ISAS - INTERNATIONAL SCHOOL FOR ADVANCED STUDIES

The PLANCK-LFI: a study of instrumental and astrophysical effects

Thesis submitted for the degree of

Doctor Philosophiæ

Astrophysics Sector

Candidate:

DAVIDE MAINO

Supervisors:

MARCO BERSANELLI
LUIGI DANESE

September 1999

SISSA - SCUOLA INTERNAZIONALE SUPERIORE DI STUDI AVANZATI

TRIESTE
Via Beirut 2-4

TRIESTE

Contents

Chapter 1

Introduction

The Cosmic Microwave Background (CMB) radiation is a strong observational evidence of the Hot Big Bang model. This model predicts that the Universe started about 10-20 billion years ago from a phase with extremely high density and temperature and that it is expanding (and cooling down) from that time to the present. After $\sim$ 300,000 years from the Big Bang, the Universe cooled down enough ($\sim$ 3000 K) to allow recombination of protons and nuclei with electrons to form atoms, so that Compton scattering cross section with photons is dramatically reduced. From this moment photons can travel almost without any further interaction with matter. Primordial nucleosynthesis calculations lead Gamow *et al.*[46] to predict the existence of a relic background radiation with a blackbody spectrum at a present temperature of few degrees.

In 1965 Arno Penzias and Robert Wilson serendipitously discovered this radiation [88] which was immediately recognized as a relic of the very early Universe by Dicke [34]. Recent data shown that it is well described by a blackbody spectrum with a temperature $T_0 = 2.728 \pm 0.004$ K [41]. From a number of experiments in the '70s and '80s, it turned out that the CMB is also isotropic to high degree of accuracy. However small departures from uniformity must be present as small clumps which eventually evolve and become structures we observe today. These small clumps leave their imprint on the CMB as small spatial variations of CMB temperature.

In 1992 the *COBE* (COsmic Background Explorer) satellite from NASA detected for the first time small temperature fluctuations in the CMB on angular scales $\theta \gtrsim 7^\circ$ at a level of $\Delta T/T \sim 10^{-5}$ [112]. Since then a new exciting era started for observational cosmology and increasing efforts have been devoted to both theoretical and experimental fronts. From the experimental side it is possible to achieve from ground- and balloon-based experiments better sensitivity and angular resolution than *COBE* (although on relatively small sky patches) and many CMB anisotropy detections have followed *COBE* result (see [67, 28] for a review). From the theoretical side an extensive work has been carried out to understand and quantify the relevant physical processes that produce CMB anisotropy and to develop adequate data processing techniques able to extract cosmological information from CMB data [132, 133]. Also it became clear that the wealth of cosmological information encoded into the CMB is largely left untouched by *COBE* being hidden on smaller angular scales.

The great impact of accurate high-resolution full-sky CMB observations on the understanding of the Universe we live in, has been recognized by both NASA and ESA

space agencies which selected two independent space missions: MAP (see MAP Web page `http://map.gsfc.nasa.gov`), a NASA Mid-Ex mission to be launched in the year 2001; and PLANCK, an ESA-M3 mission planned for a launch in the year 2007. The six years span between the two missions makes PLANCK a third generation CMB space project and more likely the *definitive* mission. PLANCK will map CMB fluctuations over an unprecedented range of frequencies (30÷857 GHz), with very high angular resolution (30′÷5.5′) and sensitivity per resolution element of the order $\Delta T/T \simeq 2 \div 4 \times 10^{-6}$ in most of the cosmological channels. PLANCK CMB anisotropy observations are expected to yield a very accurate determination of the fundamental cosmological parameters which are informative on the past, present and future of our Universe.

1.1 Outline of this Thesis

This thesis aims to address some aspects of the Low Frequency Instrument (LFI) on board the PLANCK satellite. As for any CMB experiment a great attention has to be devoted to all the possible systematic effects. Previous experiences in CMB experiments have in fact demonstrated that the more and the larger are systematic effects which contaminate the data and which have to be scrubbed in the data analysis, the less robust the final results will be. It is therefore of great importance, for not degrading the nominal angular resolution and sensitivity per resolution element, to carefully address and quantify all potential systematic effects. Through accurate and realistic simulations of PLANCK-LFI observations we study how LFI performances are affected by some of these systematic effects and how to control and further reduce these effects.

This thesis is organized as follows. We give a brief overview of the origin of microwave sky fluctuations, including CMB anisotropy, foreground contaminations originated within our Galaxy (synchrotron, free-free and dust emission) and extra-galactic foregrounds (Sunyaev-Zel'dovich effect and point sources fluctuations). Since accurate simulations are needed, they must include complete and realistic simulated microwave sky at the various observing frequencies. Unfortunately our present knowledge of foreground emissions (both galactic and extra-galactic) is far from complete and approximations have to be made. All these problems are discussed in Chapter 2.

A presentation of the PLANCK mission and its scientific capabilities is reported in Chapter 3: §3.2 reports on the selected orbit and scanning strategy; §3.3 describes the adopted telescope configuration and actual focal plane arrangement; §3.4 briefly outlines the LFI instrument and §3.5 reports LFI scientific capabilities. An introduction to the systematic effects addressed in this thesis is in §3.6 and the Flight Simulator code is presented in §3.7.

The rest of the work deals with the results from different kinds of PLANCK-LFI simulations. The off-axis position of the LFI instrument, as in the present baseline, results in optical aberrations in the angular response function of the instrument. The effect of these distortions (usually called main-beam distortions since they affect the very central part of the response function) on the nominal angular resolution is addressed in Chapter 4, firstly considering a pure CMB sky, and then a more realistic sky including galactic emission. §4.1 uses approximated response functions while "real" optical simulated ones are considered in §4.4. The effective angular resolution is derived and the loss in capabilities of cosmological parameters extraction properly quantified.

The angular response function of the LFI instrument at large angles out of the central part is extremely complex and depends not only on the telescope design but also on the whole optical system (shields, supporting structures, focal plane assembly). Signal and signal variations entering at large angles from the true direction of observation may produce errors on CMB measurements. Chapter 5 addresses this issue using a simulated full pattern of the response function and considering signal coming from our Galaxy (§5.1 and §5.2). The level of this contamination and its spatial distribution on the sky are discussed in §5.4.

As described in Chapter 2, PLANCK is a spinning space-craft with 1 minute period. Instrumental drifts occurring on time scales less than the spinning period are possible sources of systematic artifacts in final data. In general they produce "stripes" in the final maps. Chapter 6 considers typical instrumental drifts which are mainly due to gain fluctuations in the LFI amplifiers. A de-striping code for removing these artifacts is described in §6.6; its performances and possible residual striping are evaluated in §6.7.

Finally, Chapter 7 overviews simulations results and their implication on the optimization of the PLANCK design.

Chapter 2

The Hot Big Bang model, the CMB and foreground emissions

In this Chapter we briefly report on the "standard" cosmological model and on the origin of microwave sky fluctuations, including CMB anisotropy and those foreground emissions pertinent to CMB experiments like PLANCK.

Extensive work has been carried out on the origin of CMB temperature anisotropy and the reader interested in a more technical discussion can refer to a number of excellent review articles by Bond [12], Bond & Efstathiou [13, 14] and White *et al.*[128]. Here we want to give an introductory description of the relevant physical processes that leave signatures on the CMB spatial distribution.

Foreground emissions are one of the major problems in CMB experiments: these are non-cosmological signals which contribute to the observed sky temperature. It is therefore of great importance to understand their spatial and spectral behavior in order to properly subtract them from the observed signal in order to obtain clean CMB data.

In the context of this work, present knowledge of CMB anisotropies and foreground emissions is used to create synthetic sky for the detailed simulations considered in Chapters 4, 5, and 6.

This chapter is organized as follows: §2.1 describes the main features of the standard cosmological model; its observational support is in §2.2 and the inflationary scenario is presented in §2.3. The description of the CMB anisotropy statistics and of the signatures in its spatial distribution are reported in §2.4, while the present status of observations is described in §2.5. A description of Galactic and extra-galactic foregrounds is given in §2.6.

2.1 The standard cosmological model

The origin of modern cosmology may coincide with the Einstein's formulation of the General Relativity theory (hereafter GR) in 1917 which provides the mathematical background for any cosmological model. Many things happened since that time and both observational constraints and theoretical speculations have evolved into what is now extensively accepted as the "standard" cosmological model: the Hot Big Bang.

Within Einstein's GR, the simplest model is an "homogeneous" and "isotropic" universe. The first means that the properties of the Universe are the same for each observer,

while the second states that the Universe appears the same regardless the direction of observation. This is true when looking the Universe on a suitably large scale ($\gtrsim$ 300 Mpc) while on smaller scales the matter distribution is increasingly clumpy.

The space-time metric for an homogeneous and isotropic Universe is the Robertson-Walker metric:

$$ds^2 = c^2dt^2 - a^2(t)\left[\frac{dr^2}{1-kr^2} + r^2(d\theta^2 + \sin^2\theta d\phi^2)\right], \tag{2.1}$$

where t is the time variable and r, θ and ϕ are spatial polar coordinates. The constant k is a measure of the curvature of the Universe: k could be negative, zero or positive corresponding to an open, flat or a closed Universe. The function $a(t)$ is the so-called scale-factor which states how distances change with time.

The dynamical evolution of $a(t)$ is specified by Einstein's equations of GR once a stress-energy tensor is provided. It is usual to consider the content of the Universe as a perfect fluid with energy-mass density ρ, pressure p and 4-velocity $u^\mu = dx^\mu/ds$; so that the tensor reads

$$T_{\mu\nu} = -pg_{\mu\nu} + (p + \rho c^2)u_\mu u_\nu\,. \tag{2.2}$$

This is completely determined once we provide an equation of state $p = p(\rho)$. With this stress-energy tensor into Einstein's equations, one finds the Friedmann equations:

$$\frac{\ddot{a}}{a} = -\frac{4\pi G}{3}\left(\rho + \frac{3p}{c^2}\right) + \frac{\Lambda c^2}{3}, \tag{2.3}$$

$$\left(\frac{\dot{a}}{a}\right)^2 + \frac{kc^2}{a^2} = \frac{8\pi G}{3}\rho + \frac{\Lambda c^2}{3}, \tag{2.4}$$

where G is the Newton gravitational constant and Λ is the cosmological constant. It is worth noting that for $\Lambda \neq 0$ GR does not reduce to newtonian theory in the weak field limit. From these two equations one can derive time evolution for the energy density ρ which is:

$$d(\rho c^2 a^3) = -3a^2 p\,. \tag{2.5}$$

This equation together with the equation of state $p = p(\rho)$, yields the expressions $\rho = \rho(a)$ for the different kinds of cosmological components: for ultra-relativistic components, for which $p = \rho c^2/3$, we have $\rho \propto a^{-4}$; for pressure-less matter $p = 0$ and $\rho \propto a^{-3}$, while for cosmological constant, or vacuum energy, $p = -\rho c^2$ and therefore ρ is constant. More generally, for an equation of state of the form $p = w\rho$ with $w =$ constant, the energy density evolves as $\rho \propto a^{-3(1+w)}$.

Eq.(2.4) shows that there is a direct link between the energy density and the geometry of the Universe. In particular there is a critical density for which $k = 0$ (if $\bar{\Lambda} = 0$):

$$\rho_c = \frac{3H^2}{8\pi G}, \tag{2.6}$$

where $H(t) = \dot{a}/a$ is the Hubble parameter. Therefore the energy content in the Universe states the final destiny of the expansion of the Universe: for $\rho > \rho_c$ a closed Universe results; values of ρ lower than ρ_c characterize an open Universe, while for energy density equal to the critical density we have a spatially flat Universe.

Since the flat Universe ($k = 0$) has a particular, well defined value of the critical density, it is usual to express the mass-energy density content through the density parameters defined as the ratio of the density to the critical density: $\Omega(t) = \rho/\rho_c$. The case for $k = 0$ (and hence $\Omega = 1$) is of particular interest because it is a good approximation at very early times and also because we have some reasons to suspect that we are living in a flat Universe. In this case Eq.(2.4) has particularly simple solutions: $a(t) \propto t^{2/3}$ for a Universe dominated by pressure-less matter and $a(t) \propto t^{1/2}$ for a Universe filled with relativistic matter. If the Universe is dominated by the vacuum energy, or if the cosmological constant is large, the scale-factor grows exponentially: $a(t) \propto \exp(Ht)$ where $H = \sqrt{\Omega_\Lambda c^2/3}$ and Ω_Λ the vacuum energy density parameter. This solution, called the "de-Sitter" expansion, is of particular interest in the context of the *inflationary* paradigm.

Although the natural solutions of Einstein's equations yield a dynamical Universe (*i.e.* which is expanding or contracting) Einstein rejected this idea in the beginning and, introducing the so-called "cosmological constant", proposed a static solution for the Universe. But once the expansion of the Universe had been established by observations, he came back to the natural solution and he called the cosmological constant "the worst mistake in my life".

2.2 Observational support

There are mainly three observational pillars supporting the Hot Big Bang model: the Hubble law of expansion, the primordial abundances of light elements and the spectral and spatial distribution of the CMB.

- In 1929 Edwin Hubble [56] made an outstanding discovery: galaxies seem to be receding from the observer with a velocity v proportional to their distance d:

$$v = H_0 d\,. \tag{2.7}$$

  This is the Hubble law and the constant H_0 (the Hubble constant) is the present value of the Hubble parameter. This is expressed as $H_0 = 100\,h$ km/s/Mpc and possible values range between 40 and 100 km/s/Mpc. The modern cosmology reads this fact as follows: galaxies are taken more or less "fixed" in a space that is expanding.

- After $\sim$ 1 minute from the Big Bang the temperature is low enough ($\sim 10^9$ K) to allow fusion of neutrons and protons in the primordial plasma. During this phase a precise amount of light elements were produced. The predicted relative abundances of light elements and isotopes like D, ^{3}He, ^{4}He and ^{7}Li are confirmed by observations, as shown in Fig. 2-1, if the baryon density is between $1.5{\times}10^{-31}$ g.cm^{-3} and $4.5{\times}10^{-31}$ g cm^{-3} ($\Omega_B h^2 = 0.008 - 0.024$, where Ω_B is the baryons density parameter). For further details on primordial nucleosynthesis see [110, 123] and references therein.

- The CMB is the most precise blackbody: deviations from the Planckian shape are less than 0.03% of the peak intensity (see Fig. 2-2); measurements by FIRAS (Far Infra-Red Absolute Spectrophotometer) on-board *COBE* yield $T_0 = 2.728 \pm 0.004$ K with 95% Confidence Level between 0.5 cm $\leq \lambda \leq 500\mu$m [41]. The only plausible origin

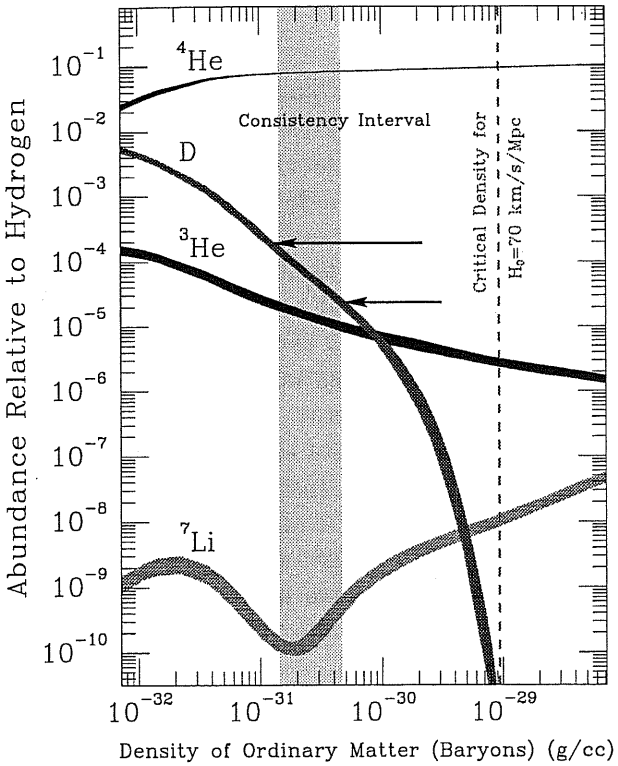

Figure 2-1: Light-elements production during the Big Bang. The width of the lines shows the $2-\sigma$ theoretical uncertainty. Primordial abundances prediction agreed with observation if $\Omega_B = 0.008 - 0.024$. From astro-ph/9703174.

is the hot plasma filling the Universe at very early times. Temperature fluctuations of the order of 30 μK are observed by *COBE*-DMR [112] on scales larger than few degrees. These are produced by density fluctuations of the same order $\delta\rho/\rho \sim 10^{-5}$ on scales $\sim 30h^{-1} - 10^4 h^{-1}$ Mpc. These small fluctuations are able to explain present structures in the Universe once they evolve under the action of gravity.

We discuss in further detail the CMB origin and main properties. In the early hot Universe matter and radiation are tightly coupled and in thermal equilibrium since photon-creating processes ($\gamma + e \to \gamma + \gamma + e$, $e + p \to e + p + \gamma$, $e^+e^- \to \gamma + \gamma$) proceed rapidly with respect to the Hubble expansion. A system in thermal equilibrium is completely specified by its temperature and any conserved quantum numbers: in absence of non-equilibrium processes, the radiation is an isotropic blackbody. The efficiency of these processes decreases with decreasing density for the expansion of the Universe and, at a certain time, matter and radiation de-couple: protons and nuclei recombine with electrons to form atoms which marginally interact with photons. This epoch is called re-combination and the region where the last scattering happened is called Last Scattering Surface (LSS). Since the photons number is conserved in an adiabatic expansion the spectral shape of the CMB is preserved: the only effect is the decrease of the thermodynamic temperature of the CMB as the Universe expands.

The CMB is a probe also of the isotropy and homogeneity of the Universe. Measurements in the seventies [23, 111] have shown an anisotropy in the CMB, at a level of $\Delta T/T \sim 10^{-3}$, with a clear dipole pattern. Recent results from *COBE* [60] report a dipole amplitude of $\Delta T = 3.343 \pm 0.016$ mK and a dipole direction oriented towards galactic co-

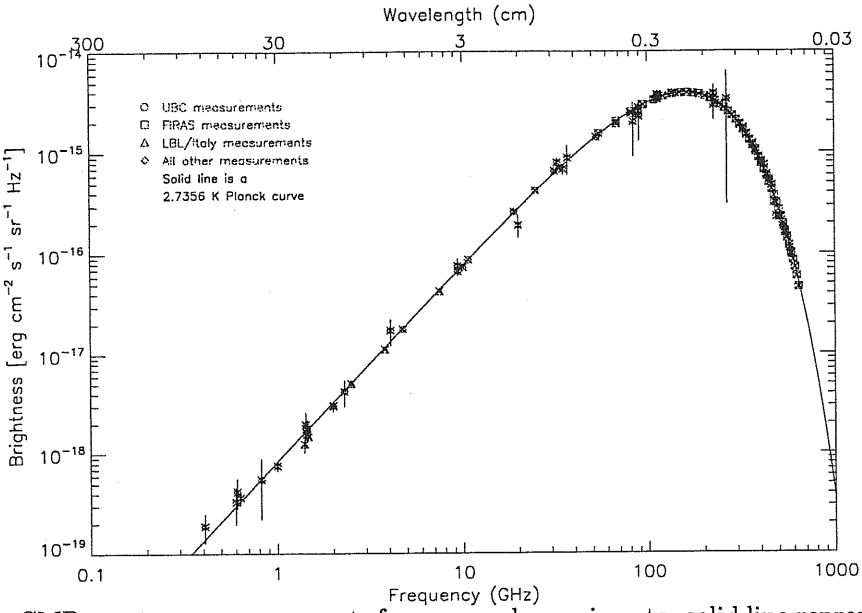

Figure 2-2: CMB spectrum measurements from several experiments: solid line represents a black-body spectral shape. From astro-ph/9902027.

ordinates ($264°.4 \pm 0.3, 48°.4 \pm 0.5$). The dipole nature of this anisotropy is interpreted as a simple Doppler effect due to the motion of our Local Group of galaxies with respect to the CMB reference frame: after correcting for Earth's motion around the Sun, a Local Group velocity of 627 ± 22 Km/sec resulted towards galactic coordinates ($276° \pm 3°, 30° \pm 3°$). If we exclude this anisotropy, which is local in origin, the CMB has the same temperature in each sky direction at a level of about one part in 10^{-5}. This fact is another evidence of the cosmic origin of the CMB: any local source would be expected to show some level of anisotropy, since the distribution of matter nearby is clearly not uniform.

It is fundamental to note that the angular dimension of regions in causal contact on the LSS is about $\theta \simeq 2°\Omega^{1/2}$. Anisotropy on scales larger than $2°$ are therefore primordial since they are not affected by causal interactions; on smaller angular scales CMB anisotropy reflects physical processes involved in structure formation.

2.3 The inflationary scenario

The Hot Big Band model is succesful but there are many open issues which have to be addressed. The most relevant are: the flatness problem (why the density in the Universe is so close to the critical value ρ_c?); the horizon problem (why the CMB has the same temperature at high degree of accuracy on the whole sky if causal regions at LSS have dimensions of few degrees?) and the origin of primordial density fluctuations (why the Universe is indeed so clumpy on small scales while it is homogeneous and isotropic on very large scales?).

In particular great attention was, and is, devoted to the problem of the origin of inhomogeneities in the Universe. Most of the early work deal with a Universe filled with baryonic matter [87, 106, 107]. These models predict a level of fluctuations of $\sim 10^{-3}$.

The fact that no anisotropy at this level was detected in a number of experiments in the '70s and '80s (see [85] for a review), forced to consider models dominated by non-baryonic dark matter.

Many assumptions have to be made about the initial conditions for gravitational instability: the geometry of the Universe (*e.g.* flat), statistical distribution of initial density fluctuations (*e.g.* Gaussian) and their power spectrum. These assumptions are now included in the so-called inflationary paradigm for which the Universe, in the very early phases of its life ($t \sim 10^{-34}$ sec), underwent an exponential expansion (see [69] for a review). Inflation solves the flatness problem: increasing the value of $a(t)$ by a large factor implies that, at inflation epoch, (k/a^2) in Eq.(2.4) is negligible. This in practice means that we can ignore the dynamical impact of the k/a^2 term which is equivalent to have $k \simeq 0$ and, as a consequence, Ω close to unity with high degree of accuracy. Inflation provides also a natural explanation for the horizon problem: it is possible to demonstrate from Eq.(2.4) that the quantity cH^{-1} can be regarded as a physical horizon for processes in the expanding Universe. Regions separated by less than this scale can exchange information (photons) otherwise they must be considered as isolated. In the De-Sitter solution the quantity cH^{-1} remains constant while the length scales increase exponentially. If inflation lasted for a sufficiently long time, *all* our Universe came from a region initially smaller than the effective horizon. This could explain why the CMB has the same temperature all over the whole sky. Inflationary models go further ahead specifying the initial conditions for structure formation and making specific predictions on the statistics of the CMB anisotropy as well as on the matter distribution.

A plausible scenario for driving such an expansion is needed as well as a physical mechanism able to generate primordial density fluctuations. This is provided by cosmological scalar field. It is usual, in particle physics, to represent zero-spin particles with a scalar field (*i.e.* which is unchanged under coordinates transformations). Let us indicate this homogeneous scalar field as ϕ and define its energy density and pressure as:

$$\rho_\phi = \frac{1}{2}\dot{\phi}^2 + V(\phi)\,, \tag{2.8}$$

$$p_\phi = \frac{1}{2}\dot{\phi}^2 - V(\phi)\,, \tag{2.9}$$

where the first terms can be regarded as kinetic energy while the seconds as potential-binding energy. Substituting these expressions into the Friedmann equations, one finds:

$$H^2 = \frac{8\pi G}{3}\left[\frac{1}{2}\dot{\phi}^2 + V(\phi)\right], \tag{2.10}$$

$$\ddot{\phi} + 3H\dot{\phi} = -V'(\phi)\,, \tag{2.11}$$

where prime indicates $d/d\phi$. It is standard to take the scalar field initially displaced from the minimum of the potential $V(\phi)$ and then slowly approaching to the minimum value of V. In this so-called slow-roll approximation ($\dot{\phi}^2 \ll V$, $|\ddot{\phi}| \ll H\dot{\phi}$), skipping terms of higher orders ($\ddot{\phi}$ and $\dot{\phi}^2$), one gets:

$$a(t) \sim \exp(Ht)\,, \qquad H(t) = \left(\frac{8\pi G}{3}V\right)^{1/2} \sim \text{const}\,. \tag{2.12}$$

Therefore when ϕ is slow-roll approaching the minimum of V a quasi-exponential expansion results. Once inflation is over the ϕ field starts to oscillate around the minimum position and the decay of these oscillations may lead to particle production and radiation. This is called re-heating. Quantum fluctuations present during inflation are then "stretched" by the accelerated expansion to become eventually density perturbations. Within these models fluctuations are Gaussian in origin with a power law power spectrum $P(k) \propto k^n$ that is close to a scale-invariant spectrum with $n = 1$. Inflation has therefore a natural physical mechanism for the origin of primordial density fluctuations. These fluctuations leave their imprint as spatial variations in the CMB temperature which is therefore a unique probe of the inflationary scenario.

2.4 The CMB angular power spectrum

It is usual to expand CMB temperature fluctuations on the sky in spherical harmonics:

$$\frac{\Delta T}{T}(\theta, \phi) = \sum_{\ell,m} a_{\ell m} Y_{\ell m}(\theta, \phi)\,, \tag{2.13}$$

where the $Y_{\ell m}(\theta, \phi)$ are the spherical harmonic functions and θ and ϕ are polar coordinates. The $a_{\ell m}$ are the coefficients of this expansions. Within the context of inflation CMB fluctuations are a Gaussian random field and therefore are completely specified by the 2-nd order momentum: the two-point correlations function $C(\gamma)$. This reads as follows:

$$C(\gamma) = \left\langle \frac{\Delta T}{T}(\mathbf{n_1}) \frac{\Delta T}{T}(\mathbf{n_2}) \right\rangle\,, \tag{2.14}$$

where γ is the angle between the two unit vectors $\mathbf{n_1}$ and $\mathbf{n_2}$ and the average is taken over an ensemble of all possible skies. If we substitute Eq.(2.13) into Eq.(2.14) we obtain:

$$C(\gamma) = \sum_{\ell m} \sum_{\ell' m'} \langle a_{\ell m} a^*_{\ell' m'} \rangle Y_{\ell m}(\theta, \phi) Y^*_{\ell' m'}(\theta', \phi')\,, \tag{2.15}$$

and considering that CMB is statistically rotationally invariant we have:

$$C(\gamma) = \frac{1}{4\pi} \sum_{\ell} (2\ell + 1) C_\ell P_\ell(\cos\gamma)\,. \tag{2.16}$$

We use the fact that the multiplication of spherical harmonic functions gives the Legendre polynomials $P_\ell(\cos\gamma)$ and we have defined $C_\ell = \langle a_{\ell m} a^*_{\ell' m'} \rangle$. Therefore the angular power spectrum C_ℓ gives a complete statistical description of the CMB fluctuations. For example, if we take the primordial fluctuations power spectrum of the form $P(k) = Ak^n$ then for large angular scales ($\ell \lesssim 20$) the CMB angular power spectrum becomes:

$$C_\ell = Q^2 \frac{4\pi}{5} \frac{\Gamma(\ell + \frac{n-1}{2})}{\Gamma(\ell + \frac{5-n}{2})} \frac{\Gamma(\frac{9-n}{2})}{\Gamma(\frac{3+n}{2})}\,, \tag{2.17}$$

where n is the spectral index of the power spectrum, Q^2 is the quadrupole amplitude normalization and $\Gamma(x)$ is the Gamma function. If $n = 1$ as inflation predicts, Eq.(2.17) writes:

$$C_\ell = \frac{24\pi}{5} \frac{Q^2}{\ell(\ell + 1)} \tag{2.18}$$

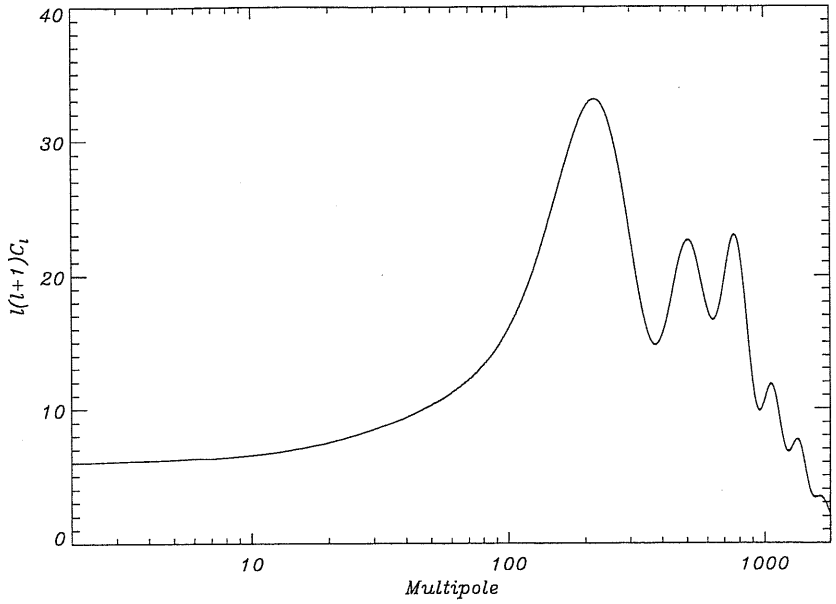

Figure 2-3: Angular Power Spectrum of CMB temperature fluctuations according to a standard CDM model within the inflationary scenario. Model parameters are: $H_0 = 50$ Km/s/Mpc, $n = 1$, $\Omega = 1$, $\Omega_B = 0.06$

and thus the quantity $\ell(\ell+1)C_\ell = \text{constant}$. It is usual therefore to plot this quantity as a function of ℓ, instead of C_ℓ alone, since it directly shows informations on the primordial spectral index n.

Fig. 2-3 shows an example of the angular power spectrum of the CMB: a standard Cold Dark Matter (CDM) model, with a spectral index of the primordial density fluctuations $n = 1$, with a flat geometry ($\Omega = 1$) and with a baryon content of $\Omega_B = 0.06$. The remaining matter content is non-baryonic dark matter. It is surprising to note so many features in the angular power spectrum of the CMB since the primordial density fluctuations is assumed to have a scale-invariant featureless power-law power spectrum. The flat part at small ℓ (*i.e.* at large angular scales: $\theta = 180°/\ell$) is primarely due to the Sachs-Wolfe effect [101]. This is simply the gravitational redshift (or blueshift) experienced by CMB photons between the LSS and us. If the gravitational potential does not change with time, the amount of energy shift is just the difference in the gravitational potential between emission and observation. If the gravitational potential changes with time we have also to consider this time evolution and to integrate the derivative of the potential along the photon path. This last effect is called Rees-Sciama effect [97] or integrated Sachs-Wolfe effect and it is an order of magnitude below the Sachs-Wolfe effect.

The most relevant features in the CMB angular power spectrum are the peaks at values of $\ell \gtrsim 100$ which are usually called "Doppler Peaks". To understand their origin we have to remind that at early time baryons and photons are coupled together and behave like a single fluid. A gravitational potential produces forced acoustic oscillations in the fluid just like the case of a driven harmonic oscillator with the driven force due to gravity, inertia of baryons and photons pressure. Re-combination is a nearly instantaneous process and

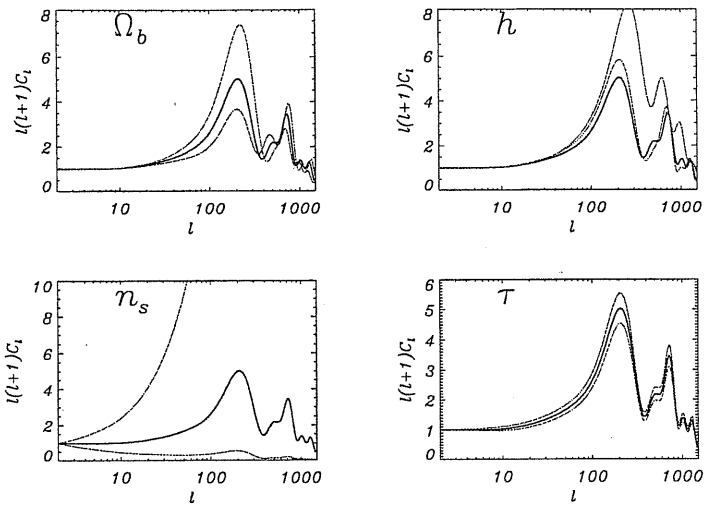

Figure 2-4: Signature of different cosmological parameters. In each box only the labelled parameter is varied while the others are kept fixed. The black solid lines refer to a model with $\Omega_B = 0.06$, $h = 0.65$, $n = 1.0$ and $\tau = 0.05$. The red lines are for lower values of the parameters (0.03, 0.3, 0.5 and 0.0 respectively), while the blue lines are for higher values (0.1, 0.8, 1.5 and 0.1).

modes of acoustic oscillations with different wavelength are "frozen" at different phases of oscillation: the first peak corresponds to a wave that has a density maximum just at the time of the last scattering. The subsequent peaks are produced by high-frequency modes that have therefore oscillated more than once. The throats correspond to velocity maxima that are 90° out of phase with respect to density maxima.

The last relevant feature to note in the CMB angular power spectrum is the nearly exponential decay of the power spectrum for multipoles $\ell \sim 1000$ (corresponding to $\theta \sim 10'$). As already mentioned, re-combination is "nearly" instantaneous and in this short time photons can diffuse (*i.e.* they have a non-negligible mean free path). Oscillations on scales smaller than this free path are then erased by diffusion processes and give rise to the quasi-exponential cut-off at high ℓ. This is usually called "collisional damping" or "Silk damping" [107, 55]. Similarly, a possible re-ionization of the Universe at late times with a significant optical depth τ may erase CMB anisotropy and leave proper signature on the power spectrum.

These are the most relevant CMB angular power spectrum features that occur in a wide range of models. Different models, specified by different sets of cosmological parameters, have their own CMB power spectrum. In Fig. 2-4 CMB power spectra are reported for different sets of cosmological parameters to emphasize the signature of each single parameter. The effect of τ is to erase power at large ℓ; the Hubble constant shifts and boosts the peaks, while n increase power at large ℓ with respect low ℓ values. Finally increasing Ω_B increase odd peaks and suppress even peaks.

Beside the usual density (scalar) fluctuations considered here, inflationary models also predict the existence of tensor modes (gravitational waves) which generate CMB anisotropy only at small ℓ values. In the recent years detailed studies on CMB polarization have been carried out by several authors [105, 59, 55] underlying that CMB polarisation

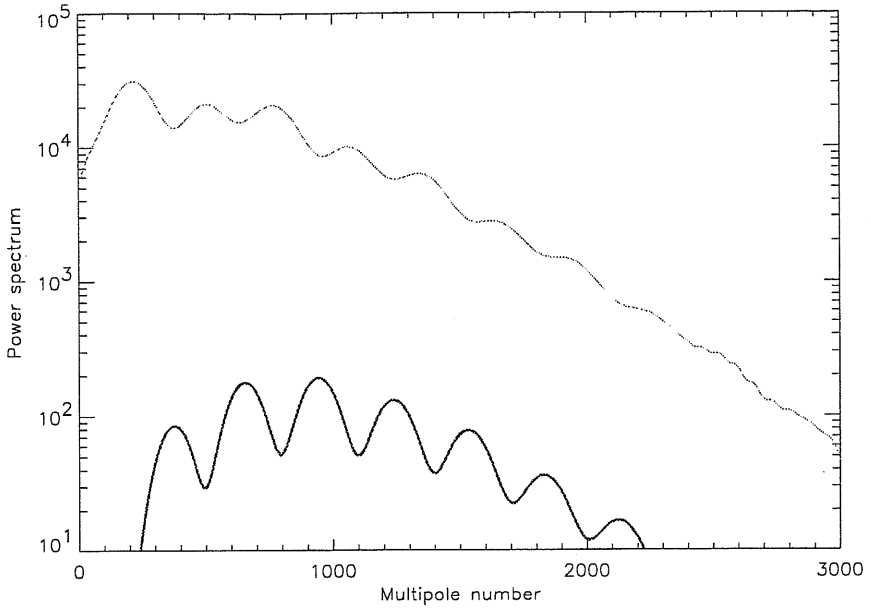

Figure 2-5: CMB Polarization power spectrum compared with the temperature power spectrum for a standard CDM model. Only scalar modes are presented. (From [74]).

provides informations that complement those from CMB temperature anisotropies. CMB polarization is generated from Thomson scattering of temperature anisotropy on the LSS with no evolution between that time and the present as, on the contrary, occurs for CMB temperature anisotropy: CMB polarization is therefore a unique view of the LSS.

Fig. 2-5 shows a typical polarisation angular power spectrum compared with the temperature pattern: the level is expected to be 5-10% of the temperature anisotropy: few μK of signal which is indeed very small and a real hard task to achieve. However the reward should be great, in particular the use of both temperature and polarization CMB data can break the degeneracy for some of the cosmological parameters (*i.e.* different combinations of cosmological parameters give the same CMB temperature power spectrum).

Therefore from a high precision measurements of the CMB angular power spectrum it is possible to extract a huge amount of cosmological information that may support current ideas in the field (like the inflationary paradigm) or may show that the Universe is far from what we think it is.

2.5 CMB anisotropy measurements and related issues

In 1992 the DMR (Differential Microwave Radiometer) experiment, operating at 31.5, 53 and 90 GHz, on-board *COBE* satellite detected for the first time CMB anisotropy on large angular scales $\theta \gtrsim 7^\circ$ with sensitivity $\Delta T/T \sim 10^{-5}$ corresponding to an *rms* quadrupole amplitude $Q_{rms} = 16 \pm 12\mu$K [112, 6, 49].

Several detections of CMB anisotropy have followed the DMR announcement of the first discovery (see for example [47, 52, 118, 77, 83, 33]). The current status of CMB

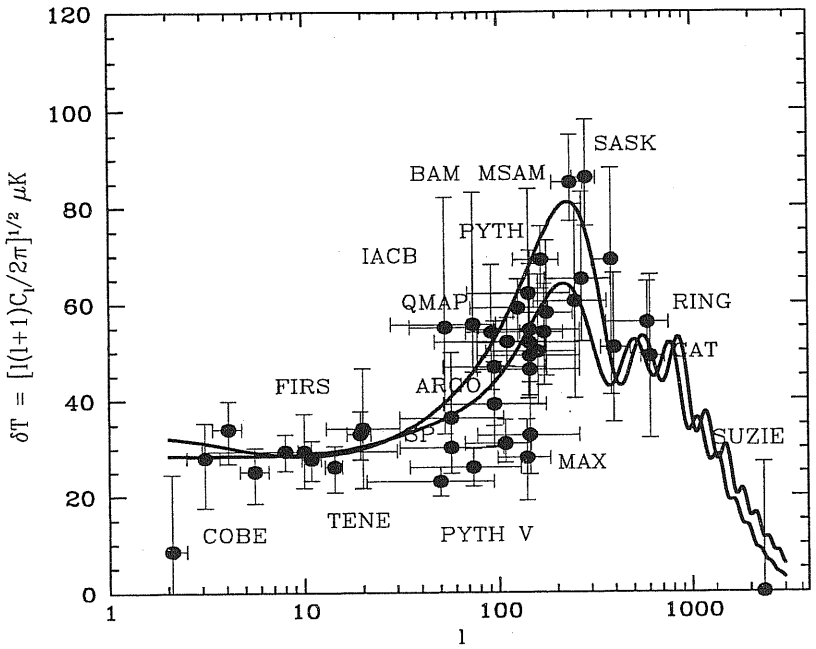

Figure 2-6: Summary of the CMB anisotropy detection in terms of power spectrum. The blue line is a Λ Cold Dark Matter Model with $\Omega_\Lambda = 0.65$, the cyan line is an Standard Cold Dark Matter Model.

anisotropy measurements is reported in Fig. 2-6: several experiments using different technologies (microwave receivers and incoherent bolometers), observing strategies and frequencies, probed the CMB angular power spectrum over a wide range of scales. However, despite the large number of detections, the situation is still open: data are consistent with different CMB models without a preferred one. The error bars in Fig. 2-6 are still too large.

There are many fundamental limitations in CMB experiments: cosmic variance, detectors sensitivity and foreground contaminations. The last is extensively discussed in the next section. Systematic effects are also a real issue for CMB experiments and they are different for different kinds of experimental setups. It is difficult to estimate them and this thesis addresses certain systematic effects related to PLANCK-LFI.

Cosmic variance is a CMB intrinsic limitation. In most of the cosmological models, the observed CMB temperature is in fact a single realization of a stochastic process. Therefore our observable Universe may not exactly follow the average over the ensemble of possible realizations. This is equivalent to say that the $a_{\ell m}$ coefficients of the spherical harmonics expansion of the CMB temperature anisotropy are independent, identically-distributed Gaussian random variable (for a given ℓ) thus C_ℓ has a χ^2 distribution with $2\ell+1$ degrees of freedom. The variance on C_ℓ is therefore:

$$\frac{\Delta C_\ell}{C_\ell} = \sqrt{\frac{2}{2\ell+1}}, \tag{2.19}$$

which is quite substantial for small values of ℓ since a small number of modes ($m = 2\ell+1$) is available.

Incomplete sky coverage introduces another uncertainty: the observed region may not be representative of the realization as a whole. This is called sample variance. In general for CMB experiments which do not cover the whole sky, sample variance is larger than cosmic variance by a factor proportional to the ratio of the whole sky area and the surveyed solid angle.

Detectors sensitivity is an issue in CMB anisotropy experiment since the very small signal that has to be measured on a portion of the sky as large as possible. In the present generation of CMB anisotropy experiments, the need of high sensitivity drives the use of arrays of detectors.

Combining cosmic and sample variances with instrumental noise, the final variance on C_ℓ reads:

$$\frac{\Delta C_\ell}{C_\ell} = \sqrt{\frac{2}{2\ell+1}}\sqrt{\frac{4\pi}{\Omega_{obs}}}\left[1+\frac{4\pi\sigma_{pix}^2}{B_\ell^2 C_\ell N_{pix}}\right], \tag{2.20}$$

where N_{pix} is the total number of pixels observed with uniform sensitivity σ_{pix}, Ω_{obs} is the solid angle observed and B_ℓ^2 is the beam window function ($B_\ell^2 = \exp[-\ell^2\sigma_B^2]$ for a gaussian beam with angular resolution equal to $\sigma_B\sqrt{8\ln 2}$).

2.6 Foreground Emission

This section aims at summarizing the main physical properties of those foreground contaminations pertinent to satellite CMB anisotropy experiments like MAP and PLANCK.

2.6.1 Galactic Foregrounds

There are mainly three physical processes responsible of galactic foreground emission: synchrotron, free-free (or thermal Bremsstrahlung) and dust emission. In Fig. 2-7 the intensity, in antenna temperature, of the galactic foregrounds as a function of frequency is shown together with CMB levels for monopole ($T_0 = 2.728$ K), kinematic dipole ($\Delta T \simeq 3$ mK) and cosmic Quadrupole amplitude ($\approx 28\mu$K). A clean cosmological window is around 100 GHz. Fig. 2-7 shows clearly the different spectral behavior of the three galactic foreground emissions with respect to the CMB. This fact can be used to clean CMB data by means of multifrequency observations covering as large a frequency range as possible. It is clear that at very low frequencies ($\nu \lesssim 1$ GHz) synchrotron emission dominates the microwave sky, while dust dominates at very high frequency ($\nu \gtrsim 100$ GHz). Useful information on these two emission processes can be obtained exploiting observations in the frequency region where they dominate. On the contrary, free-free emission, never dominates over either synchrotron or dust thus complicating free-free emission studies.

Synchrotron Emission Galactic synchrotron emission originates from cosmic-ray electrons accelerated into the galactic magnetic field. Every charged particle accelerated radiates. In this case the magnetic field **B** produces the boost. This emission is called *cyclotron* radiation for non-relativistic particles while *synchrotron* radiation for extreme relativistic particles. Thus the overall synchrotron emission spectrum depends upon the energy distribution of the particles considered and on the magnetic field [100, 70]. The

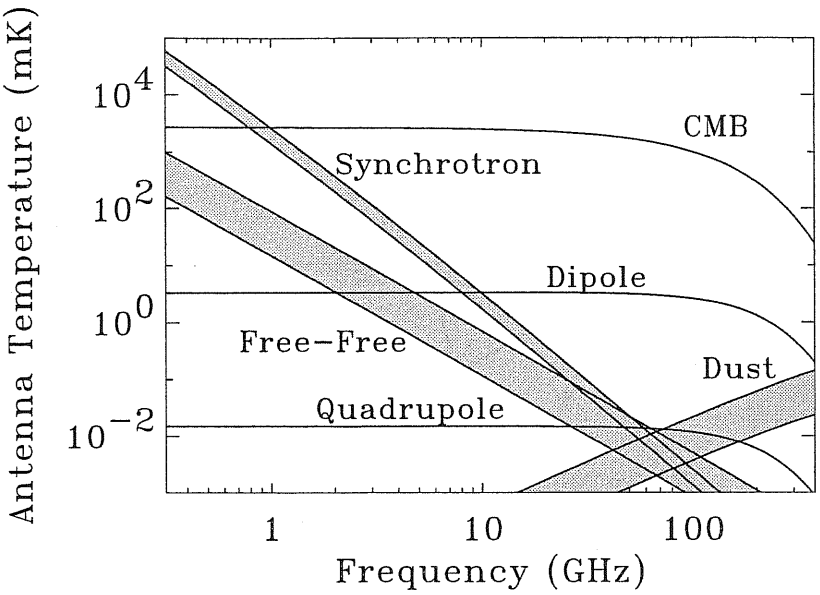

Figure 2-7: Relative intensity of foreground emissions as a function of frequency together with CMB anisotropy level

particle trajectory is helicoidal since particles move along the magnetic field line force while rotating around the field direction. It is possible to introduce a rotation frequency

$$\omega_B = \frac{qB}{\gamma mc}, \tag{2.21}$$

where γ is the usual relativistic correction and q and B are the particle charge and magnetic field intensity. The relativistic electrons velocity beams the radiation into a cone with amplitude $\Delta\theta \sim 1/\gamma$ as in Fig. 2-8 [100]. The effect of beaming is to concentrate synchrotron radiation in a narrow region around the particle direction of motion. From Fig 2-8 an observer receives radiation from points 1 and 2 if their separation is such that the two cones include observer's line of sight. The time interval at emission from points 1 and 2 is given by:

$$\Delta t = \frac{2}{\gamma\omega_B \sin\alpha}, \tag{2.22}$$

where the $\sin\alpha$ term reprojects the electron trajectory into a plane normal to the **B** field. The observed delay $\Delta t'$ differs from Eq.(2.22) by a factor $(1 - v)$ and, since $\gamma \gg 1$, this becomes $\sim 1/(2\gamma^2)$ and the observed delay is γ^3 times smaller than the characteristic period ($\propto \omega_B^{-1}$). The resulting spectrum is fairly broad with a cut-off for frequencies of the order $1/\Delta t'$ [100]. It is possible to define a critical frequency after which the spectrum cuts-off:

$$\omega_c \equiv \frac{3}{2}\gamma^2 \omega_B \sin\alpha\,. \tag{2.23}$$

In the case of a high relativistic particle, the power emitted per unit frequency is

$$P(\omega) = \frac{\sqrt{3}}{2\pi}\frac{q^3 B \sin\alpha}{mc^2} F\left(\frac{\omega}{\omega_c}\right), \tag{2.24}$$

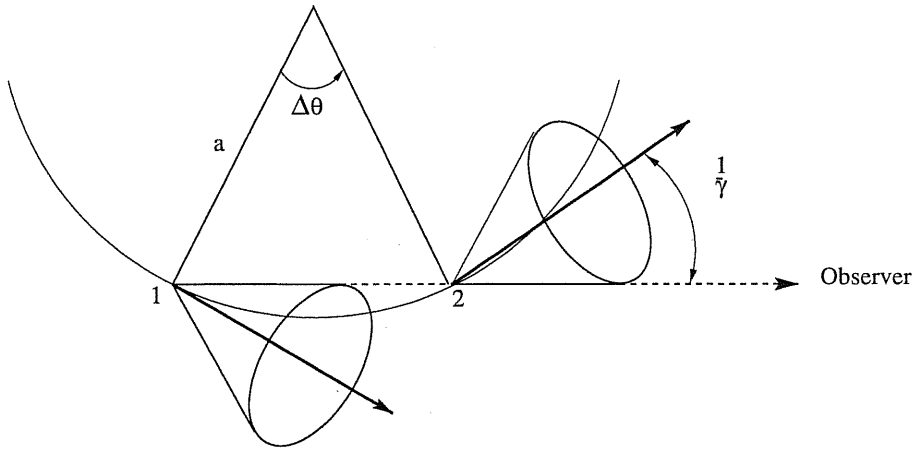

Figure 2-8: The beaming effect for a relativistic particle

where the function $F(x) \equiv \int_x^\infty K_{5/3}(\eta)d\eta$ and $K_{5/3}$ is the modified Bessel function of 5/3 order.

This is for a single electron: the astrophysical case is much more complicated since we have to consider many particles (cosmic rays) with an energy distribution $N(E)$ and with angles α different for each particle. For a more realistic model of synchrotron emission in our Galaxy, the galactic magnetic field has to be known for each line of sight. Following Bennet *et al.*[5], we write the observed brightness temperature, related to the flux $S(\nu)$ by $S(\nu) = 2kT(\nu)\nu^2/c^2$ (where k is the Boltzmann constant),

$$T(\nu) = \int\int P(\nu, \mathbf{B}, E)\, N(E, \mathbf{l})\, dEdl\,, \tag{2.25}$$

where $P(\nu, \mathbf{B}, E)$ is the power emitted at a frequency ν by a single electron with energy E in a magnetic field $\mathbf{B}$ (e.g. Eq.(2.24)), and $N(E, \mathbf{l})dE$ is the number of relativistic electrons of energy E per unit volume in the position $\mathbf{l}$ along the line of sight. Unfortunately both $N(E, \mathbf{l})$ and $\mathbf{B}(\mathbf{l})$ are poorly known and some approximations have to be made in order to compute the integrals in Eq.(2.25).

If we assume the electrons directions randomly oriented with respect to the magnetic field (so the angles α are isotropically distributed) and the energy spectrum as a power law $dN/dE = N_0 E^{-p}$, the integration of Eq.(2.25) yields

$$T(\nu) = \frac{\sqrt{3}q^3}{8\pi mc^2}\left(\frac{3q}{4\pi m^2c^5}\right)^{(p-1)/2} |\mathbf{l}|\, N_0\, B_{\rm eff}^{(p+1)/2}\, \nu^{-(p+3)/2}\, a(p)\,, \tag{2.26}$$

where $a(p)$ is a weak function of the electron energy, $|\mathbf{l}|$ and $B_{\rm eff}$ are, respectively, the length through the considered volume and the effective magnetic field along the line of sight. So we have $T(\nu) \propto \nu^{-(p+3)/2} \equiv \nu^{-\beta_{\rm sync}}$ where $\beta_{\rm sync}$ is the synchrotron spectral index. The local cosmic-ray electrons energy spectrum is measured to be well described by a power law, for energies which describe the radio peak of synchrotron emission ($E \simeq$ few GeVs). In this range the power law spectral index is observed ([126, 82]) to increase from 2.7 to 3.3. This is not surprising since energy loss mechanisms for electrons increase with the square of the electron energy. A similar behavior is therefore expected also for

Freq. [MHz]	Resolution [°]	Gain uncertainty [%]	Zero-level [K]	Zero-level correction[a] [K]	Sky coverage [%]
38	7.5	5	300	-	72
178	0.22×5	10	15	+27.5	57
404	8.5×6.5	3.6	2.3	N/A	68[b]
408	0.85	10	3	-	100
820	1.2	6	0.6	-0.97	57
1420	0.6	5	0.5	-0.13	68

[a] from Lawson *et al.*[65]

[b] the sky is undersampled at survey resolution.

Table 2.1: Summary of radio maps available. The 2326 MHz is not included since only the preliminary version is available and lot of work has to be done

the spectral index $\beta_{\rm sync}$. This is used by Bennet *et al.*[5] to model the synchrotron radio emission at GHz frequencies.

Synchrotron dominates the microwave sky emission at very low frequencies ($\lesssim 1$ GHz) where a determination of the spectral index is also possible. The only synchrotron full-sky map available is the survey at 408 MHz from Haslam *et al.*[53] (see Fig. 2-9) albeit large areas are surveyed at 1420 MHz (all the northern hemisphere for declinations $\delta > -19°$) [98] and at 2326 MHz (the southern hemisphere with $\delta < 30°$) [58]. Other incomplete sky coverage are obtained at 38 MHz [79], at 178 MHz [119], at 404 [86] and 820 MHz [7]. Table 2.1 summarizes the existing maps which cover a significant sky fraction. These surveys are strongly affected by zero-level and gain uncertainties which become particularly relevant at higher frequencies since the overall signal decreases. Fitting these data to the power law dependence in $T(\nu)$, large corrections have to be made to reconcile these data with theoretical prediction as in Eq.(2.26). These corrections are always of the order of map errors in Table 2.1. For example typical gain uncertainty are $\simeq$ 10% and 5% for the 408 and 1420 MHz surveys, while zero-levels are $\simeq$ 3 K and 0.5 K respectively for the two maps. In regions where the signal is low, where one is expected to do the best CMB measurement, these uncertainties translate into a 36 % error on the derived synchrotron spectral index which, of course, produces complete different predictions of synchrotron emission at CMB frequencies. Furthermore a meaningful extrapolation to CMB frequencies has to consider the proper spectral shape of cosmic-ray electrons which translates into a synchrotron emission with a knee around 10 GHz. Platania *et al.*[89], from data in the 1-10 GHz range, have found a possible indication of such a spectral steppening. However data are large effected by systematic effects and only new precise measurements of microwave sky emission can shade light on this important point.

However it has been found that $\beta_{\rm sync}$ steepen with increasing frequency [65, 3, 4] as expected and that is spatially variable $2.3 < \beta_{\rm sync}(408, 1420) < 3.0$ due to place-to-place variations of both electrons energy spectrum and galactic magnetic field [99, 65].

A meaningful determination of the synchrotron spectral index strongly depends upon the efficiency of the "cleaning" technique adopted to remove systematic effects. A first attempt has been made by Davies *et al.*[27] with the two largest surveys (408 and 1420 MHz):

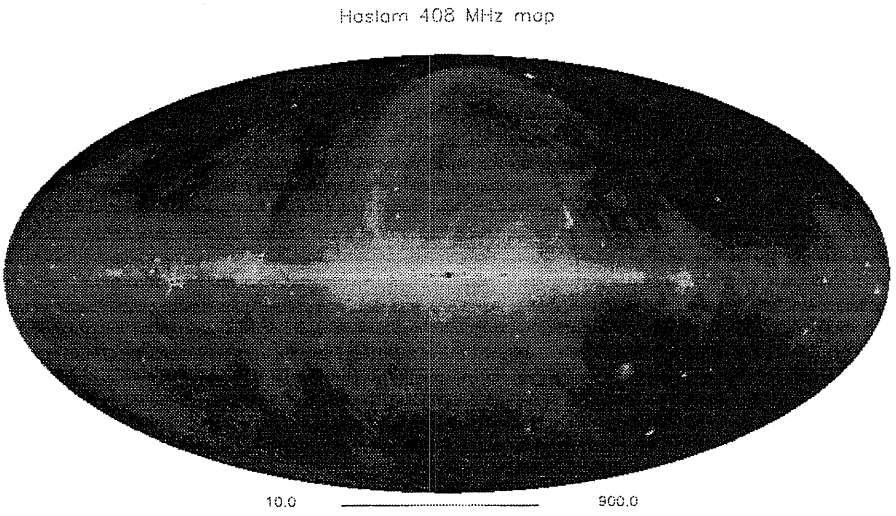

Figure 2-9: Haslam map at 408 MHz. Units of K.

they found at high galactic latitudes, which are relevant for a CMB experiment, indices $\beta_{\rm sync}$ between 2.8 and 3.2.

Other evidences of a mean spectral index $\beta_{\rm sync} \simeq 3$ at high frequency have been found also by Platania *et al.*[89] in the frequency range $1 \div 10$ GHz. These values of $\beta_{\rm sync}$ seem to indicate a relatively small contribution of synchrotron emission, at least at high galactic latitudes, at CMB "optimal" frequency. This is also in agreement with [62, 33] who correlated *COBE*-DMR and Tenerife data with synchrotron template (the Haslam map) and found no significant correlation: an upper limits to synchrotron at 31.5 GHz of 11μK for galactic latitudes $|b| > 20^\circ$ is inferred by Kogut *et al.*[62].

For what concerns the angular distribution we estimate the angular power spectrum of the 408 MHz map including or cutting the contribution from the galactic plane. On the angular scales probed by the Haslam map (*i.e.* down to $\simeq 1^\circ$ resolution) the angular power spectrum is well described by a power law $C_\ell \propto \ell^{-\gamma}$ with an index $\gamma \simeq 2$. This is similar to what found by Lasenby [66] who considered 1-dimensional power spectrum of the Haslam map for the regions observed by the Tenerife experiment.

Free-free Emission When a free electron is accelerated by the Coulomb field of ions free-free emission results (see Fig. 2-10). In the astrophysical context this typically occurs when thermally hot ($\gtrsim 10^4$ K) electrons encounter with an ion, atom or molecule starting from an un-bound state and ending, after the interaction, in another un-bound state (hence the name free-free).

It is possible to calculate the amount of radiation emitted by a single electron, or a population of electrons, in astrophysical conditions [100]: one has to integrate over the total distribution of electrons and ions to derive the emissivity per volume along a given

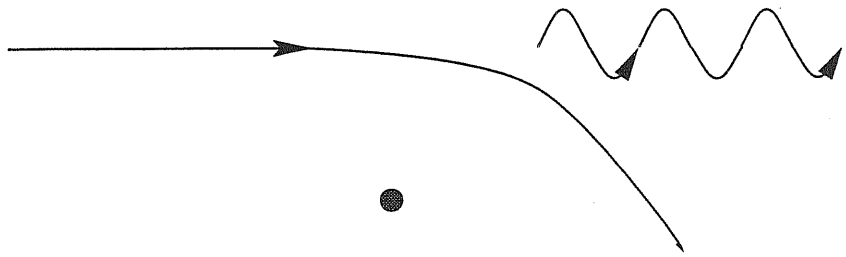

Figure 2-10: Schematic representation of the free-free emission

line of sight. This can be written [100]:

$$\alpha_\nu = \frac{4e^2}{3m_e hc}\left(\frac{2\pi}{3km_e}\right)^2 N_e N_i Z^2 T_e^{-1/2}\,\nu^{-3}\,(1-e^{-h\nu/kT_e})\langle g_{ff}\rangle \quad (2.27)$$

$$\approx 0.018\,Z^2\,N_e N_i\,T_e^{-3/2}\nu^{-2}\langle g_{ff}\rangle\,, \quad (2.28)$$

where we have assumed $h\nu \ll kT_e$ and $\langle g_{ff}\rangle$ is the velocity averaged Gaunt factor. Here h and k are the Planck and Boltzmann constants respectively, e is the electron charge and m_e its mass, N_i and N_e are the number of ions and electrons per unit volume, ν is the observing frequency and T_e is the electrons temperature. If we integrate the emissivity along the line of sight we obtain the optical depth τ:

$$\tau_\nu = 0.018\,T_e^{-3/2}\,\nu^{-2}\,\langle g_{ff}\rangle \int N_e N_i dl \quad (2.29)$$

$$\approx 0.08235\,T_e^{-1.35}\nu^{-2.1}EM\,, \quad (2.30)$$

where the emission measure $EM \equiv \int N_e N_i dl$ is in units of [cm^{-6} pc] and the exponents of both T_e (units of 10^4 K) and ν (units of 10 GHz) includes the effect from the Gaunt factor [100]. Here we have assumed that the astrophysical plasma is neutral, the electrons temperature is almost constant along the line of sight and not exceeds 20 K, and that frequency is less than 100 GHz. Once we have the optical depth we are able to derive the brightness temperature for free-free emission:

$$T_b^{ff} \sim 26\mu K\,\nu^{-2.1}\,T_e^{-0.35}EM\,. \quad (2.31)$$

Galactic free-free arises from two distinct components: one discrete and one diffuse. The former is clearly associated with HII regions. These are regions of intense star formation where hot electrons are present and radiate via thermal bremsstrahlung. These are highly concentrated along the galactic plane, $|b| < 5°$, with very few exceptions (*e.g.* the Orion Nebula). In a recent work Paladini *et al.*[84] have produced a new catalogue of $\sim$ 1200 HII sources in the microwaves (at 2.7 GHz) mainly along the galactic plane. Since free-free emission is not polarized, HII sources are a valuable source of calibration for polarized CMB measurements at sub-degree angular resolution. Their time stability and relatively large fluxes allow also a relative calibration for CMB temperature anisotropy data .

As for the diffuse component from Fig. 2-7 it is clear that there is no frequency window in which free-free emission dominates over synchrotron or dust emissions. This is the

main reason why, up to now, no full-sky maps of free-free emission are available. One would expect that at high galactic latitudes and at relatively high frequencies, free-free emission dominates over the synchrotron component and, combining multi-frequency data, it would be possible to separate the two by means of their different spectral behavior. Unfortunately, the baseline (zero-level) uncertainty in present available sky surveys (*e.g.* 408, 1420 and 2326 MHz maps) are poorly known and therefore of no use in this respect.

A good tracer of the diffuse free-free emission is the diffuse galactic Hα emission [113]: in fact both emissions are likely produced by the same gas and both are proportional to the EM. Measurements of Hα are very difficult because of the large contamination from strong geocoronal emission and the OH night-sky emission at 6568.68Å very close to $\lambda_{H\alpha} = 6583$Å. Nonetheless the situation is expected to improve very rapidly: for example the WHAM project (Wisconsin H Alpha Mapper) [96] will produce a map of the Hα norther sky emission with an angular resolution of about 1°; similar project are on-going for mapping the souther hemisphere Hα emission [78].

The intensity of the Hα line is proportional to the gas temperature and electrons density along the line of sight:

$$I_{H\alpha} = 0.36\,(EM)\,T^{-\gamma}\,R\,, \tag{2.32}$$

where EM and T have the usual units and R is the emission at $\lambda_{H\alpha}$ in units of 2.41×10^{-7} erg/(cm^2 std) or Rayleigh. This is valid for $T \leq 2.6 \times 10^4$ K and γ between 0.9 and 1.2. From Eq.(2.32) we obtain the brightness temperature

$$T_b^{ff} = 1.68\mu\mathrm{K}\,\langle g_{ff}\rangle T^{0.4\,\mathrm{to}\,0.7}\lambda I_{H\alpha}\,, \tag{2.33}$$

with λ in cm and $I_{H\alpha}$ in Rayleigh. The Hα can be modelled at first order as a layer parallel to the galactic plane with a law $T(b) \propto \csc|b|$: in fact the plane is optically thick to Hα but at high galactic latitudes there is in general low absorption. From the Hα data, Bennet *et al.*[5] estimated a contribution to antenna temperature at 53 GHz of $T_A(\mu\mathrm{K}) \approx 7\csc|b|$ for $|b| > 15°$.

Since no spatial template for free-free emission is available, any estimations of free-free emission in microwave data require pixel-by-pixel frequency analysis. Recently Kogut *et al.*[63] have cross-correlated *COBE*-DMR data at 31.5, 53 and 90 GHz with DIRBE data at 100, 140 and 240μm and found a statistically significant emission at each DMR frequency whose spatial distribution is well traced by dust emission on angular scale larger that 7°. Modelling the emission with both a dust and a radio emission they found a spectral index for the radio component of $\beta_{\mathrm{radio}} \simeq -2.1^{+0.6}_{-0.8}$ in good agreement with the theoretical index for free-free. This result is extended by Leitch *et al.*[68] and de Oliveira-Costa [31] down to 14 GHz founding a spectral index consistent with free-free emission at 95% confidence level.

If this is free-free emission one expects to find the same correlation with dust spatial template also in Hα data. However, even if there is an indication for this correlation, microwave results appear systematically higher. There is no full-sky map of Hα emission but a small region around the North Celestial Pole (NCP) is observed both in Hα [108] and in the microwaves [68]: the small variations in Hα are down by a factor 3-10 with respect the microwave emission and are inadequate to explain the presumed free-free emission. One could imagine that this emission originates from regions whose gas temperature is $T \simeq 10^6$ K (possibly near a SNR). In this way the Hα data would be consistent

with expected free-free emission. Such high gas temperature yields X-ray emission that should be detectable. In the region around the NCP the ROSAT 1/4 keV data yield an emission measure of about 0.023 cm^{-6} pc which, inserted into Eq.(2.31), produces a small contribution to the observed free-free emission.

These results are extremely interesting: microwave emission is correlated with dust showing a spectral index consistent with free-free emission but with a lower Hα emission than expected. So what could be? Recently Draine & Lazarian [35] suggested that this "anomalous" microwave emission could originate from both electric and magnetic dipole in small spinning dust grains. The relevant feature is that this emission peaks between 10 and 50 GHz depending on the grain size. This explanation is particularly attractive since it naturally explains the observed correlation with dust emission being originated by the same physical dust distribution. Furthermore it explains the lack of Hα emission without the requirement of high gas temperature which yield energetic problems (it would require an energy a factor of 10^2 larger than the estimated rate from supernovae).

As for the small angular scales behavior, Kogut *et al.*[62] have found that free-free emission angular power spectrum decreases as the third power of ℓ. This is what has been found for dust emission (see next section) from IRAS and DIRBE maps and it is another clue to the existing correlation between at least one component of free-free emission and dust emission.

Dust Emission Dust emission is of particular interest at high microwave frequencies ($\gtrsim$ 100 GHz) and PLANCK-LFI is marginally affected by this contamination. It originates from dust heated by the interstellar radiation field: dust absorbs UV and optical photons and re-emits them in the far-IR. The intensity depends upon gas chemical composition, dust to gas ratio, and grain composition, dimension and structure. Thus variations from place to place are expected. The IR intensity from a population of dust particles with size distribution $f(a)$ with radius a between $a_{min} \leq a \leq a_{max}$, and dust-to-gas mass ratio Z_d is usually written as

$$I(\nu) = \frac{\mu m_{\rm H} Z_d}{\langle m_d \rangle} N_{\rm H} \int_{a_{min}}^{a_{max}} da\, f(a) \sigma(a,\nu) \int dT P(a,T) B_\nu(T)\,, \tag{2.34}$$

where μ is the atomic weight of the gas, $N_{\rm H}$ is the total H column density, $\langle m_d \rangle$ is the size-averaged mass of the dust population, $\sigma(a,\nu)$ the dust particle cross-section at radius a and frequency ν, $B_\nu(T)$ is the Planck function at temperature T and $P(a,T)dT$ is the probability for a dust particle to have a temperature between T and $T + dT$. In case of dust radiating in thermal equilibrium at $T_{\rm eq}$, the $P(a,T)$ function is a simple delta function at $T = T_{\rm eq}$.

Recent analysis of *COBE* DIRBE (Diffuse Infrared Background Experiment) and FIRAS observations, together with IRAS data, by Dwek *et al.*[36] provides dust spectrum spanning the 3.5-1000μm wavelength regime. They derive a model for dust emission in which beside the usual bare silicate and graphite grains, polycyclic aromatic hydrocarbons (PAHs) are considered. At wavelength above 140 μm the model is dominated by the emission from graphite ($T \sim 17 - 20$ K) and silicate grains ($T \sim 15 - 18$ K). Kogut *et al.*[60, 62], using *COBE* DMR and DIRBE data, found that at high galactic latitudes, the dust emission can be modeled as a modified blackbody with a dust temperature of 18 K and an emissivity proportional to ν^2.

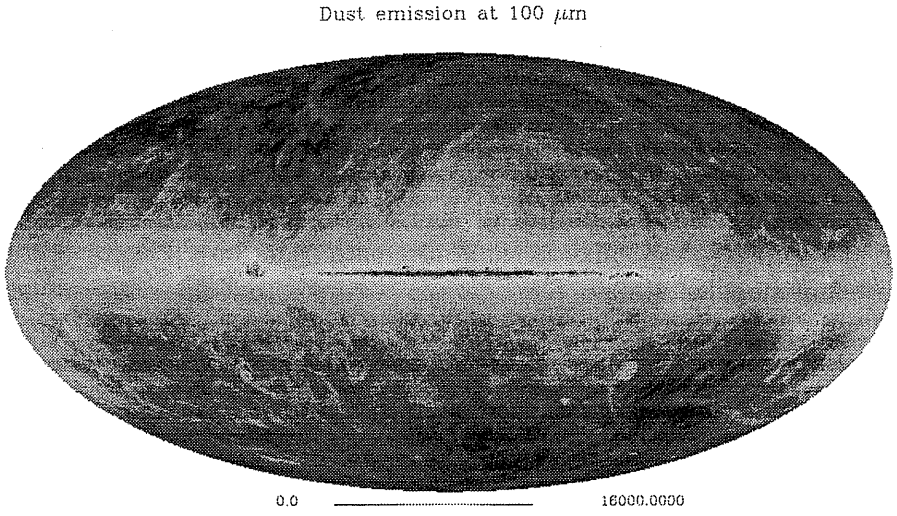

Figure 2-11: Dust emission at 100μm. Units of MJy/sr.

More recently Schlegel *et al.*[102] have produced a map at 100μm exploiting the IRAS and *COBE*-DIRBE data. After destriping the IRAS data and point source removal, the final map results to have nearly the IRAS angular resolution (6.1′) with the calibration accuracy of DIRBE data (see Fig. 2-11). In the case of an emissivity ν^2 they also provide a map of the dust temperature distribution over the whole sky. In general the expression in Eq.(2.34) can be approximated by a modified blackbody law:

$$I(\nu) \propto \nu^{\alpha} B_{\nu}(T_d) \tag{2.35}$$

where ν is the observing frequency, α is the emissivity index and T_d is the dust temperature.

However Finkbeiner *et al.*[40] exploiting the *COBE*-FIRAS data found that the ν^2 emissivity is inconsistent with emission between 100-2100 GHz and also that no power law emissivity model can explain the full spectral range of dust emission. However they found good agreement between data and a two-component dust model. They refer to the two components as amorphous silicate component, $\nu^{1.7}$ and $\langle T_d \rangle \simeq 9.5$ K, and a carbonaceous components, $\nu^{2.7}$ and $\langle T_d \rangle \simeq 16$ K. Using this model they predict the emission at each DMR frequency: they found that observed emission is a factor 1.2, 2.4 and 20 larger than their prediction at 90, 53 and 31.5 GHz respectively. There is more dust-correlated emission than predicted. They compared their prediction also at 14.5 and 32 GHz and found similar excess. Such an excess is spatially correlated with dust but usual thermal vibrational dust emission is not able to account for the observed signal. As already mentioned emission from ultra-small spinning dust grains togheter with magnetic dipole emission from paramagnetic grain could explain the observed microwave emission.

Analysis of the IRAS data [48] have found an angular power spectrum for the dust emission of the form $C_\ell \propto \ell^{-3}$ confirmed by DIRBE data [131].

Spinning dust grains In general there are three distinct mechanisms by which dust can radiate in the microwaves [35]: "vibrational electric dipole" emission (the usual dust emis-

sion due to thermal fluctuations in the charge distribution in the grain), "magnetic dipole" emission (due to thermal fluctuations in the magnetization of the grain) and "rotational electric dipole" emission (due to the rotating electric dipole in spinning grains). The usual vibrational emission falls very rapidly at microwave frequencies. If grains contain large fraction of magnetic materials, "magnetic dipole" emission could contribute in a significant way to microwave emission. There is recently [39] a large evidence for ultra-small dust grains. These grains can spin very rapidly and, having an electric dipole, should radiate at microwave frequencies. In particular the last mechanism could explain the "anomalous" component in the microwave sky emission reported in the previous paragraph.

Draine & Lazarian [35] have computed the emissivity from spinning dust grains for different grain sizes a and grain dipole moment β. Assuming that the grain angular velocity follow a Boltzmann distribution, they found:

$$j_\nu = \left(\frac{8}{3\pi}\right)^{1/2} \frac{1}{c^3} \int da f(a) \frac{\mu^2 \omega^6}{\langle\omega^2\rangle^{3/2}} \exp\left(\frac{-3\omega^2}{2\langle\omega^2\rangle}\right), \tag{2.36}$$

where μ is the intrinsic dipole moment of uncharged grain ($\mu \simeq \beta N^{1/2}$ where N is the total number of atoms in the grain) and $f(a)$ is the usual grain size distribution. With this expression and using the grain size distribution as inferred from IRAS data at 12 and 25μm, they shown that a large electric dipole emission could be produced by spinning grains in the 10-100 GHz range. In particular this emission well explain the observed emission between 30 and 50 GHz as from *COBE*-DMR and Saskatoon data.

The possibility to test the existence of these spinning dust grains are measurements at frequencies below 20 GHz where a turn in the spectrum is expected. Recently de Oliveira-Costa *et al.*[33] have considered the Tenerife data at 10 and 15 GHz. They found that free-free emission is not able to explain the ratio of the emission between 10 and 15 GHz yielding a larger 10 GHz signal than observed. Furthermore the spectral index between 10 and 15 GHz is not consistent with free-free emission and they claimed that this emission is an evidence of spinning dust grains emission. However it is worth to note that they collected data from different experiments probing different angular scales and this makes much more difficult to obtain a reliable estimation of the microwave emission spectral index.

2.6.2 Extra-Galactic Foregrounds

Extra-galactic sources Beside galactic foreground emission, another unavoidable fundamental limitation for CMB measurements is set by extra-galactic sources. Because of the large beam size, the *COBE*-DMR data are mainly affected by diffuse galactic foreground (e.g. [63]) and practically uncontaminated by extra-galactic sources [2, 61]. On the contrary, extra-galactic foregrounds are expected to be a major problem for future high-resolution CMB experiment like MAP and PLANCK with sensitivity of $\Delta T/T \simeq 10^{-6}$ as well as for some balloon experiments.

The issue of small scales fluctuations due to extra-galactic sources has been long discussed in literature ([42, 115, 117] and references therein). These studies provide an important result: due to the sharp rise in the dust spectrum with increasing frequency ($S_\nu \propto \nu^{3.5}$), a different composition of bright sources below and above $\simeq$ 200 GHz shows

up. Radio sources ("flat"-spectrum radiogalaxies, BL Lacs objects, blazars and quasars) dominate at low frequency while dusty galaxies at high frequencies.

As for radio source, observed counts are available at different frequencies ranging from 408 MHz to 8.44 GHz and reach very deep flux levels which are far from PLANCK sensitivity.

We have to extrapolate source counts at PLANCK frequencies and the spectral behavior of these sources at high frequencies is the key issue. In this extrapolation several effects need to be considered. On one hand a large fraction of sources with flat or inverted spectra at 5 GHz have turnover frequency below 90 GHz. On the other hand high frequency survey select sources with hard spectra. For a power law source counts $n(s,\nu_0) = k_0 S^{-\gamma}$ and a gaussian spectral index distribution with mean α_0 and dispersion σ, the counts at a frequency ν are given by:

$$n(S,\nu) = n(S,\nu_0)\left(\frac{\nu}{\nu_0}\right)^{\alpha_{\rm eff}}, \tag{2.37}$$

where $\alpha_{\rm eff} = \alpha_0 + \ln(\nu/\nu_0)\sigma^2(1-\gamma)^2/2$. Therefore source counts estimations neglectic this dispersion of spectral indices, underestimate the counts by a factor of $\exp[\ln^2(\nu/\nu_0)\sigma^2(1-\gamma)^2/2]$. For example the spectral index distribution between 5 and 90 GHz has a dispersion $\sigma = 0.34$ which, for Euclidean counts with $\gamma = 2.5$, translates into a correction of about a factor of 3.

Due to the large uncertainties on the spectra of most of the radio selected AGN and poor knowledge of counts for inverted spectra sources, a comprehensive model of source counts at $\nu \sim 100$ GHz is, at the moment, impossible. However the model adopted by Toffolatti *et al.*[117] seems to be remarkably successful. They compute radio source counts using the simple recipe by Danese *et al.*[25] in which a spectral index $\alpha = 0$ for "flat"-spectrum source up to 200 GHz is assumed and then a steepening to $\alpha = 0.75$ occurs. This simple model properly accounts for deep source counts at 8.44 GHz which were produced long after the model. This model implies a substantial contribution of active star-forming galaxy to sub-mJy counts at cm wavelengths. This is consistent with results from Kron *et al.*[64] which indicate that the optical counterpart of the sub-mJy source are in fact faint blue galaxies, often showing peculiar morphologies and high star formation activity. This evidence is also supported by a recent work by Gruppioni, Mignoli & Zamorani [51] where they found that the majority of radio sources with flux limit of 0.2 mJy are early type galaxies.

The situation is worse for dusty galaxies since evolutionary properties are poorly known and source counts are very evolution-sensitive. The largest survey available is provided by IRAS at 60μm which however covers a limited range of fluxes. The situation is improving thanks to the ISO-CAM, ISO-PHOT and SCUBA data [44] limited to small sky areas. Predicted counts are strongly sensitive to poorly known evolutionary properties due to boosting effects and large negative K corrections. It is therefore not surprising that model counts predictions may differ by substantial factors. Substantial extrapolation has to be made which is very uncertain due to the poorly known spectrum of galaxies in the mm/sub-mm region: for example the flux ratio 1.3mm/60μm is observed to span about a factor of 10 ([43]).

Toffolatti *et al.*[117] provided, in the context of the PLANCK mission, the number of counts for both radio sources and dusty galaxies and found that radio sources dominate

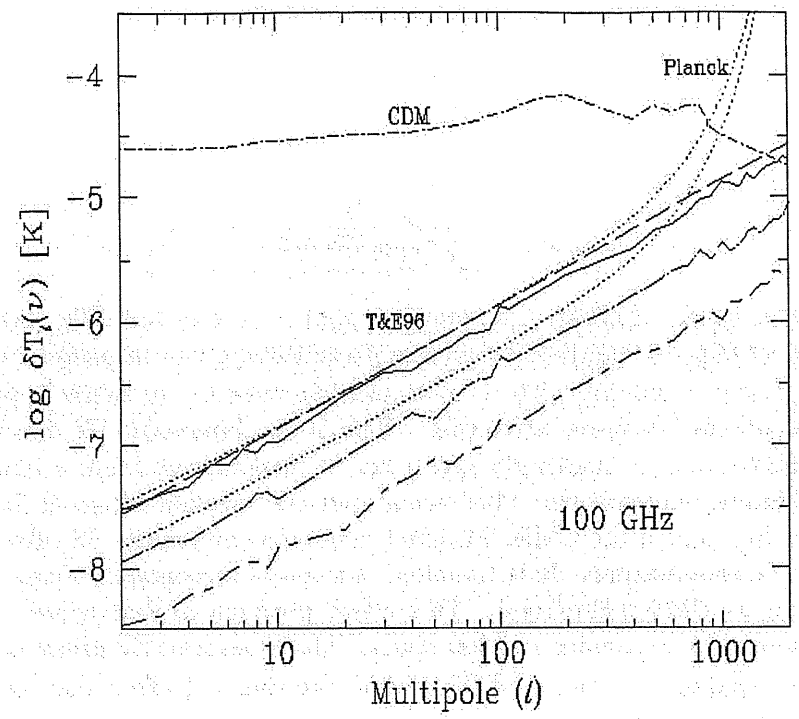

Figure 2-12: Angular power spectrum from a Poisson distribution of point sources at 100 GHz for three different values of flux limit for source removal (1, 0.1 and 0.01 Jy). Dotted lines are unsmoothed noise spectra, thin long-dashed is from [115] and dot-dashed is a standard CDM model (from Toffolatti *et al.*[117]).

the counts up to 200 GHz and this will allow a direct measurement of the high frequency tail of their poorly known spectra. These estimates indicate that at high galactic latitudes, extra-galactic sources are the major source of foreground fluctuations for angular scales $\lesssim 30'$. These results are reported synthetically in Fig. 2-12 where the angular power spectrum for extra-galactic sources is computed at 100 GHz, for three different values of limit flux for source removal, and compared with noise as well as primary CMB spectra.

These results show that amplitude of fluctuations due to extra-galactic sources in the range 100-200 GHz are well below the primary CMB signal.

The Sunyaev-Zel'dovich effect Another important foreground for CMB anisotropy measurements are cluster of galaxies. In fact when CMB photons interact with hot ionized gas in clusters of galaxies, they suffer inverse Compton scattering. Cold photons, like the CMB ones, passing trough hot gas gain energy and shift towards higher temperatures. Therefore there are less photons at low frequencies while at higher frequencies there will be an excess of CMB photons resulting in a cold or hot spot in the CMB field. This is the well known Sunyaev-Zel'dovich effect and results in a frequency dependence of the spectrum which reads:

$$\Delta I = \frac{2(kT)^3}{(hc)^2} y\, g(x)\,, \tag{2.38}$$

where T is the CMB temperature, ν is the observing frequency, y is the usual Compton-isation parameter while $g(x)$ is a function of the dimensionless frequency $x = h\nu/kT$ of

the form:

$$g(x) = \frac{x^4 e^x}{(e^x - 1)^2} \left[x \coth\left(\frac{x}{2}\right) - 4 \right] . \tag{2.39}$$

This is the thermal SZ effect. The function $g(x)$ is null at 217 GHz and therefore the SZ thermal effect can be identified by means of multifrequency measurements.

If the cluster is moving with its own peculiar velocity, an extra Doppler effect results because of simple Thomson scattering. This is the kinematic SZ effect which does not cause deviation from a blackbody spectrum. It however produces a blackbody spectrum with an different temperature. This means that the spectral shape of the kinematic effect is exactely the same of the CMB. This fact makes the kinematic SZ effect one of the worst foreground contaminations. It is therefore extremely important to clearly understand its contribution to CMB anisotropy. This effect produce in fact a red shift of the order $v_{\rm bulk}/c$ where $v_{\rm bulk}$ is usually $\lesssim 1000$ Km/s. The kinematic SZ effect is usually, for most frequencies, smaller by a factor of 10 or more the thermal effect and therefore has a little impact on CMB anisotropy.

The SZ arises from CMB interacting with gas in clusters of galaxies and therefore we expect that the power spectrum of the anisotropy follows that of the gas. Since clusters of galaxies are Poisson distributed, like extra-galactic sources, the angular power spectrum of the SZ effect should be constant with ℓ like white noise. The relevant angular scales are those of cluster angular dimensions ($\lesssim 10'$) which are below the scale where Silk damping has erased CMB anisotropy: this should dominate sky fluctuations on very small angular scales.

2.7 Synthetic sky maps[1]

In the rest of this thesis accurate simulations of the PLANCK-LFI observations are performed. For making realistic prediction of LFI capabilities and the relevant impact of systematic effects, it is extremely important to produce the most realistic microwave sky. This in fact will produce estimation of LFI performances in a "real" world with both foregrounds and systematic effects contaminations which depend on the assumed sky model (*e.g.* stray-light). Furthermore accurate foreground models would be a good starting point for a foreground removal technique that will be applied to real CMB data.

Synthetic sky should include CMB fluctuations, galactic and extra-galactic foregrounds. As for CMB, fast codes are now available which, within the inflationary paradigm, are able to compute the CMB angular power spectrum up to very high ℓ on time-scales of minutes (*e.g.* CMBFAST [132]). Pixelization packages [50] currently available can produce a full-sky map of the CMB starting from C_ℓ with the desired angular resolution in very short time scales. A standard CDM model normalize to *COBE* data is used for simulations of the CMB anisotropy.

In this thesis we do not consider the contribution from unresolved point sources as predicted by Toffolatti *et al.*[117]. However it will be possible to include their contribution to microwave sky fluctuations for more complete simulations that will be soon performed.

[1]Based on D. Maino *et al.*, *A&A* in preparation; presentation at the PLANCK-LFI Consortium Meeting, Capri, 7-9 October 1999

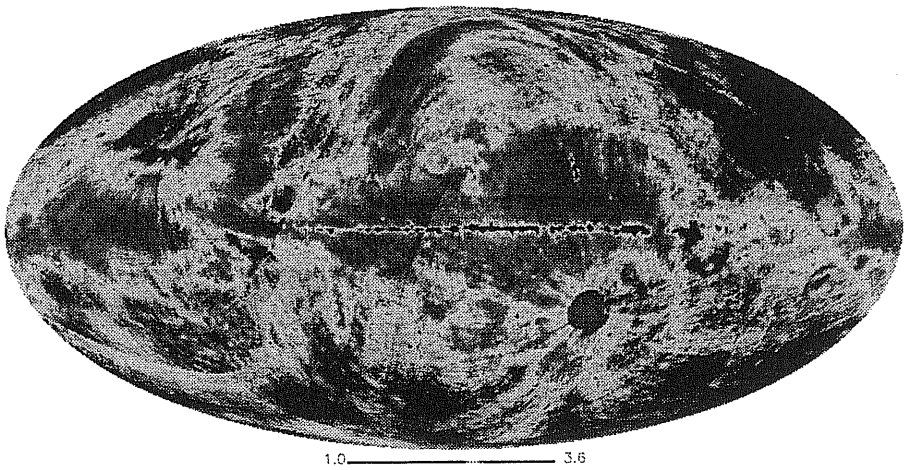

Figure 2-13: Synchrotron spectral index between 408, 1420 and 2326 MHz. A fit to a power law is adopted when three data points were available. Stripes are still present also in the cleaned 408 and 1420 MHz maps.

Galactic foregrounds are considered. As for dust emission we make use the results from Schlegel *et al.*[102], to extrapolate the intensity at 100μm at CMB frequencies using the spatial distribution of the dust temperature. We adopted the intensity law in Eq.(2.35) together with the dust temperature map. In this way we produce a model of dust microwave emission which takes into account the spatial variations of dust temperature. The map from [102] has an angular resolution of $6.1'$ which is adequate for PLANCK-LFI simulations and therefore we do not need to extrapolate the dust emission at smaller angular scales.

Free-free emission lacks a spatial template. We do not consider the diffuse free-free emission but include only the contribution from HII regions in the new catalogue from [84]. The contribution is scaled down to PLANCK-LFI frequencies with the theoretical free-free spectral index.

Synchrotron emission is well traced by the Haslam map at 408 MHz. We shown that the synchrotron spectral index is spatially variable and steepens at higher frequency. In order to gain information its properties we considered the de-stripped 408 and 1420 MHz together with the 2326 MHz to study the distribution of the spectral index $\beta_{\rm sync}$ all over the sky. Both the Haslam and Reich & Reich maps are corrected for extra-galactic contributions as well as for zero-level uncertainties. Problems arise with the 2326 MHz map which is large contamined by striping effect and calibration accuracy.- In regions covered by the three surveys we evaluated $\beta_{\rm sync}$ by means of a power law fit of the brightness temperature at the three frequencies; where only two surveys cover a certain region we used

$$\beta_{\rm sync} = \frac{\log(T(\nu_1)/T(\nu_2))}{\log(\nu_2/\nu_1)}\,, \tag{2.40}$$

where $T(\nu_1)$ and $T(\nu_2)$ are the brightness temperature at the two frequencies ν_1 and ν_2.

Our estimated value for $\beta_{\rm sync}$ are mapped as in Fig. 2-13: this result is very preliminary

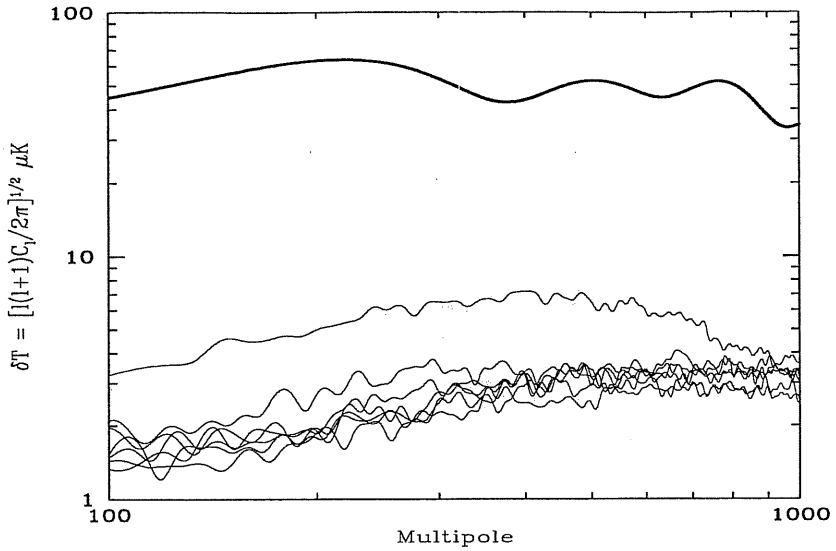

Figure 2-14: Comparison between CMB and synchrotron power spectrum as extracted from several high galactic latitudes regions from the 2326 MHz map and scaled to 30 GHz with a $\beta_{\rm sync} = 2.9$ spectral index

and values range from 1.0 to 3.5. The lowest value is mainly located in the sources along the galactic plane and it is misleading. In fact point sources are removed from the de-stripped 408 and 1420 MHz maps but are still present in the 2326 MHz map. However there are region with low spectral index at high galactic latitudes. It is important to remind that the 2326 MHz map is strongly affected by striping effect and gain uncertainties and has to be cleaned as the 408 and 1420 MHz maps. This cleaning technique implemented by Davies *et al.*[27] however leaves residual stripes and has to be improved. It is possible to state that a general steepening of the spectral index is observed when the 2326 MHz data are included.

Using this result, altough with great care since it is very preliminary, it is possible to produce a synchrotron map at PLANCK-LFI frequencies using the Haslam spatial template and this distribution of the synchrotron spectral index.

As reported in Table 2.1 the Haslam map has a poor angular resolution which is far from the one of PLANCK-LFI and small angular scales extrapolation is needed. We want to check if the $C_\ell \propto \ell^{-2}$ found from the Haslam map is confirmed also at higher value of ℓ. The survey with the best angular resolution is the Jonas *et al.*[58] map which has $20'$ resolution. There is also another survey with a resolution of $10'$ which however covers only a region along the galactic plane: this is the Parkes survey at 2.4 GHz [37] which is less effected by zero-level and gain uncertainties being limited to a small fraction of the sky. Therefore these data are in principle more reliable than the 2326 MHz data. From these two maps we extract several patches of $10^\circ \times 10^\circ$ and compute their angular power spectrum. In regions covered by both surveys the recovered power spectrum shows a good agreement thus checking the consistency between the two maps. We therefore extract high galactic latitude patches from the 2326 MHz map and, in Fig. 2-14, we compare these synchrotron power spectra with the one of the CMB scaled at 30 GHz. It is interesting to note that up to very high ℓ the synchrotron power spectrum has a slope

$\gamma \simeq 2$. Furthermore for clean sky regions the δT level is almost the same as in Fig. 2-14 where a large contamined region is included (the highest spectrum). The resulting level of synchrotron fluctuations is ~ 10 times smaller that of CMB yielding the possibility that synchrotron emission should not be a real problem at CMB frequencies.

This is the general recipe we used to produce synthetic microwave sky emission at PLANCK-LFI frequencies. Of course improvements are possible and as new data are published we upgrade our model.

Chapter 3

The PLANCK mission and the Low Frequency Instrument

This chapter summarizes the concept of the PLANCK mission. Particular attention is devoted to the scanning strategy and to the design and capabilities of LFI.

The choice of the scanning strategy is a key issue and still open within the PLANCK collaboration. One of the major requirements for the scanning strategy is that it should allow a complete sky coverage with enough redundancy to control foregrounds and systematic effects. Rejection of different systematic effects are probably optimized by different scanning strategies, thus yielding possible trade-offs which have to be carefully considered.

This chapter is organized as follows: §3.1 introduces the main properties of the two PLANCK instruments; §3.2 describes in detail the chosen orbit and the adopted scanning strategy. The telescope and focal plane arrangement is in §3.3 while §3.4 reports a description of the LFI instrument and §3.5 its scientific capabilities. An introduction to the systematic effects addressed in this thesis is in §3.6. In §3.7 the PLANCK flight simulator implemented for the simulations presented in this thesis is described.

3.1 The PLANCK concept

We have described in Chapter 2 which are the main fundamental limitations in CMB anisotropy measurements: cosmic and sample variance, detectors sensitivity and foregrounds contamination. Systematic effects are another key issue. These considerations force an "ultimate" CMB experiment to satisfy the following requirements:

- nearly complete sky coverage to avoid sample variance;
- large frequency range to control and separate foreground emissions from cosmological signal;
- low contribution from ground and atmospheric emission;
- high control on systematic/instrumental effects;
- high sensitivity and resolution for high accuracy on C_ℓ.

Frequency [GHz]	30	44	70	100
Number of detectors	4	6	12	34
Number of polarized detectors	4	6	12	34
Angular resolution [′]	33	23	14	10
Bandwidth $[\Delta\nu/\nu]$	0.20	0.20	0.20	0.20
Noise/res. elements 12 months [μK]	4	7	10	12

Table 3.1: Summary of the potential LFI performances

Frequency [GHz]	100	143	217	353	545	857
Number of detectors	4	12	12	6	6	6
Both polarisations	no	yes	yes	no	yes	no
Angular resolution [′]	10.7	8.0	5.5	5.5	5.5	5.5
Bandwidth $[\Delta\nu/\nu]$	0.25	0.25	0.25	0.25	0.25	0.25
Noise/res. elements 12 months [μK]	5	6	12.5	41	393	12630

Table 3.2: Summary of the potential HFI performances

Danese *et al.*[26] claimed that only a space mission can satisfy at the same time these requirements: PLANCK is designed to be such a mission. PLANCK is the merger of two independently proposed missions: COBRAS (COsmic Background Radiation Anisotropy Satellite [73]) and SAMBA (SAtellite for Measurements of Background Anisotropy [93]). These two missions now form respectively the PLANCK LFI (Low Frequency Instrument) and HFI (High Frequency Instrument). LFI and HFI are based on different technologies: microwave radiometers with HEMT (High Electron Mobility Transistor) amplifiers cooled at 20 K (LFI) and spider-web bolometers cooled at 0.1 K (HFI). The need of high sensitivity drives the choice of detector arrays cooled to cryogenic temperatures. PLANCK covers the extremely wide frequency range from 30 to 857 GHz: this allows high control of foreground contaminations and their separation from CMB signal. The angular resolution ranges from $30'$ to $5.5'$. Tables 3.1 and 3.2 report a summary of LFI and HFI nominal properties: average sensitivity per resolution element over the whole sky is reported. Note that a large number of detectors operate between 70 and 217 GHz: this is a frequency range particularly suitable for direct CMB measurements since the expected level of foregrounds (both galactic and extra-galactic) is below the CMB signal ([26]; see also Chapter 2). LFI and HFI deal with different astrophysical processes and therefore they need one another to optimally separate cosmic signal from foreground contaminations.

It is worth mentioning that Tables 3.1 and 3.2 report the nominal expected performances *i.e.* assuming the detector white noise is the actual limit to the sensitivity per pixel. Possible systematic effects can in fact degrade, for example, the angular resolution or the sensitivity per resolution element in a considerable way thus possibly compromising mission goals. An observing strategy which allows repeated observations of sky pixels by several detectors at different frequency on many time scales is required. In such a way it is possible to achieve an high control of systematic effects and their characterization for a meaningful subtraction.

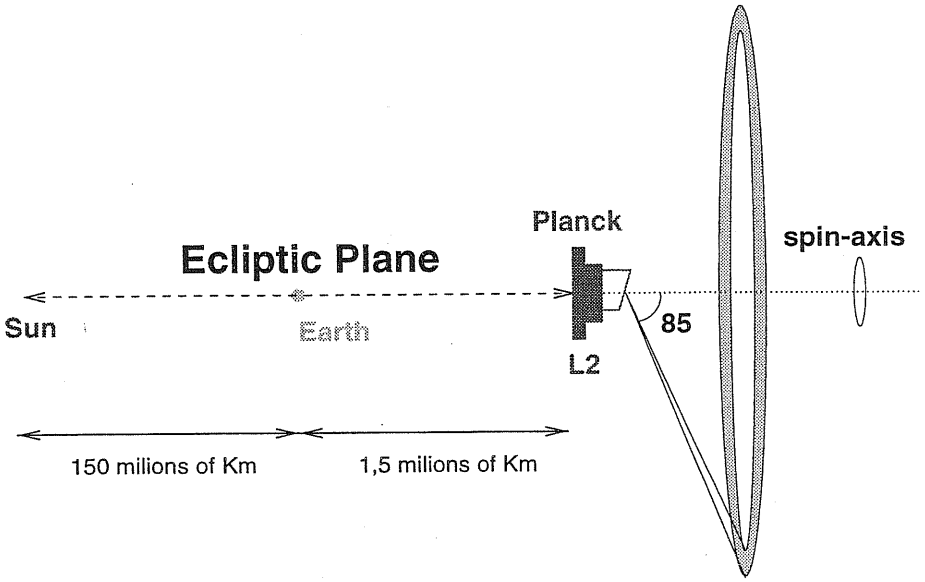

Figure 3-1: Schematic representation of the adopted PLANCK scanning strategy.

The combination of both instruments data give to PLANCK the imaging power (*i.e.* the CMB angular power spectrum down to $\ell \sim 2000$), the proper redundancy and control of systematic effects and foreground emissions (*i.e.* final sensitivity limited by cosmic variance and astrophysical foregrounds) which make PLANCK the *definitive* CMB anisotropy mission.

3.2 Orbit and scanning strategy

PLANCK is a spinning space-craft which will be located in a tight Lissajous orbit near the Earth-Sun Lagrange point L_2. The spin-axis is oriented in the anti-Sun direction and the bore-sight angle α between pointing and spin-axis in the current baseline is 85°. The requirement of low contribution from Sun, Earth and Moon (a critical issue for *COBE* because of its Low Earth Orbit) is the primary reason for the far-Earth orbit selection around L_2 ($\sim 1.5 \times 10^6$ Km). From L_2 the solid angle of Earth and Moon is dramatically reduced and also the Sun has nearly the same angular size. This considerably reduces the total amount of radiation from Sun, Earth and Moon that reaches, either directly or by diffraction and scattering, the detectors.

In the simplest scanning strategy the spin-axis moves about 2.5′ every hour along the Ecliptic plane to keep the anti-solar orientation while the spacecraft spins at 1 r.p.m.; great circles are traced in the sky which have intersections in a region close to the Ecliptic polar caps. A schematic representation is in Fig. 3-1. Since each circle is observed many times on different time-scales, possible instrumental drifts on time-scales larger than the spinning period can be easily removed. Problems may arise when drifts have a characteristic time-scale equal or smaller than the spinning period and moving the spin-axis away from the Ecliptic plane may help in removing these drifts (see Chapter 6 for further details). In this respect sinusoidal oscillations of the spin-axis as well as precession have been considered:

between the two, precession is preferable since it preserves the solar aspect angle thus not inducing any thermal modulation. Thermal stability is another key issue: the closer the spin-axis is maintained along the Sun-PLANCK direction, the smaller will be temperature modulations which may be source of possible systematic effects. Since with $\alpha = 85°$ small regions around the Ecliptic polar caps are left unobserved, with a spin-axis precession it is possible to obtain a nearly full-sky coverage.

For a proper reconstruction of CMB temperature anisotropy PLANCK requires an accurate calibration which converts signal from raw telemetry into physical units. Each detector has to be accurately calibrated on a time scale as short as possible. Stable celestial sources with adequate intensity which are observed during the mission are suitable for calibration. One of this is the CMB dipole whose amplitude and direction are known with an accuracy of 1%. Because of the scanning strategy PLANCK will continuously observe the CMB dipole allowing for a good calibration accuracy on time scale of few hours for LFI. The dipole is in fact the best celestial calibrator since it has the same spectral shape of the signal we want to measure and it has a large pattern thus not depending on the beam size. Another source of absolute calibration is the CMB dipole modulation produced by the motion of the satellite around the Sun. The amplitude of the modulation is $\sim 270\mu$K and allows calibration on large time scales (> 6 months) with an accuracy of 0.2% [8]. Accurate simulations are currently being performed [21], in the context of LFI, to better quantify the achieved calibration accuracy over several time-scales from few hours to days.

3.3 Telescope and focal plane arrangement

In order to achieve the nominal angular resolution an optical system is required. Both LFI and HFI share the same optical system. The baseline currently under study is a 1.55 m projected aperture Gregorian off-axis telescope. The actual configuration of the focal plane is reported in Fig. 3-2: the round box in the center of the focal plane is occupied by the HFI instrument while LFI feed-horns are placed as a ring around it. The focal plane has a radius of about 5° when projected in the sky. Most of the LFI feed-horns are therefore at $2° \div 5°$ from the telescope axis. Furthermore the focal plane is in fact not plane because of the off-axis design of the telescope. The feed-horns have to be properly arranged in order to have their phase centers at the focal-surface of the telescope. The feed-horn aperture, the primary mirror aperture and the illumination (edge-taper) of the primary mirror set the effective angular resolution and the level of beam sidelobes. The former has to be as small as possible; the latter have to be as low as possible.

3.4 The Low Frequency Instrument

The actual design of the LFI radiometers has been proposed in order to minimize the effect of amplifiers instabilities (namely the $1/f$ noise) in the final radiometer output. We give here a brief description of the radiometer concept and how this is integrated in the PLANCK pay-load.

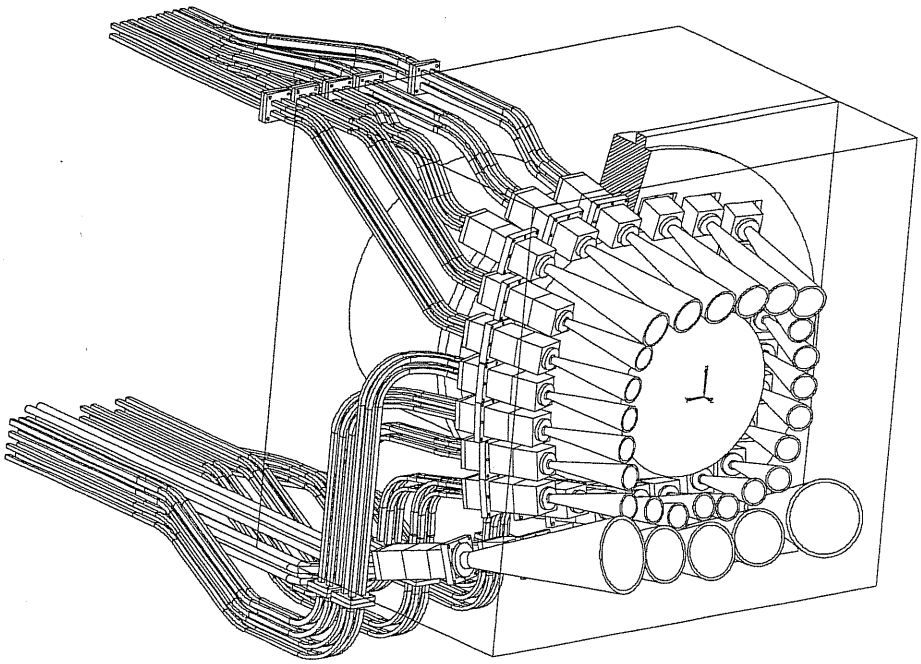

Figure 3-2: Schematic of PLANCK focal plane: the round box represents HFI in the center of the focal plane, LFI feed-horns are placed as ring around it.

3.4.1 Radiometer concept

The PLANCK-LFI radiometers are Blum correlation receivers [11, 22] known also as pseudo-correlation or continuous comparison receivers. A schematic representation is shown in Fig. 3-3. The radiometer has two inputs: the first looks at the sky through an orthomode transducer (OMT) and a feed-horn, and the second looks a reference load at a given temperature by means of a small horn. The reference load temperature is at $T_{\rm load} \equiv T_y \simeq 4$ K, exploiting the HFI 4 K cooling stage. This is somewhat different from the sky temperature $T_x \simeq 2.7$ K. However a back-up solution with $T_y \simeq 20$ K is already studied.

The OMT splits the two polarization directions of the signal, and sky and load signals, passing through the first hybrid coupler (see Fig. 3-3), go into the two "legs" of the receiver. The signals are amplified and phase shifted through a phase switch with fixed phase (90° or 180°). Then they pass through another hybrid which recombines the signals. After another amplification, the signal is converted by a detector diode. The output signal is proportional to the difference between the two inputs. This difference can be done in several ways: the one adopted for LFI takes successive measurements of each detector and makes the difference between them. Depending on the detector, and hence on the phase state, one of these signals corresponds to the sky and the other to the load. In order to further reduce the impact of spurious systematics, the best way is having a null output from the receiver. This can be achieved by adjusting the DC gain ratio r between the two legs at a value $r = (T_x + T_n)/(T_y + T_n)$ where T_n is the noise temperature. Best performances are achieved with a fully balanced radiometer with $T_y \approx T_x$ (*i.e.* with $r \simeq 1$).

The nominal sensitivity of a radiometer with the LFI design, in the ideal case of pure

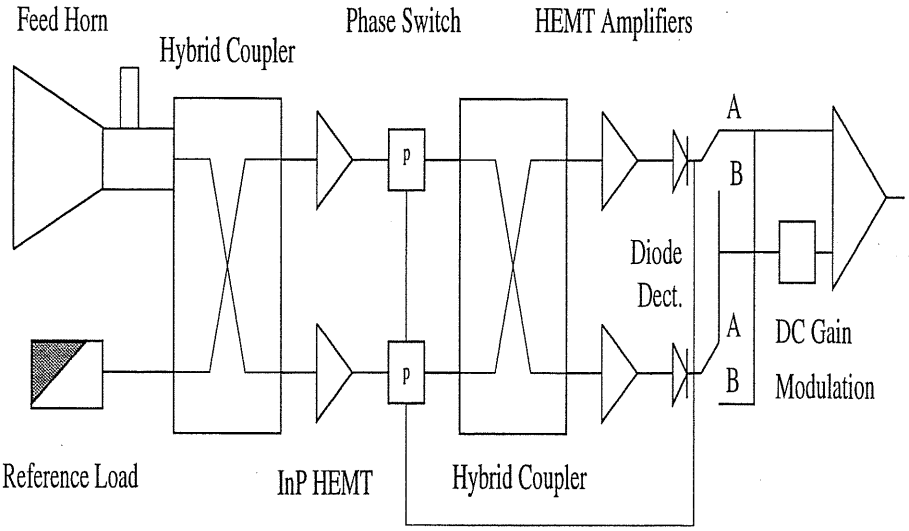

Figure 3-3: Schematic representation of the pseudo-correlation receiver used for LFI (Bersanelli *et al.*[5])

white noise, reads:

$$\Delta T_{\rm wn} = \frac{\sqrt{2}(T_x + T_n)}{\sqrt{B\tau}}, \tag{3.1}$$

where B is the bandwidth (usually 20% of the central frequency) and τ is the integration time. We will see in Chapter 6 how to properly characterize the noise behavior of LFI radiometers.

3.4.2 Radiometer description

The LFI radiometers are splitted into two parts: the front- and the back-end units. A schematic representation of the LFI front-end unit (FEU) is shown in Fig. 3-2. The FEU includes 28 modules allocated at the focus of an off-axis telescope; each module is composed by a feed-horn, an OMT, two hybrid couplers, two phase switches and four cryogenically cooled amplifiers.

The radiation collected by the telescope enters the radiometers by means of conical corrugated feed-horns ([10, 120]) whose radiation pattern has to be highly symmetric, with low sidelobes and a beam width which allows a level < -30 dB at 22° from the maximum directivity direction.

The 30 and 44 GHz amplifiers are InP (indium phosphide) HEMT incorporated into an integrated circuit (MIC) while at 70 and 100 GHz all the circuits are incorporated in a single chip using MMIC (monolithic microwave integrated circuit) technology.

The 28 front-end modules are mounted on a plate at 20 K and cooled at 20 K by a hydrogen sorption cooler [122]. This is a Joule-Thomson cooler in which the hydrogen expands from 6 MPa to 0.03 Mpa through a Joule-Thomson expander. This cooler also provides a 18 K precooling to the 4 K HFI cooler. This kind of cooler is particularly useful since combines high efficiency without moving parts and vibrations.

1-σ error	PLANCK-LFI^T	PLANCK-LFI$^{(T+P)}$
$\Delta \ln C_2$	0.13	0.031
$\Delta \ln h$	0.027	0.015
$\Delta \Omega_\Lambda$	0.083	0.046
$\Delta \ln (\Omega_b h^2)$	0.013	0.009
$\Delta \ln \tau_{ri}$	1.6	0.08
$\Delta \ln n_S$	0.008	0.004

Table 3.3: Fisher Matrix 1-σ errors for SCDM model for PLANCK-LFI specifications

The cold part is connected to the room temperature section (back end) of the LFI receivers by means of waveguides or cables: 20 cables and 92 waveguides are required for all the 28 LFI modules. Including the two hybrids in the FEU eliminates the need (and problems) of a phase matching of transmission path to back-end. The back-end include two parallel chains of amplification, filtering, detection and integration.

3.5 LFI Scientific capabilities

The primary goal of LFI is to map CMB anisotropy in four frequency bands (30, 44, 70 and 100 GHz), over nearly the entire sky, with resolution from $30'$ to $10'$ and with sensitivity per resolution element $\Delta T/T \sim 2 \div 4 \times 10^{-6}$. These measurements will yield a determination of the CMB power spectrum up to $\ell \sim 1000$ allowing for the extraction, with few percent accuracy, of the most important cosmological parameter like the Hubble constant, the primordial spectral index, the baryon and dark matter contents. LFI data are able to test the inflationary paradigm for structures formation *i.e.* whether they are due to primordial quantum fluctuations or topological defects like cosmis strings. CMB polarization measurements are possible in small sky regions ($25° \times 25°$) close to the Ecliptic polar caps where sensitivity is ~ 5 times better than the average considering the simplest scanning strategy without spin-axis wobbling. These regions are large enough to extract polarisation information which will help in breaking the degeneracy between cosmological parameters.

Maino *et al.*[71] estimated the errors on cosmological parameters expected from LFI data (both temperature and polarization) exploiting the Fisher Matrix formalism (see Appendix A for technical details). In this approach, a fiducial CMB anisotropy model is required as well as angular resolution and noise per resolution element of the considered experiment. Two cosmological models are considered here: a standard CDM model and a ΛCDM model. These model are specified by the Hubble constant h, the baryon content Ω_B, the cosmological constant Ω_Λ, the re-ionization optical depth τ, the primordial spectral index n and the spectrum normalization C_2 (see Table A.2 for numerical values for the two considered models). Table 3.3 and Table 3.4 report estimated errors on cosmological parameters, for the SCDM and ΛCDM model, derived from temperature and temperature plus polarization data. It is interesting to note how well is designed LFI since cosmological parameters are recovered with errors of few percent (a part τ and C_2 which are in fact degenerate) and the substantial improvement when including polarization data especially

1-σ error	PLANCK-LFI^T	PLANCK-LFI$^{(T+P)}$
$\Delta \ln C_2$	0.12	0.020
$\Delta \ln h$	0.026	0.015
$\Delta \ln \Omega_\Lambda$	0.030	0.018
$\Delta \ln (\Omega_b h^2)$	0.018	0.012
$\Delta \ln \tau_{ri}$	0.66	0.062
$\Delta \ln n_S$	0.012	0.007

Table 3.4: Fisher Matrix 1-σ errors for ΛCDM model for PLANCK-LFI specifications

for τ and C_2 since polarization breaks the degeneracy between the two.

LFI will detect few hundreds of galaxies clusters through their SZ effect and, together with X-ray data, will yield an independent determination of the Hubble constant. Flat-spectrum radiosource (compact radio-galaxies, QSO, BL Lacs and blazars) will be also observed by LFI in a particularly interesting spectral window where their spectral features (brakes for synchrotron ages, steepening for transition between optically thick/thin synchrotron emission and self-absorption) are manifest.

The four LFI maps will form a rich database for studies on Galaxy: the structure of the galactic magnetic field, the spatial and energy distribution of the cosmic-rays, the evolution and properties of the interstellar medium as well as supernova remnants, planetary nebulae and symbiotic stars.

3.6 Systematic effects

This section introduces those systematic effects which will be addressed in detail in this thesis: main beam distortion, $1/f$ noise and stray-light contamination.

Optical analysis of the PLANCK telescope design have shown that only in the very central part of the focal plane, the beam pattern of the feed-horn is symmetric. Beam aberrations, like coma, appear in LFI beams because of their off-axis position. The major effect of main beam distortions is a degradation of the effective angular resolution with respect to a beam located in the center of the focal plane. Since the need of high angular resolution, it is of great importance to consider both larger telescope apertures and different telescope designs which may improve the level of main beam distortions. In Chapter 4 we will address this issue in detail analyzing the impact of distorted beam, with elliptical approximations and with more realistic optical simulated beam shapes.

A particularly critical systematic effect is the stray-light. This is the radiation coming from off-axis sources through beam sidelobes. Several sources may introduce spurious signals and they can be both instrumental (internal stray-light) and astrophysical. As for the second, the major contributions come from an imperfect rejection by the optical system of signal from Sun, Earth, Moon, planets and Galaxy. Due to the adopted scanning strategy, the Galaxy will be continuously observed and sidelobes will pick-up galactic radiation producing artifacts. In Chapter 5 using a full antenna beam pattern at 30 GHz and a detailed model of the microwave emission of Galaxy, we will address the stray-light problem.

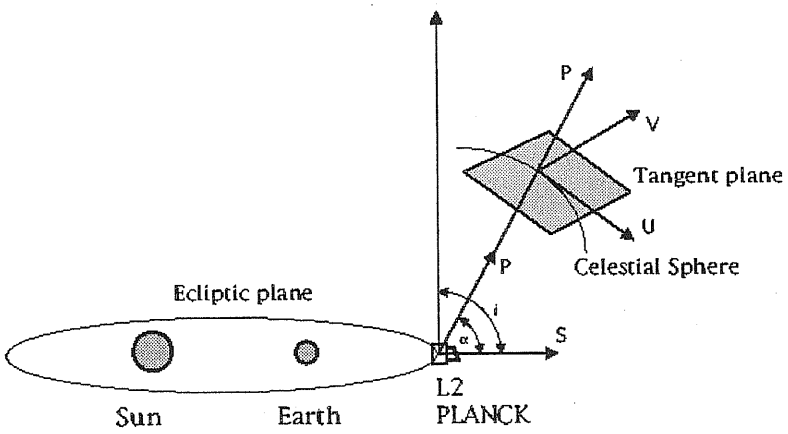

Figure 3-4: Schematic representation of PLANCK orbit and relevant input for the FS code

The performances of real hardware are usually far from optimum. In particular in Chapter 6 we will consider the issue of gain drifts in the LFI radiometer amplifiers which are the source of the so-called $1/f$ noise. Unfortunately these drifts have a typical time-scale smaller than the spin period and therefore they may be source of possible systematic artifacts in the data: if not properly minimized and removed they lead to stripes in the final maps due to the PLANCK scanning strategy. Through accurate simulations of the LFI radiometer performances we will address this issue and propose a removal technique. These results will provide an indication of the optimal scanning strategy with respect to the $1/f$ noise effect.

3.7 The Flight Simulator

In order to test the relevance of the previously mentioned systematic effects, a Flight Simulator code (hereafter FS) has been implemented. This code includes the main properties of the PLANCK payload: the bore-sight angle, the scanning strategy, the beam location on the focal plane. These are general properties and are valid for both LFI and HFI. In Fig. 3-4 i denotes the angle between the spin-axis $\mathbf{s}$ and the normal to the Ecliptic plane (in the simplest scanning strategy without spin-axis wobbling $i = 90°$); α is the bore-sight angle between spin-axis and pointing axis $\mathbf{p}$. Given total mission time, time for a given spin-axis position and spin-axis shift, FS code provides the directions for $\mathbf{s}$ and $\mathbf{p}$ during the mission: we always know where the pointing and spin-axis are pointing at.

In the celestial sphere we take the tangent plane in the $\mathbf{p}$ direction and, on this plane, define cartesian coordinates (x, y) identified by the versors $\mathbf{u}$ and $\mathbf{v}$. Here $\mathbf{u}$ is a versor pointing always the spin-axis while $\mathbf{v}$ is such that ($\mathbf{u}$,$\mathbf{v}$,$\mathbf{p}$) form a cartesian reference frame. On this plane the beam position is identified by its coordinates (x, y). Equivalently, beam position is found by two angles (the colatitude θ_B and the longitude ϕ_B) counted from the pointing axis and from the versor $\mathbf{u}$ clockwise. Other general code inputs are the FWHM (Full Width Half Maximum or resolution) for considered beams and the number

of samplings (which form a single integration) per single FWHM.

Considering LFI we have to properly model its performances. The nominal sensitivity is specified once given the system noise temperature, the bandwidth and integration time; the model $1/f$ noise behavior requires another input: the knee-frequency (further detailed description in Chapter 6).

The beam pattern is another key input. It is possible to use either simplified or optical simulated beam shapes. For each integration time the right position and orientation of the beam shape is considered in the FS code. Detailted description is in Chapter 4 and Chapter 5 which consider beam convolution for main beam distortions and stray-light analysis.

Chapter 4

Main Beam distortions for LFI beam patterns[1]

This chapter analyses the issue of main beam distortions for the Low Frequency Instrument. The telescope design and the present arrangement of the focal plane leave the LFI feed-horns at $\sim 2^\circ \div 5^\circ$ from the optical axis. Optical aberrations alter the beam pattern which is no more symmetric. Two are the major effects of main beam distortions: a degradation of the angular resolution, with respect to a beam placed in the center of the focal plane, and a lower sensitivity per resolution element. These can be regarded as orthogonal to each other in the space $\theta - \Delta T$ of angular resolution-temperature sensitivity to anisotropy (or equivalently in the $\ell - C_\ell$ space). The degraded angular resolution decreases the multipole order ℓ to which the experiment is sensitive, and the lower sensitivity makes the error bar on C_ℓ coefficients larger. The relevance of these effects on anisotropy measurements is the main concern of the accurate simulations, at 30 and 100 GHz, considered here. The effect of main beam distortions is quantified by the *rms* difference of sky temperatures observed by a distorted beam and a gaussian circular symmetric one, thus deriving an "effective" angular resolution.

Main beam distortions depend on the telescope size. Since the focal plane arrangement is almost fixed, the only way to make the off-axis beam patterns "closer" to the optical axis and then less distorted, within the current telescope configuration, is to enlarge the size of the telescope or to find a telescope design with a better response over a larger focal surface.

This chapter is organized as follows: §4.1 summarizes the general concept of convolution and presents the approximated main beam shape used for some of our simulations; the microwave sky model is in §4.2 while §4.3 presents results either for pure CMB sky (§4.3.1) either including galactic emission (§4.3.2). Optical simulated beam shapes at 100 GHz are considered in §4.4 and the loss in capability of extracting cosmological parameters is in §4.4.1. Conclusions are reported in §4.5.

[1]Partially based on C. Burigana, D. Maino *et al.*, *A&ASS*, **130**, 551 (1998) and on D. Maino *et al.*, ISAS Internal Report, in preparation

4.1 Sky convolution and beam shape

In order to evaluate the effect of main beam distortions a real/simulated beam response function together with a realistic model of microwave sky emission is required. The sky temperature observed by the main beam of an antenna with a normalized beam pattern $P_n(\theta,\phi)$ is

$$T_{\rm obs}(\theta,\phi) = \frac{\int_{\Omega_{\rm M}} P_n(\theta,\phi)T(\theta,\phi)d\Omega}{\int_{\Omega_{\rm M}} P_n(\theta,\phi)d\Omega}, \tag{4.1}$$

where $T(\theta,\phi)$ is the real sky temperature in the sky position (θ,ϕ) and $\Omega_{\rm M}$ is the main beam solid angle. In order to compute the antenna pattern for PLANCK-LFI feed-horns, the proper horn response coupled with the adopted telescope design have to be considered. An ideal non-imaging telescope converts the plane wave entering on the telescope aperture, in a spherical wave centered at the focal point. A perfect feed transforms the free-space spherical wave into a guided-wave propagating through the horn to the detector chain without losses. This condition is nearly satisfied with a parabolic shaped reflector coupled with a corrugated feed, provided that the phase center of the feed is placed at the parabola focus. In general, based on the reciprocy theorem of the electromagnetic field, the antenna response at the far-field region is the Fourier transform of the electric field on the antenna aperture, seen as a radiating aperture. Considering an ideal telescope (*i.e.* parabolic) and a feed-horn perfectly on-axis (*i.e.* on the parabola focus), horn pattern is transferred to the aperture plane and thus on the antenna far-field beam pattern, without introducing variations on the optical path or, equivalently, without any phase delay. Under this condition the pattern shows a symmetric response which is of course the best case. However considering feed-horns displaced from the optical axis, the field on the aperture shows an Optical Path Difference (OPD) or different phases, and consequently beam distortions rise, due to the combination of the field not perfectly phased. Depending on the phases distribution the resulting distortions are called: coma, spherical aberrations and astigmatism.

This can be easily generalized to the dual mirror PLANCK-like telescope in which each reflector may introduce phase errors and then beam distortions. The usual way to reduce them would be to place the feed-horns close to the optical axis. However, since the focal plane arrangement is almost fixed, it is not possible to gain much in this direction. It is possible to study different telescope designs that minimize the OPD on a large region of the focal plane thus reducing beam distortions.

As a first step a beam pattern which is gaussian but with an elliptical section is considered. This is a simplification but not far from reality: optical simulations [81] show that main beam distortions for off-axis beams result in an elliptical main beam shape with increasing complexity in side-lobes. In this way it is possible to derive orders of magnitude of distortion effect and its dependence upon basic parameters: FWHM, observing frequency, telescope aperture and beam location on the focal plane. Here the elliptical beam is located along the optical axis. This further simplification does not alter our final conclusions but speeds up geometrical calculations in FS code. The beam pattern at a given point (x,y) on the $\mathbf{u}-\mathbf{v}$ plane (see §3.6) then reads:

$$P_n(x,y) = \exp\left[-\frac{1}{2}\left[\left(\frac{x}{\sigma_x}\right)^2 + \left(\frac{y}{\sigma_y}\right)^2\right]\right]. \tag{4.2}$$

The amount of main beam distortion is parametrized by the ratio r between the major, σ_x, and minor, σ_y, axis of the ellipse with respect to a case of a pure symmetric beam with $\sigma' = \sigma'_x = \sigma'_y = \sqrt{\sigma_x \sigma_y}$. Here the major axis is along the x axis but different orientations do not alter our results. Since main beam distortions are the main concern of this chapter, the sky signal is integrated up to 3σ level of the beam pattern *i.e.* $(x/\sigma_x)^2 + (y/\sigma_y)^2 = 9$ which corresponds to a level of ~ -20 dB.

4.2 Simulated microwave sky

In order to evaluate the impact of main beam distortions on LFI observations, a realistic sky has to be considered. This will include CMB anisotropy and a model of galactic and extra-galactic emission. Several models will be considered in this thesis using the present knowledge reported in §2.4 and 2.6. The worst case scenario is always considered with respect to the systematic effect under study. The *COBE*-Cube pixelization scheme is used for mapping microwave sky models. Synthetic microwave sky at 30 and 100 GHz, including CMB fluctuations and galactic emission which sums up synchrotron and dust emission, are here considered.

4.2.1 CMB fluctuations

We expand CMB anisotropy in spherical harmonics as in Eq.(2.13). The spherical harmonic functions $Y_{\ell m}(\theta, \phi)$ are the product of two functions which encode the θ and ϕ dependence separately: the Legendre polynomials and a phase factor $e^{im\phi}$. Following Burigana *et al.*[19] a modified version of the Legendre polynomials is introduced:

$$p_\ell^m(\mu) = \sqrt{\frac{(\ell - m)!}{(\ell + m)!}} P_\ell^m(\mu)\,, \tag{4.3}$$

where $\mu = \cos(\theta)$. With this modification and the condition of reality for CMB fluctuations, we obtain:

$$\begin{aligned} \frac{\Delta T}{T}(\theta, \phi) &= \sum_{\ell=2}^{\ell_{\max}} \sqrt{\frac{2\ell + 1}{4\pi}} p_\ell^0(\mu) \Re(a_{\ell 0}) \\ &+ \sum_{m=1}^{\ell_{\max}} \sum_{\ell=\max(2,m)}^{\ell_{\max}} 2\sqrt{\frac{2\ell + 1}{4\pi}} p_\ell^m(\mu) \\ &\times [\Re(a_{\ell m})\cos(m\phi) - \Im(a_{\ell m})\sin(\mathrm{m}\phi)]\,. \end{aligned} \tag{4.4}$$

Since a real convolution between sky signal and beam pattern is performed, the highest possible sky resolution has to be achieved and therefore a large number of evaluations of Eq.(4.4) are required. The adopted pixelization, although does not allow the use of FFT (Fast Fourier Transform) for fast computation of CMB sky maps, has some useful symmetry properties which decrease computational time by a factor of ~ 4. We chose to generate map at $19'$, $10'$ and $5'$ of resolution (pixel size) which seems to be appropriate for our purpose considered the $33'$ and the $10'$ resolution at 30 and 100 GHz respectively.

4.2.2 Galaxy emission

Since free-free emission never dominates microwave sky signal (see §2.6), our galactic synthetic model includes only synchrotron and dust emission. However the exclusions of free-free emission minimally affects final results. Our sky map database includes two full-sky maps: the Haslam map, which is a useful spatial template for synchrotron emission, and *COBE* DIRBE map at 240 μm which traces dust emission. Synchrotron is modelled by a simple power law with a spectral index $\beta_{\rm sync} = 2.8$; dust emission is described by a modified blackbody law $I_\nu \propto \nu^\alpha B_\nu(T)$ where α (typical values between 1.5-2) is the dust emissivity and $B_\nu(T)$ is the planck function at frequency ν and dust temperature T ($\sim$ 18 K).

Both the Haslam and *COBE* DIRBE maps lack the proper angular resolution to match PLANCK specifications. For realistic simulations of LFI observations we have to artificially extend their angular resolution according to present knowledge about synchrotron and dust spatial distribution. A simple heuristic approach, which is obviously a first but reasonable guess, is considered. Firstly the angular resolution of sky maps (Haslam and DIRBE) is increased by dividing each original pixel into smaller pixels of 5′ and assign in each smaller pixel the same temperature of the larger one. Now we want to add fluctuations to this constant field. How can we do it? We simply calculated from the original map the *rms* on a given angular scale (namely 2.6°); build a suitable number of 20° × 20° patches with fluctuations with an angular power spectrum $C_\ell \propto \ell^{-\beta}$ (both $\beta = 2$ and 3 are considered) up to 5′ angular scale. We randomly cover the *rms* sky with these patches and re-scale each patch requiring that the *rms* on the 2.6° scale in the extended map has to be the same found in the original map; in this way we "normalize" our extended map. We finally add this fluctuation field to the extended sky.

4.3 Beam tests results

The convolution of the sky with beam response function is performed assuming that the telescope points always in the same direction during a given integration time: this is in general not true although this approximation does not alter our results. Furthermore we want to evaluate the impact due to main beam distortions in a way which does not depend upon scanning strategy but only on optical properties of the LFI instrument.

The beam integration is performed using 2-dimensional gaussian quadrature with a grid of 48×48 points. Sky maps are then interpolated using bilinear interpolation in order to have sky temperature at each grid point. Maps at 5′ resolution will have $\sim$ 50 pixels per FWHM at 30 GHz (33′) and $\sim$ 6 at 100 GHz (10′). Our integration accuracy depends also on the map resolution and we evaluate quantitatively this dependence.

We derive the impact of main beam distortions with a simple estimator which is the *rms* of the difference between temperature observed by an elliptical beam and that from a circular one. The *rms* is expressed in thermodynamic units which are the usual units for CMB results and which do not depend upon frequency.

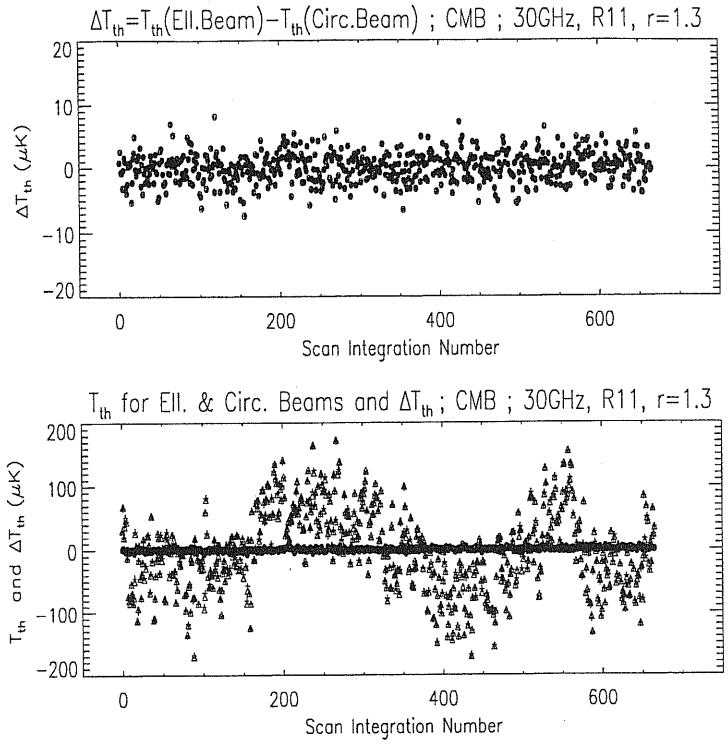

Figure 4-1: Top panel: differences between temperatures observed by an elliptical and circular beam for a typical scan. Bottom panel: temperature observed by an elliptical (triangles) and circular (crosses) beam and their difference (circles) for a given scan.

4.3.1 Test with CMB signal only

In order to obtain results valid for low foreground regions, where most of the cosmological informations will be extracted, a pure CMB sky neglecting foreground emissions is considered. The CMB anisotropies are modelled assuming a standard CDM model with baryon content $\Omega_B = 0.06$, Hubble constant $h = 0.5$, no re-ionization and 24% of mass in Helium. Test assuming different cosmologies (ΛCDM with $\Omega_\Lambda = 0.7$ and MDM with $\Omega_{\rm hot} = 0.3$) yield nearly the same results of the standard CDM. Maps are pixelized at $5'$ but results dependence upon pixel size is explored.

Fig. 4-1 and 4-2 report results at 30 and 100 GHz respectively: the upper panels show differences in scan circle temperatures between elliptical and circular beams; lower panels show the same differences as before compared with absolute temperature observed by the two beams. Even with large temperature variations (quadrupole waves) temperature differences remain almost constant along a scan circle. Table 4.1 summarizes results with different beam pattern, distortion parameters r and map pixel size. Last column in Table 4.1 reports the numerical error in the evaluation of the *rms* for a typical scan using different integration grids: 96×96 grid points instead of 48×48. Test # 7 shows that for maps with lower resolution, the effect of main beam distortions is reduced by the smoothing of the CMB field. There is a simple geometrical explanation for these results: signal coming from different parts in the sky (within the main beam solid angle) as observed by beam with different shapes, becomes more and more important as the angular resolution (FWHM) increases (see results at 30 and 100 GHz for the same values for r) and/or the distortion parameter increases (see results at 30 and 100 GHz separately).

We search for an analytical description of the previous results and factorize the depen-

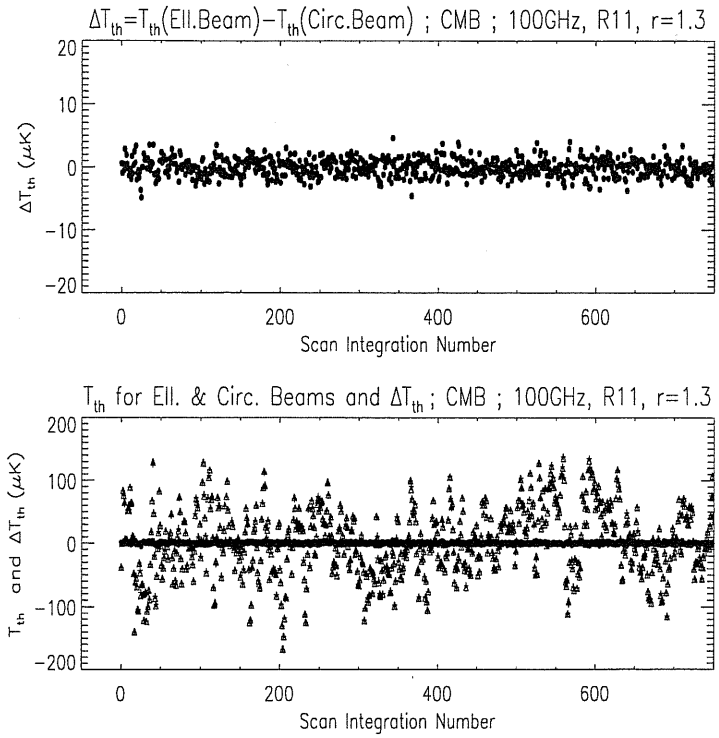

Figure 4-2: The same as in Fig. 4-1 but at 100 GHz.

Test #	Freq. [GHz]	FWHM [′]	Pixel size [′]	r	rms [μK]	Δrms [μK]
1	30	30	5	1.1	0.834	0.16
2	30	30	5	1.3	2.27	0.16
3	30	30	5	1.8	5.09	0.16
4	100	10	5	1.1	0.506	0.10
5	100	10	5	1.3	1.38	0.10
6	100	10	5	1.8	3.19	0.10
7	30	30	19	1.3	1.39	

Table 4.1: Values for rms of $(T_{\rm ell} - T_{\rm circ})$

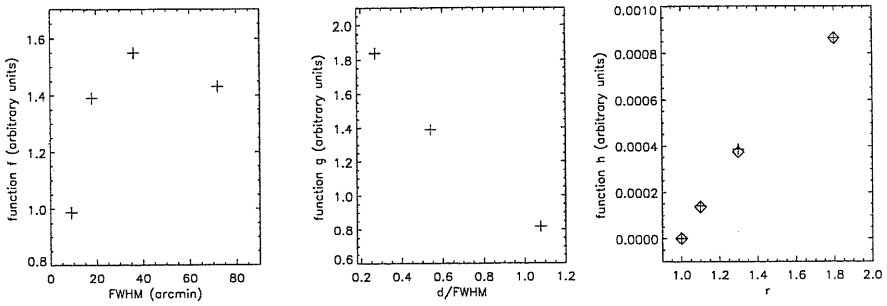

Figure 4-3: Dependence of rms upon (from left to right): FWHM, map resolution and distortion parameter r (crosses: tests at 30 GHz; daimonds: tests at 100 GHz).

dence of the rms upon FWHM, distortion parameter r and map resolution, quantified by pixel size d. This means to search for an expression of the form:

$$rms = f(\mathrm{FWHM}) \times g(d) \times h(r)\,. \tag{4.5}$$

We perform several simulations in which we vary one of these parameters while keeping the others fixed. A quadratic dependence of rms upon either FWHM either r is found; a simple linear law holds for map resolution. These functions are reported in Fig. 4-3. The final expression reads:

$$\begin{aligned} rms \;&\simeq\; 6.43 \times 10^{-4}\mu\mathrm{K}[-(r-1)^2 + 2.26(r-1)] \\ &\times\; [(-\mathrm{d/FWHM}) + 1.72] \\ &\times\; [-\mathrm{FWHM}^2 + 96.0\,\mathrm{FWHM} + 1800.]\,. \end{aligned} \tag{4.6}$$

This analytical approximation works quite well for FWHM $\lesssim 1°$: typical errors are of the order of $\sim 0.25\mu$K and always less than 0.7μK

In computing the observed temperature for each integration along a scan-circle, the beam pattern is supposed not to change its orientation within an integration time. This is not true in general since within an integration time PLANCK telescope continuously changes its pointing direction. In the Phase A study of the PLANCK mission the sampling scheme considered 3 samplings per FWHM at each frequency resulting in total number of samplings different for each frequency for the different FWHM. Assuming this sampling scheme we assign to each of the 3 samplings a different orientation of the telescope thus roughly simulating telescope motion. The average over the 3 samplings is computed for symmetric and elliptical beam and the rms of the difference between the two is derived. For a pure CMB microwave sky, with a distortion parameter $r = 1.3$ at 30 GHz (see Test # 2), an $rms = 1.85\mu$K is obtained which has to be compared with the previous $rms = 2.27\mu$K without "telescope motion". Oversampling can not be easily used to further reduce main beam distortions: this was intuitively expected since within an integration time the telescope orientation does not change significatively.

4.3.2 Tests including Galaxy signal

The above results hold in absence of galactic fluctuations and we expect the inclusion of galactic emission in a more realistic synthetic sky will play an important role especially at

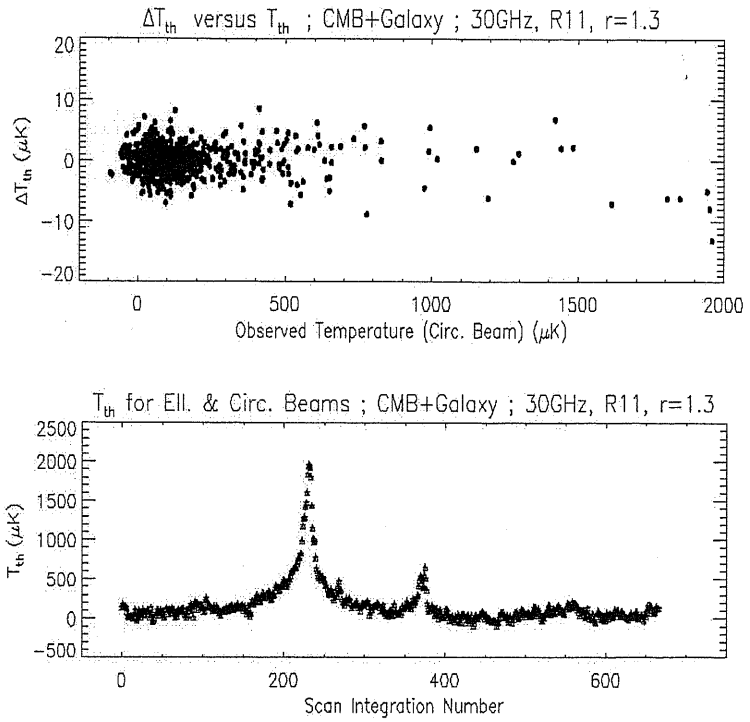

Figure 4-4: Top panel: differences between temperature as observed by an elliptical and a circular beam for a typical scan as a function of the observed temperature in the circular beam. Bottom panel: absolute temperature observed by the elliptical (triangles) and circular (crosses) beam

30 GHz where galactic contamination is larger. Following §4.2.2 microwave sky emission is evaluated at 30 and 100 GHz. Fig. 4-4 shows results at 30 GHz: upper panel reports temperature differences between an elliptical and a circular beam as a function of the circular beam temperature; lower panel shows the absolute temperature observed by the two beams. With the same parameters of Test # 2 we obtain an $rms = 2.49\mu$K which is not larger than the pure CMB case ($rms = 2.27\mu$K). However when computing the rms only for observed temperatures larger than 200μK, an $rms = 3.22\mu$K results. We compute the behaviour of rms as a function of the galactic latitude. Values of rms every 3.5° in latitude are shown in Fig. 4-5: rms is not large where galactic signal is low; on the contrary near the galactic plane ($|b| \lesssim 5°$) rms is $2 \div 3$ times larger because of larger galactic signal and fluctuations. This situation does not depend upon the chosen model for small angular scales galactic fluctuations. At 100 GHz a similar effect is not visible due to the relative lower amplitude of galactic emission at this frequency with respect to 30 GHz.

4.4 "Real" beam patterns

Previous tests with elliptical beams are useful for orders of magnitude evaluations of the effect of main beam distortions and for deriving simple analytical dependence from basic

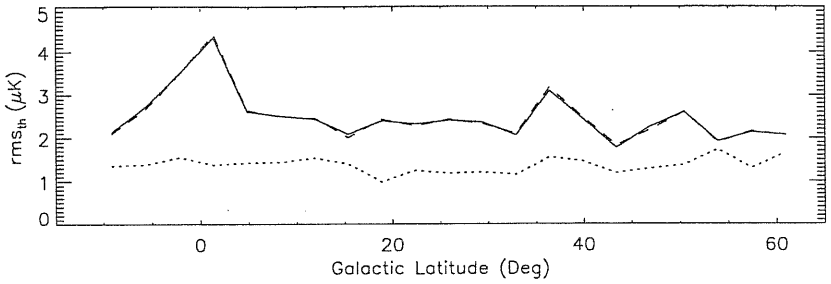

Figure 4-5: *rms* as a function of the galactic latitude at 30 GHz (upper curves) and 100 GHz (dotted line). Solid line refers to a slope $\beta = 2$ for galactic fluctuations while dashed line is for $\beta = 3$. The adopted r is 1.3

parameters. However "real" beam patterns have to be considered in order to obtain a more precise and realistic evaluation of this systematic effect. Villa *et al.*[121], using a software based on calculation by Sletten [109] computed "real" beam shapes for all the 17 LFI 100 GHz feed-horns (see Fig. 4-6, left panel) for three different values of the primary mirror aperture of the PLANCK telescope. They considered 1.3, 1.55 and 1.75 meter aperture telescopes: a typical beam shape for the 1.3 m telescope is shown in Fig. 4-6 (right panel): note the clearly not elliptical distortion of main beam in the -20 dB contour level. The primary mirror aperture, feed antenna pattern and feed location on the focal plane determine the angular resolution achievable. It is worth reminding that the LFI feed at 100 GHz should have $10'$ of nominal resolution in order to fullfil LFI cosmological goals.

We consider all the LFI 100 GHz feed-horns in their present allocations on the focal plane and a pure CMB standard CDM sky: previous results support that at 100 GHz small galactic contamination at high galactic latitudes is expected. An effective angular resolution is derived for each feed-horn for the 3 primary mirror apertures. In order to evaluate the effective angular resolution, the CMB sky is convolved with "real" beam patterns truncated at 1° from the beam center, and with a set of gaussian beams with FWHM ranging from $6'$ to $17'$ at $1'$ step. Considering the gaussian beams only and computing the differences and relative *rms* between temperatures observed by one beam and all the others, we found that an $rms \simeq 1.5\mu$K results for two gaussian beam with $1'$ FWHM difference. We then compute the differences and *rms* between temperatures observed by "real" beams and by the gaussian ones: the FWHM of the gaussian beam that produces the smallest sky temperature *rms* with the "real" distorted beam, is taken to be the effective angular resolution W_e of the "real" beam pattern. Results are synthetically reported in Table 4.2. For each feed-horn and primary mirror aperture the effective resolution W_e and corresponding *rms* is computed. This *rms* quantifies the typical signal difference between distorted and gaussian equivalent beam: the additional noise introduces by main beam distortions is between $2 \div 3\mu$K for 100 GHz beams located at $\simeq 2.8^\circ$ from the optical axis. It is interesting to compare these results with those obtained using elliptical gaussian beams showing how "real" beam patterns are far from being simply gaussians and elliptical. Fig. 4-7 shows our results as contour plots of constant angular

D →	1.3m		1.55m		1.75m		D →	1.3m		1.55m		1.75m	
Feed	W_e	σ_{th}	W_e	σ_{th}	W_e	σ_{th}	Feed	W_e	σ_{th}	W_e	σ_{th}	W_e	σ_{th}
1	12.00	2.10	10.00	1.70	8.90	2.60							
2 & 17	12.15	3.15	10.25	2.75	9.00	1.90	3 & 16	12.35	2.70	10.45	2.10	9.20	2.10
4 & 15	13.00	2.30	11.00	1.45	9.80	2.70	5 & 14	12.90	2.40	10.90	2.80	9.55	1.75
6 & 13	13.15	2.00	11.00	2.00	9.70	1.90	7 & 12	13.40	2.05	11.20	2.35	9.85	2.00
8 & 11	13.90	1.15	11.65	1.95	10.25	1.85	9 & 10	14.20	2.05	12.05	1.40	10.70	1.70

Table 4.2: Beam properties at 100 GHz for telescopes of different aperture: W_e (in arcmin) and values (in μK) of the thermodynamic temperature *rms* differences, σ_{th}, measured by "true" beams and corresponding gaussian beams. Results from pairs of beams located at the same **u** and $|\mathbf{v}|$ have been averaged. By averaging over all the feeds we have: $\langle W_e \rangle = 13.1', 11.0', 9.7'$ and $\langle \sigma_{th} \rangle = 2.2, 2.1, 2.0 \mu$K respectively for the 1.3, 1.55, 1.75 m aperture telescopes.

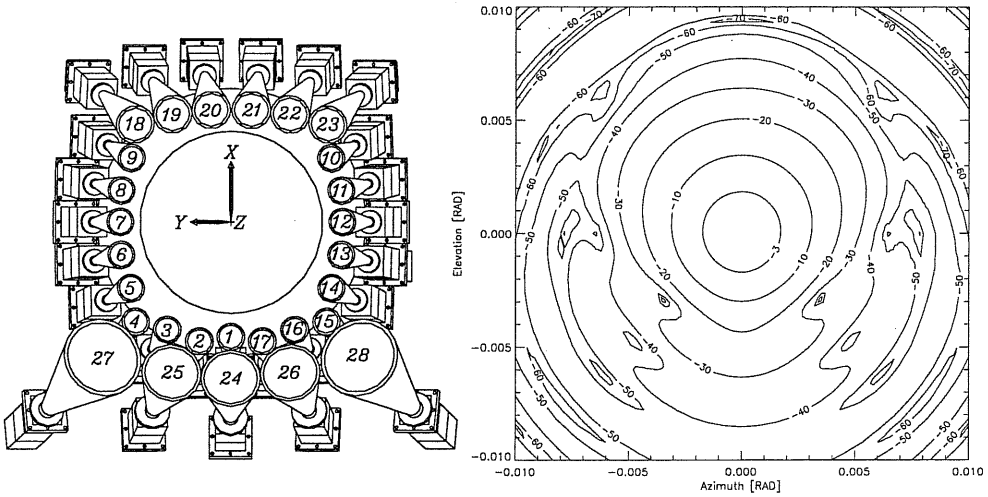

Figure 4-6: Left panel: LFI focal plane assembly. Feeds from 1-17 are at 100 GHz, from 18-23 at 70 GHz, from 24-26 at 44 GHz and 28 and 29 at 30 GHz. Right panel: Typical beam pattern at 100 GHz for feed # 1 (From Villa *et al.*[121])

resolution for the 1.3 and 1.75 meter telescopes at 100 GHz. The feed-position of all the LFI frequencies is indicated by the filled color circles: note that the whole set of 100 GHz array is located near the contour level of 13′ and 10′ resolution for the 1.3 and 1.75 meter respectively. It is evident that with the 1.3 meter telescope (the PLANCK Phase A telescope) the 100 GHz feed-horns, with the present symmetric configuration of the focal plane, are far from the nominal 10′ of resolution thus possibly compromising LFI cosmological goals. A possible solution would be to aggressively illuminate the primary mirror to gain better angular resolution. On the other hand this would increase the level of sidelobes introducing possible spurious signals which have to be properly considered.

Another point is the large dispersions of W_e values: from 12′ to 14.2′ for the 1.3 meter, and from 10.7′ and 8.9′ for the 1.75 meter. This dispersion does not disappear enlarging the telescope aperture. A simple but crucial result is that signal observed by two beams looking at the same sky region *can not be averaged in a simple way* since each beam is distorted in a particular way peculiar of its position on the focal plane. This situation is summarized in Fig. 4-8 where the distribution histogram of the differences between the signal observed by all the 17 LFI 100 GHz feed-horns for a typical scan circle, is

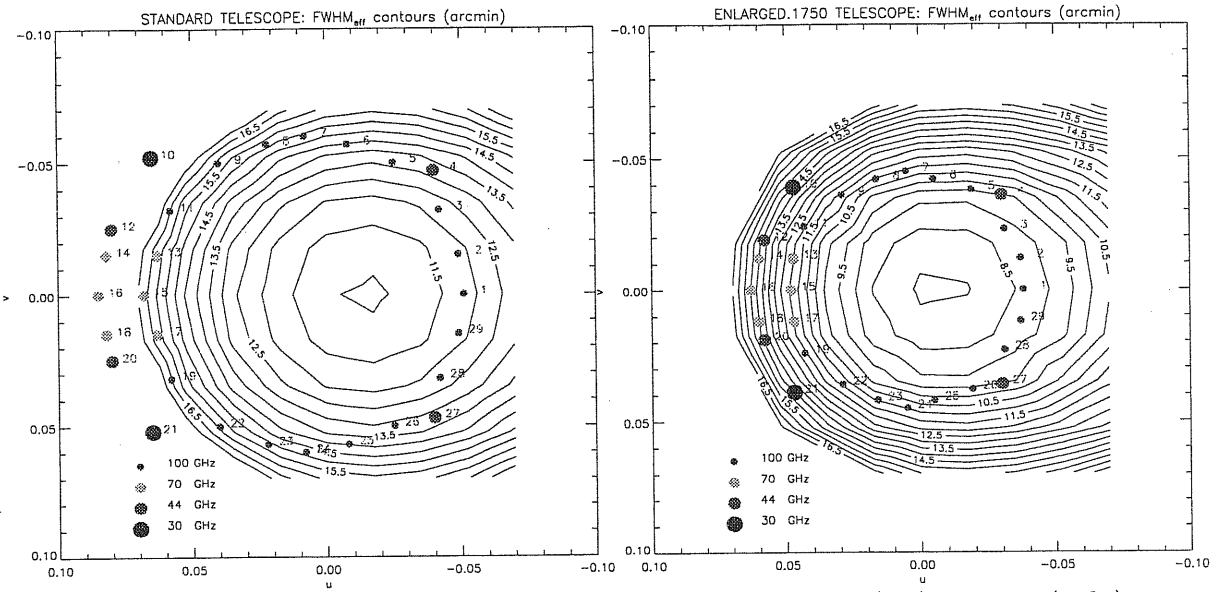

Figure 4-7: Contour levels of constant angular resolution for the 1.3 (left) and 1.75 (right) meter telescopes computed at 100 GHz. Feed-horn position at LFI frequency is indicated by the filled colored circles in the $\mathbf{u} - \mathbf{v}$ plane (units of radians)

reported (solid line). Together are also shown temperature differences from two subsets of 100 GHz feed-horns: one subset made by those feed-horns whose W_e are quite similar (differences $\lesssim 0.2'$, dotted lines), another subset where W_e is quite different ($\sim 2'$, dashed lines). As shown this effect can not be reduced enlarging the primary mirror aperture. Unless another focal plane assembly is possible placing the 100 GHz feed-horns closer to the optical axis, other solutions have to be found. Preliminary results from Mandolesi *et al.*[76] for an Aplanatic Gregorian off-axis telescope are promising: for the same primary mirror aperture of the standard Gregorian telescope, the aplanatic telescope yields better and regular beam patterns and less spread in W_e values. Of course the other possibility will be certaintely to scrub this systematic effects in data reduction and therefore suitable algorithms are under study.

4.5 Main beam distortions and cosmological parameters

The main beam distortion affect the final angular resolution, which enters in the expression for errors on C_ℓ Eq.(2.20). We want to evaluate directly the main beam distortion effects on LFI science and in particular on the estimation of cosmological parameters. Of course a detailed study should require the combined analysis of all frequency channels taking into account foreground contamination as well as an accurate quantification of the capabilities the components separation techniques (Wiener filter and/or MEM (*e.g.* [1, 16, 54])). However the 100 GHz channel is marginally affected by foreground contaminations and pure CMB data at this frequency will be used as a guideline for following discussion.

Firstly a simple estimation of the increased uncertainty on C_ℓ due to decreased angular resolution is derived. At very high $\ell \simeq 800 \div 1000$, the C_ℓ uncertainty is dominated by

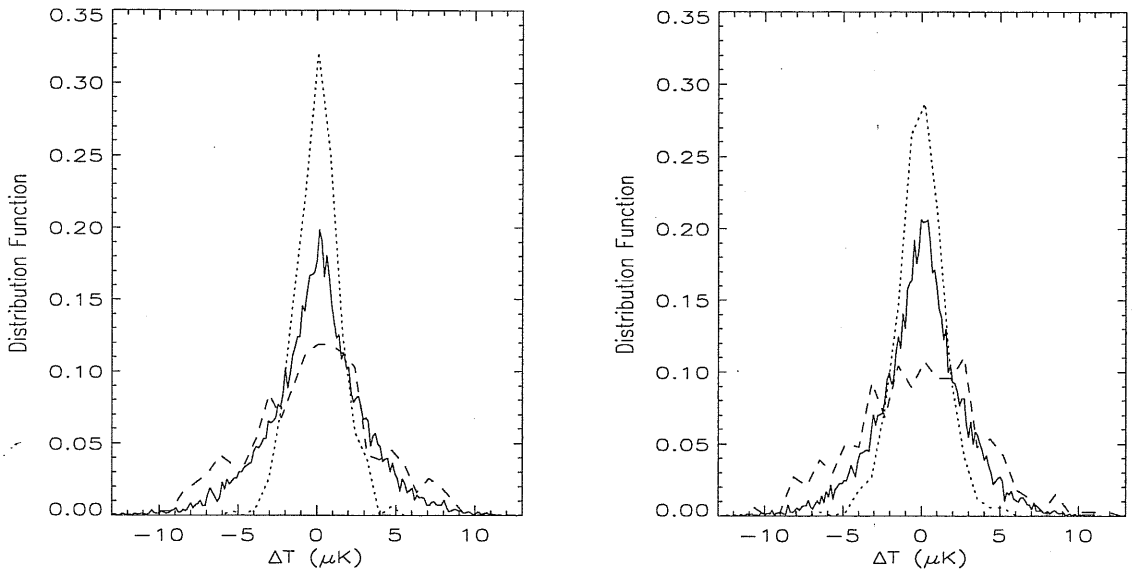

Figure 4-8: Distribution functions of differences between signals measured by LFI 100 GHz feed horns and two subsets of them (see text) for the 1.3 meter (left panel) and 1.75 meter (right) telescope.

instrumental noise: it is possible to re-write Eq.(2.20) as:

$$\frac{\Delta C_\ell}{C_\ell} \simeq \sqrt{\frac{4\pi}{\Omega_{\rm obs}}}\sqrt{\frac{2}{2\ell+1}}\left[\frac{4\pi\sigma^2}{B_\ell^2 C_\ell N_{\rm pix}}\right], \tag{4.7}$$

where $B_\ell^2 = \exp[-\ell(\ell+1)W_e^2/8\ln 2]$ and W_e is the effective angular resolution as derived in §4.4. The ratio of ΔC_ℓ for two experiments with the same noise per pixel σ but with different resolution $W_{e,1}$ and $W_{e,2}$ reads:

$$\frac{\Delta C_\ell|_1}{\Delta C_\ell|_2} \simeq \exp[-\ell(\ell+1)(W_{e,2}^2 - W_{e,1}^2)/8\ln 2]\,. \tag{4.8}$$

The averaged angular resolutions at 100 GHz for the 1.3m and 1.75m telescope are $13'$ and $9.7'$ respectively. The ratio in Eq.(4.8)is then 2.1, 3.2, 5.5, and 14 at $\ell = 800, 1000, 1200$ and 1500 respectively. The degradation on C_ℓ accuracy, especially at large ℓ, is quite significant and the 1.3m Phase A telescope is not satisfactory in this respect.

The larger the errors on C_ℓ, the larger the errors on extracted cosmological parameters. The effect would be particularly relevant for those parameters producing features in C_ℓ at large ℓ which are the most affected by angular resolution degradation. A complete χ^2 fit or Likelihood analysis should be done. However simple estimation of errors on cosmological parameters could be derived exploiting the Fisher Information Matrix formalism (see Appendix A for further details). This approach works in idealized conditions of no foreground contaminations. As before the 100 GHz channel without foregrounds will be the guideline for the analysis. The Fisher Matrix needs a fiducial CMB anisotropy model. An open CDM model, with Hubble constant $h = 0.65$, matter content $\Omega_m = 0.4$, baryon content

Quantity	1.3 m	1.75 m
$\Delta \ln\ h$	0.0330	0.0217
$\Delta \ln\ \Omega_K$	0.0377	0.0232
$\Delta\Omega_\Lambda$	0.0448	0.0271
$\Delta \ln\ \Omega_b h^2$	0.0134	0.0122
$\Delta\Omega_m$	0.0674	0.0410
$\Delta \ln\ n_S$	0.0095	0.0087
$\Delta \ln\ \tau$	0.8074	0.7870
$\Delta \ln\ C_2$	0.0832	0.0809

Table 4.3: Uncertainties on cosmological parameters versus telescope aperture. The chosen model is and OCDM model with $h = 0.65, \Omega_m = 0.4, \Omega_b = 0.06, \tau = 0.05, n_S = 1$. The fraction of the sky is $f_{sky} = 0.65$

$\Omega_B = 0.06$, no cosmological constant, re-ionization optical depth $\tau = 0.05$ and primordial spectral index $n = 1$, is adopted. We take only a fraction of the sky $f_{\rm sky} = 0.65$ when computing C_ℓ uncertainties. Results are in Table 4.3 for the 1.3m and 1.75m telescopes. The 1.3m telescope which provides an averaged angular resolution of $13'$ at 100 GHz, yields errors which are $\simeq$40% larger than for the 1.75m telescope which on the contrary provides $9.7'$ of mean angular resolution. The effect is particularly evident for those parameters which show their signature at large ℓ (*e.g.* the curvature parameter $\Omega_K = 1 - \Omega_m - \Omega_\Lambda$ and Ω_m). Therefore a significant degradation at 100 GHz results. Furthermore this is an idealized case with no foregound contaminations which certaintely will further degrade the cosmological parameters errors when included.

4.6 Conclusions

Accurate simulations of the main beam distortion effect with pure CMB sky and including galactic emission, yield an additional noise with *rms* of few μK and a degredation in the angular resolution is introduced. This extra noise is not large compared to the average sensitivity. However because of the adopted PLANCK scanning strategy, some sky areas will be observed several times yielding a better sensitivity than the average. These regions are close to Ecliptic polar caps and in a $25^\circ \times 25^\circ$ region around them, the sensitivity is ~ 5 better than the average. Furthermore this effect does not take advantage of the scanning strategy since repeated observations of the same sky regions are pratically observed with the same main beam orientation in the $\mathbf{u} - \mathbf{v}$ plane except for regions around the Ecliptic caps. A part for these regions, the effect of main beam distortions is more systematic than statistic in origin.

Simulations assuming simple elliptical gaussian main beam patterns indicate that for the same distortion parameter r, the distortion effect is larger at lower frequency because of the larger beam width. This fact would suggest to place low frequency feed-horns close to the optical axis where aberrations are smaller. However optical simulations [81] show that for fixed distance from the optical axis, distortions are larger at higher frequencies *i.e.* the distortion parameter r is larger. This fact would on the contrary suggest to

place high frequency channels close to the optical axis. Our present knowledge of the effect, its dependence upon FWHM and r, favor the second arrengement. Furthermore the more crucial role of the high frequency channels for LFI science, drives to put the 70 and 100 GHz closer to the optical axis. Nonetheless lower frequencies are extremely important controlling and monitoring foreground emissions and main beam distortions have to be reduced to the minimum level for a correct estimation and meaningful separation of these emissions. In this respect larger primary mirror aperture and/or better optical configurations (aplanatic telescope) have to be considered.

More realistic simulations have been performed using "real" optical simulated beam patters. At 100 GHz for the 1.75m telescope the beam pattern is quite elliptical with $r \simeq 1.2$ but is not gaussian: structures at significant level are also present in the sidelobes and their contribution could be important. The effective angular resolution W_e, derived for all the 17 LFI 100 GHz feed-horns for the 1.3m telescope, yields to the conclusion that this telescope is far from being satisfactory, not allowing the $10'$ of angular resolution at 100 GHz and comprimising the cosmological goals of LFI. It is possible to gain better angular resolution with this aperture with an over-illumination (low edge-taper) of the primary thus increasing the level of sidelobes [75]. This issue will be carfully addressed in Chapter 5.

The choice of a 1.75m telescope seems to satisfy both the requirements on angular resolution and on side-lobes signal rejection. It is possible to under-illuminate a larger primary mirror without substantially decreasing the angular resolution but significantely lowering the side-lobes. Fig. 4-7 shows the angular resolution contours at 100 GHz computed with an edge-taper of -30 dB, a level which allows a good suppresion of side-lobes. The analysis of the effect of main beam distortions directly on CMB science also shown the significant degradation of LFI capabilities for the 1.3 meter telescope with respect a larger telescope.

These results have to be regarded as lower limits since the idealized case considered: all the other possible systematic effects are not considered as if they were exactely known and properly correct. A degradation of these results would be possible when a comprehensive simulations will be performed. However these results have been extremely important and have been the basis for a trade-off with ESA in the definition of the PLANCK telescope yielding a 1.55m aperture as present baseline. It would be possible to further optimize both telescope design and primary mirror aperture in the PLANCK Phase B.

Chapter 5

Galactic stray-light[1]

This chapter analyses the issue of stray-light contaminations in LFI observations. Stray-light is defined as the radiation that enters the detector out of the main beam pattern. In principle, it is difficult to separate it from the main beam signal. The source of stray-light may be both internal (emission from telescope and satellite itself), and external *i.e.* astrophysical in origin. The level of stray-light depends on the full beam pattern and, for external stray-light, on its orientation with respect astrophysical sources. The requirement on rejection of this un-wanted radiation depends not only on the telescope design and aperture, as for main beam distortions, but on the entire optical system which includes solar, panels, shield, thermal stability, assembly on the focal plane and orbit selection. Analysis of optical simulations yields the conclusion that features of the antenna pattern at large angles are mainly produces by diffraction and scattering from the edges of mirrors and supporting structures.

In order to achieve the proper sensitivity per resolution element, strong requirements on rejection of these signals are needed: for the Sun a rejection ≈ -91 dB is required, for the Earth ≈ -78 dB, for the Moon ≈ -71 dB and for the galactic plane ≈ -65 dB. As for the Sun , the effect of solar radiation are minimal with an anti-Sun spin-axis. Low Earth Orbit (like the one of *COBE*) are not suitable because of stray-light and thermal modulation which prevent to reach temperature lower than 100 K in the focal plane. The optical orbit with respect thermal and stray-;light considerations is a tight Lissajous orbit around the Lagrangian L_2 point of the Earth-Sun system. In this way Sun, Earth and Moon are always behind the spacecraft and, in the simplest scanning strategy with spin-axis always on the Ecliptic plane, their position relative to the spacecraft is constant. This would allows stable thermal environment and stray-light rejection.

One of the major contribution to stray-light signal is galactic plane which is continuously observed by the LFI beams. The effect is expected to be larger at low LFI frequencies since the overall larger galactic emission. It is important to estimate not only the expected level of stray-light signal, but also its spatial distribution *i.e.* where stray-light signal is re-projected on the sky and then the possible effect on LFI science. Accurate simulations have been performed including an optical simulated full beam pattern at 30 GHz in the FS code.

This chapter is organized as follows: §5.1 describes the full antenna beam pattern

[1]Partially based on C. Burigana & D. Maino, *A&ASS* submitted

and the reference frames used in the simulations; §5.2 gives order-of-magnitude estimation of the level of the stray-light signal while in §5.3 the convolution code is presented and tested. Main results are presented in §5.4 in terms of data streams and of stray-light maps. Conclusions are reported in §5.5.

5.1 Simulated beam pattern

In order to evaluate the effect of stray-light, an antenna full pattern is required together with a FS code which properly re-projects stray-light signal in the sky according to the scanning strategy. The reference frame considered is the one described in §3.7: the telescope axis define the z-axis while $\mathbf{u}$ and $\mathbf{v}$ respectively define the x and y axes in the telescope reference frame. Each beam position is identified by means of its $\mathbf{v_B}$ in the (x, y, z) frame or by the colatitude and longitude (θ_B, ϕ_B).

The ESA team provided us the full antenna pattern at 30 GHz [30]. This is computed considering the physical theory of diffraction, propagating the electromagnetic wave from the horn and taking into account all the possible discontinuities like the edges of the mirrors, shields and supporting structures. They considered some simplyfing assumptions: both primary, secondary and shield are considered as perfectly reflecting surfaces and the feed-horns are stand-alone not suffering from mutual interactions or coupling. In particular the second assumption is quite strong since each feed-horns "feels" the nearby-horns which may significantly modify the beam response. Of course, one fixed the surrounding structures around the focal plane, the beam pattern is defined. There is the possibility to shape the edge of structures which propagates the incident power away from the detectors (namely towards the shields or screens). However this is complicate and the easiest way to improve the beam pattern lowering the side-lobe contribution, is to increase the edge-taper *i.e.* lowering the incident power at the edge of the primary mirror. But as already seen in Chapter 4 this would degrade the final angular resolution.

The main beam response function is computed in a regular equispaced grid on the (x, y) plane "around" beam center. For this beam part we performed sky convolution directly in this frame. The response function at large angles is instead computed in an regular equispaced grid in polar coordinates refereed to the "beam frame" according to GRASP8 code for optical simulations standards. This is the state-of-the-art of optical code, however its reliability in the case of PLANCK-LFI has not been proved yet. For each colatitude θ_{bf} and longitude ϕ_{bf} in the grid the response function is computed. Here θ_{bf} ranges from 0° to 180° starting from the maximum directivity direction, while ϕ_{bf} ranges from 0° to 360°. These coordinates identify the standard (x_{bf}, y_{bf}, z_{bf}) cartesian beam frame. This is simply obtained from the "telescope" frame by a rotation of the z axis by an angle θ_B in the plane containing the z-axis and the vector $\vec{v_B}$ pointing at the considered beam position. These polar coordinates θ_{bf} and ϕ_{bf} have been used for sky convolution with equispaced grid.

The orientation of these frames as the satellite scans the sky is considered and for each integration the right orientation of the "beam frame" is computed. This is a critical point because of the large asymmetry of the beam pattern in the ϕ_{bf} coordinate as shown in Fig. 5-1 and in Fig 5-2 for the considered 30 GHz beams. Shields are included in the computation of the beam pattern. It is evident the main spillover near $\theta_{bf} \sim 90°$ at a level of ≈ -60 dB which extends by few degrees in both θ_{bf} and ϕ_{bf} directions. There

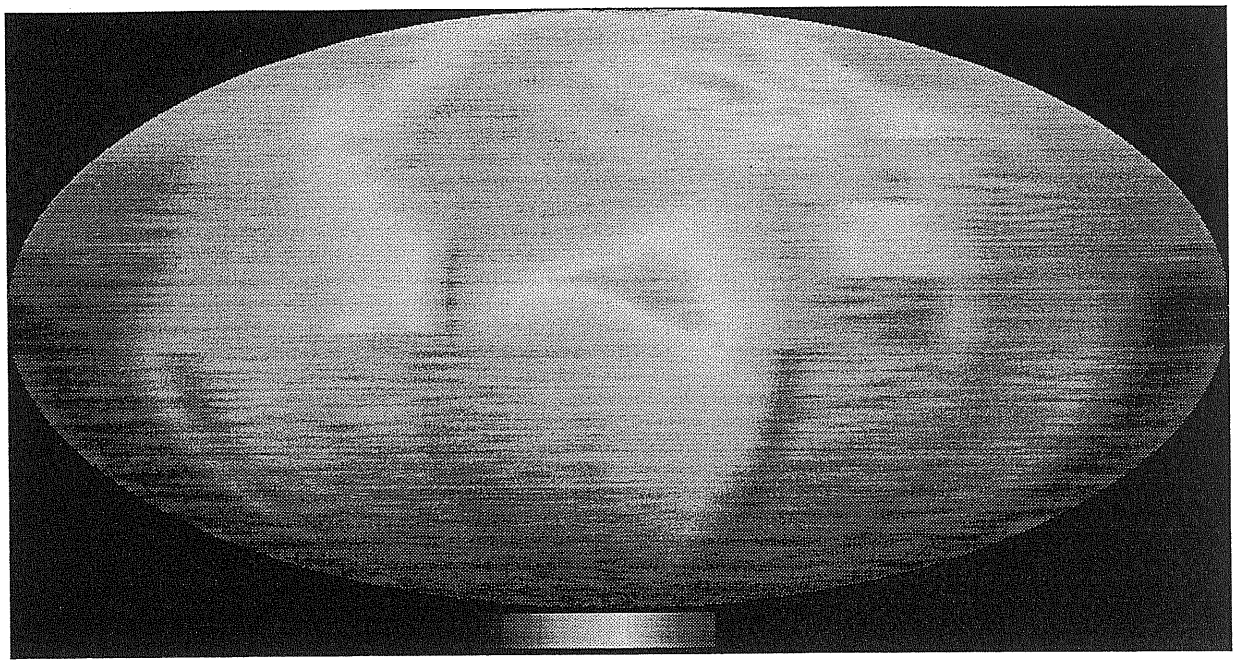

Figure 5-1: Full antenna pattern. The response is normalized to the maximum. The maximum of the response is at the North Pole and decreases towards the South Pole. Note the asymmetry of the response as a function of ϕ_{bf}: particularly evident is the main spillover near the centre of the projection.

are other features with similar response and angular extension not only in the very far part but also "close" to the beam center (see the features at $\theta_{bf} \sim 30°$ in Fig. 5-1). For a more accurate analysis of the stray-light effect, the beam pattern is divided into three parts: the main beam (up to 1.2°), the intermediate beam (from 1.2° to 5°) and the far part for $\theta_{\rm bf} \geq 5°$. These numbers are indicative and depend, for a given telescope design, on the considered frequency and, although weakly, on the feed position in the focal plane. In this case 1.2° corresponds to a level of $\simeq$ -40 dB which is a reasonable level achievable for beam reconstruction through planets, during flight operation; the 5° instead divides regions where response variations are on angular scales less than 1° from those where they occur on scales $\gtrsim 1°$.

In what follows a reduced version of the FS code is considered since computational time for beam convolution is huge particularly for the far side-lobe part. This choice however does not affect final results because the galactic angular power spectrum decreases at small angular scales and those beam pattern features particularly relevant occur at degree or even larger angular scales. Therefore instead of the nominal spin-axis re-pointing of 2.5′ every hour, spin-axis moves by 2°/hour and the number of samplings per circle is 180° *i.e.* one sampling every 2°. In this way the resulting grid is similar to an equispaced grid in cylindrical coordinates with 2° step (ECP, see [80]).

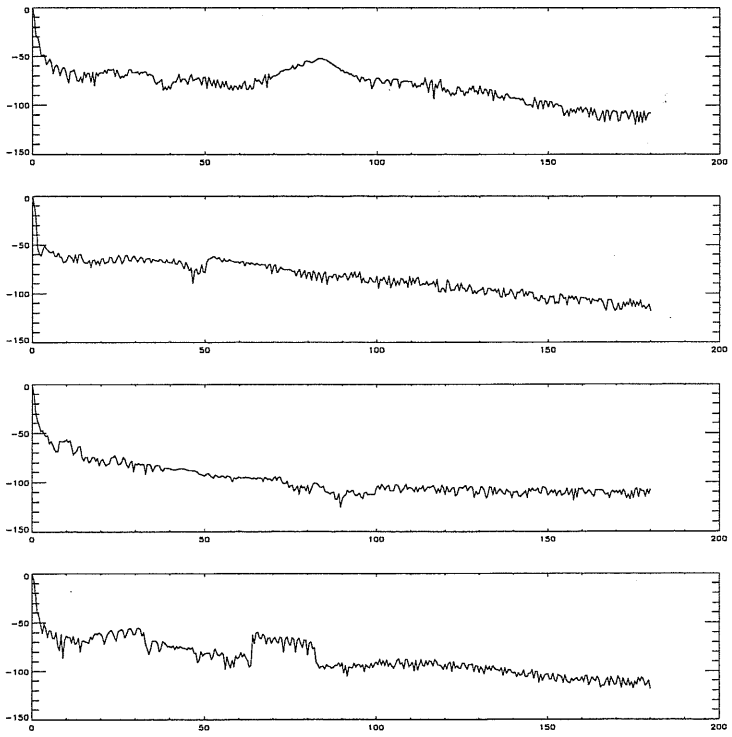

Figure 5-2: Beam response cuts for four different values of ϕ_{bf} as a function of the angle θ_{bf}.

5.2 Microwave sky

For this analysis the synthetic model of microwave sky emission considers synchrotron emission plus HII sources contribution. The LFI full beam pattern is computed for one of the 30 GHz feed-horns and, as shown in §2.6, the major contribution at this frequency are in fact synchrotron and free-free emission. As shown by Paladini *et al.*[84] HII sources may contribute in a non negligible wat to the observed signal especially at 30 and 44 GHz. It is important to quantify the effect on the primary main beam signal, when an HII source enters the far side-lobe of the LFI beam pattern. The diffuse component of free-free emission is not considered here. The synchrotron template (the Haslam map) is therefore cleaned from HII sources to produce a "pure" synchrotron map. The individual HII sources are derived from the catalog of Paladini *et al.*[84] at 2.7 GHz, scaled with a spectral index of 2.1 up to 1 GHz nad then with a flat spectrum to 408 MHz. The "pure" synchrotron map and the sources catalog have been scaled down to 30 GHz with spectral indices of 2.8 and 2.1 respectively. The two components are then recombined.

Given the microwave sky emission model and the full beam pattern, it is possible to make simple estimates of the expected amplitude of the signal entering the different parts of the antenna pattern. This can be done knowing the integrated response of the different antenna parts. The model considered has ~ 13 degrees^2 with antenna temperature, T_A, larger that 2 mK; ~ 73 degrees^2 with $T_A > 1.5$ mK and ~ 230 degrees^2 with $T_A > 1$ mK. The minimum sky value is about 0.05 mK and $\sim 50\%$ of the sky has a signal of about 0.1 mK.

The integrated response (IR) is about 0.6% for a region with $1.2° \leq \theta_{bf} \leq 5°$ and $\simeq 1\%$ for $\theta_{bf} > 5°$. Of course the remaining IR is in the main beam part. Combining the IR of the different antenna parts and the statistical properties of the microwave sky emission model, a peak of contamination at a level of $\sim 10\mu$K and of few μK is expected in the intermediate and in the far part respectively. Considering the signal coming from the main spillover only we expect a contamination of about 2 μK.

These are simple calculations which give only the order of magnitude of the expected stray-light signal from directions out of the main beam. Of course more detailed numerical calculations are needed to have a more robust estimation of the impact of such systematic effect on the relevant PLANCK science.

5.3 Full antenna pattern convolution

The input sky map is pixelized according to the HEALPix scheme [50] with pixel sizes of $3.5'$, $6.8'$ and $55'$ respectively for the main, intermediate and far part of the antenna pattern. These resolutions are adequate for convolution compared with the typical angular size of beam response features in the three parts of the beam pattern. As for the analysis of main beam distortions, the convolved antenna temperature is given by Eq.(4.1) but now the integral in the numerator is over the solid angle of the considered beam pattern part while the integral in the denominator is over the whole antenna solid angle. In the code both integrations are converted into summations over pixels within the considered solid angle.

The main beam part is given on an equispaced cartesian grid with $\Delta x = \Delta y = 0.0005$ rad. The intermediate and far pattern are instead given on a polar coordinates

grid with $\Delta\phi_{bf} = 10°$ and $\Delta\theta_{bf} = 0.1°$ and $0.5°$ respectively. With a simple routine we extract those pixels which fall into a solid angle around a given directions. Of course the directions of pixel centers do not coincide with grid points where the beam response in known. Simple but robust bilinear interpolation [92] have been used to compute beam response in the corresponding directions.

The discretization of the Eq.(4.1) may introduce numerical errors which have to be properly quantified. This can be done by comparing results performed with smaller pixel sizes: numerical errors of about 1 μK and less than 0.1 μK are found for the main and intermediate part convolution. These numbers are very small compared with the amplitude of signal entering in these two beam parts. Furthermore they are also small when compared with the uncertainties and approximations made in the construction of our microwave sky model and in the computation of the antenna pattern by optical code. These results quantify the relevant numerical accuracy of our calculations.

5.3.1 Code testing

The consistency of sky convolution with main, intermediate and far beam patterns has been evaluated exploiting the synthetic microwave sky emission model in §5.2. This is straightforward for the main and intermediate parts since it is expected that, when data streams are coadded into corresponding sky maps, these amps should be similar to the input map except for a beam smoothing in the intermediate part. In fact both main and intermediate parts show the typical shape of galactic emission at the right signal level.

However the situation is rather difficult for the far pattern since it is not intuitive to identify which part of the beam response pick-ups a given signal and hown this is reprojected into the sky. Therefore the validity of the convolution code is tested using a simpler version of both antenna pattern and galaxy spatial template. The antenna patterns assumed to be centred in the optical axis, perfectly symmetric in $\phi_{\rm bf}$ direction and to be the sum of two gaussians: one for the main beam, one for the main spillover at $\theta_{\rm bf} = 90°$ plus a constant low level. We use maps with:

- a spot at the North galactic pole: the output map shows a slab along the galactic equator as we expected (Fig. 5-3);

- a slab in Ecliptic and Galactic coordinates: the maps show signal peaking at the poles (Galactic and Ecliptic) and then decreasing towards the equator; for the slab in Galactic coordinates there is a modulation in longitude related to the main spillover solid angle and to the fact that the scanning strategy is in ecliptic coordinates and not in galactic (Fig. 5-4).

For these two maps it is possible to extract the angular power spectrum: peaks at $\ell = 2$ and higher harmonics are expected since this principal mode corresponds to the 90° symmetry of the beam response. This is in fact what is reported in Fig. 5-5. The whole set of these results give a robust validation of our convolution code both for what concerns the level of the expect signal in the three beam parts and both in its predicted shape when reprojected on the sky. Therefore we can consider the real beam pattern computed at 30 GHz with the modeled microwave emission described in Sect. 5.2.

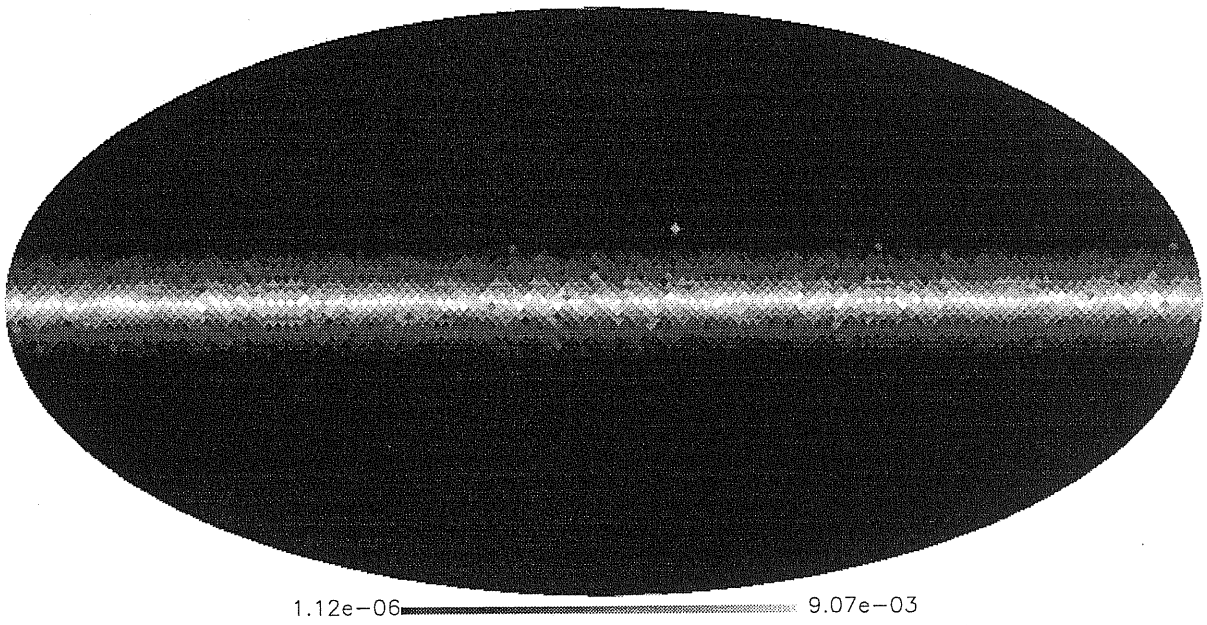

Figure 5-3: The signal in the main beam from the spillover for a polar spot in Galactic coordinates: when the main beam points along the equator the spillover looks at the spot

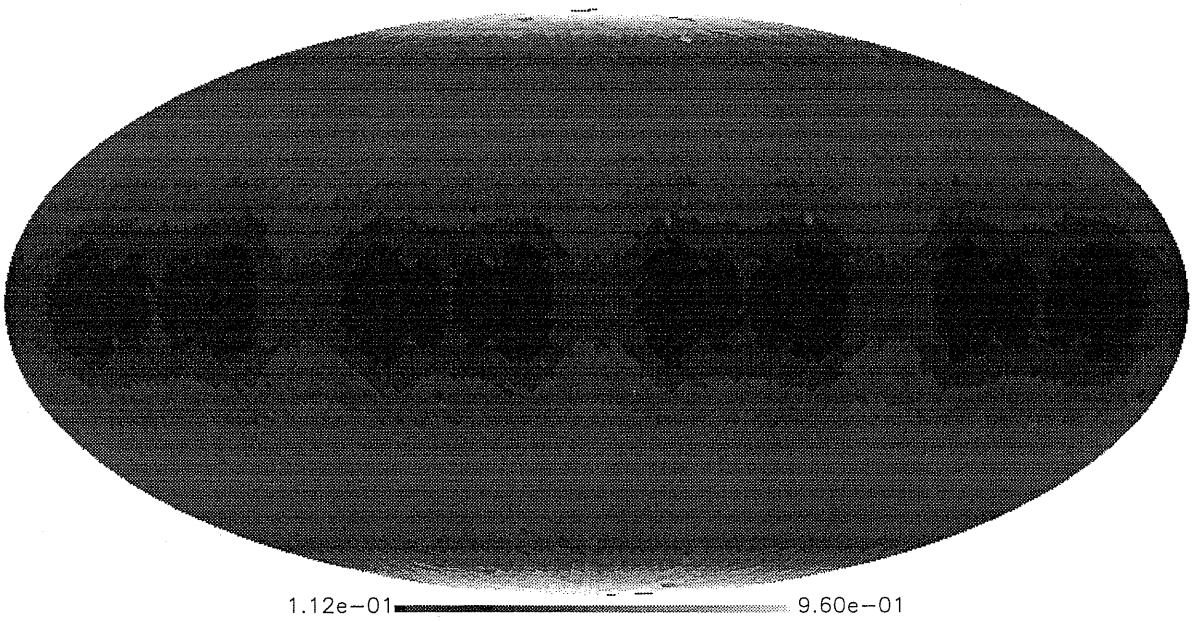

Figure 5-4: The same as before but now in Galactic coordinates: note the longitude modulation due to a combined effect from the spillover and the scanning strategy

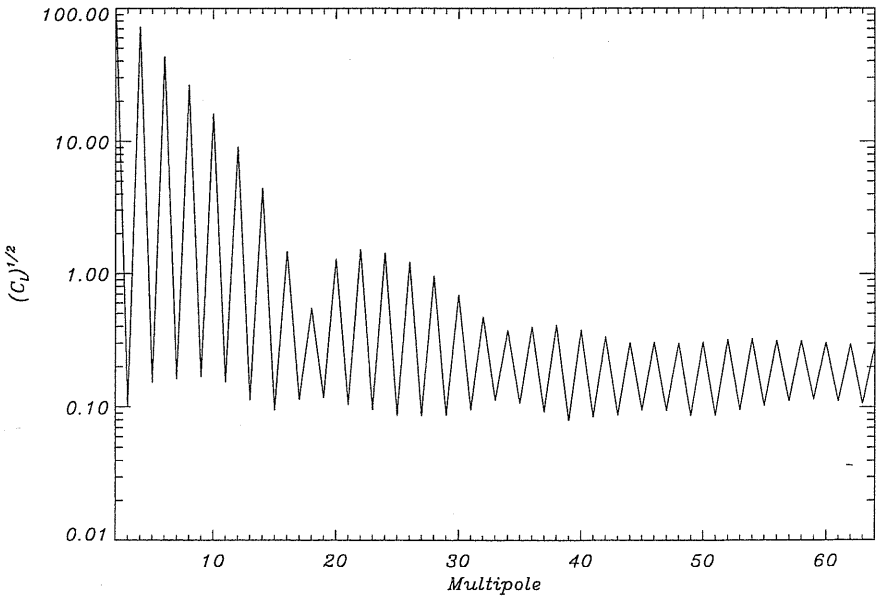

Figure 5-5: Angular Power Spectrum for the map in Fig. 5-4: peaks at $\ell = 2$ and higher harmonics are present due to beam symmetry at 90°. Same results can be obtained with map in Fig 5-4.

5.4 Simulations Results

In the reduced version of the scanning strategy in §5.1, we considered two geometrical configurations: one with the bore-sight angle of 80° and another with $\alpha = 90°$. The first is used by De Maagt *et al.*[30] for computing the full antenna pattern even if it is slightly lower than the actual $\alpha = 85°$ baseline. As for $\alpha = 90°$ the same beam pattern for the 80° case is assumed. Therefore results with $\alpha = 90°$ have to be considered as conservative since the whole telescope and shield geometry would be somewhat different and so the beam pattern. Nevertheless it is interesting to consider this geometrical configuration since it allows two nearly sky coverage (for 1 year of mission) in which beam orientation is totally different. The worst case, as for side-lobe contamination, between the two feed-horn at 30 GHz is considered: the beam is placed in $\theta_B = 5.26°$ and $\phi_B = 126.03°$.

5.4.1 Data streams

The output of the FS code relevant here are two matrices with rows equal to the number of spin-axis positions n_s (here $n_s = 180$) and a number of columns equal to the number n_p of integrations along a scan circle ($n_p = 180$). In the first matrix $\mathbf{N}$ the pixel number corresponding to pointing direction of the main beam is stored; in the second, $\mathbf{G}$, the convolved temperature in these directions is recorded. Here instrumental noise (white and $1/f$ noise) has not been considered: its impact will be addressed in Chapter 6.

In Fig. 5-6 (top panel) signals from three different data streams are reported for the main, intermediate and far part of the antenna pattern for the 80° case: solid line is the main beam pattern signal, dashed line is the intermediate signal (multiply by 50) and dot-dashed line is the far side-lobes signal (multiply by 500). As expected the intermediate part is very similar to the main beam pattern a part for a smoothing effect and reduced intensity because of the different integrated response. Two maxima corresponding to beam galactic plane crossing are present, for each scan circle, in both signals. The case for the far pattern is quite complicate: maxima due to the main spillover and to beam features close the main beam are present and occur also where main beam signal is particularly small. In Fig. 5-6 (bottom panel) the ratio intermediate/main and far/main are reported: the contamination from intermediate part is higher where galactic signal is high, while for the far part this contamination peaks in regions where galactic signal is quite small.

A comprehensive view of all the scan circles is reported in Fig. 5-7. The x-axis of the figure is the spin-axis longitude while the y-axis is the telescope latitude. It is worth noting how features in the far beam pattern signal are very different comparing the first and the second six months of missions (the left half and the right part of each panel). This is because of the different orientation of the beam pattern and in particular of the main spillover with respect to the sky signal (galactic plane). Similar results are obtained for the $\alpha = 90°$ case. The maximum of contamination is about 13 μK from the intermediate part and ~ 6 μK from the far pattern; the mean value in the far pattern is about $\sim 2\mu$K. These values are in good agreement with our previous simple estimations.

Following Puget & Delabrouille [95], Maino *et al.*[72] decomposed each scan circle into Fourier series:

$$g(\xi) = \sum_{m=0}^{n_p/2-1} \sqrt{2} a_m \cos(m\xi + \xi_{0,m}) \,, \tag{5.1}$$

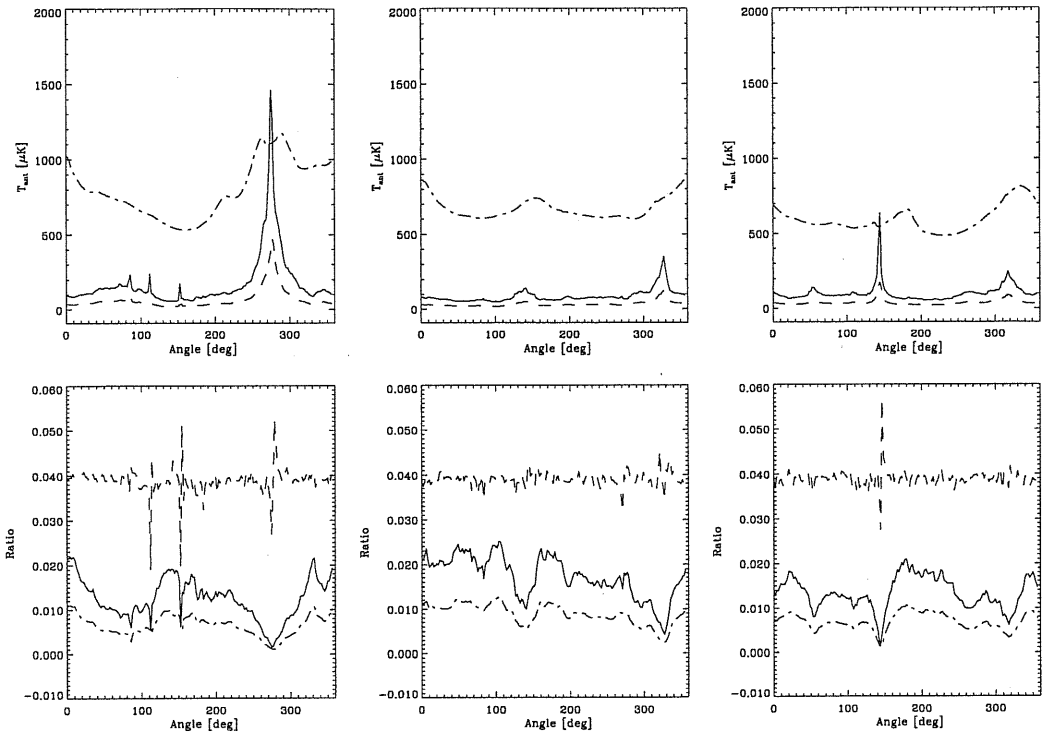

Figure 5-6: Top Panels: absolute signals entering main (solid lines), intermediate (dashed; multiply by 50) and far (dot-dash lines; multiply by 500) antenna pattern for three different sky directions (0°, 60° and 120° spin-axis longitude) for $\alpha = 80°$. Bottom panels: ratio between intermediate/main (dashed, multiply by 5.), far/main (solid) and far/intermediate (dot-dashed, multiply by 10.)

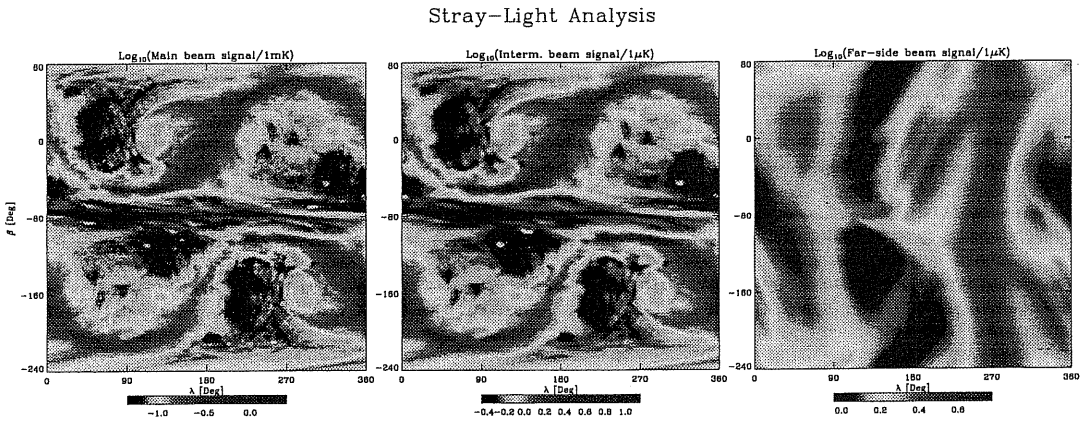

Figure 5-7: Summary of the whole set of data stream for the main (left), intermediate (centre) and far antenna pattern (right). Units are mK for the main beam and μK for intermediate and far pattern and the angle $\alpha = 80°$. The smoothing effect is clearly evident in the intermediate case with respect the main beam signal. Also note the different shape of the far signal with respect the first and second 6 months of mission

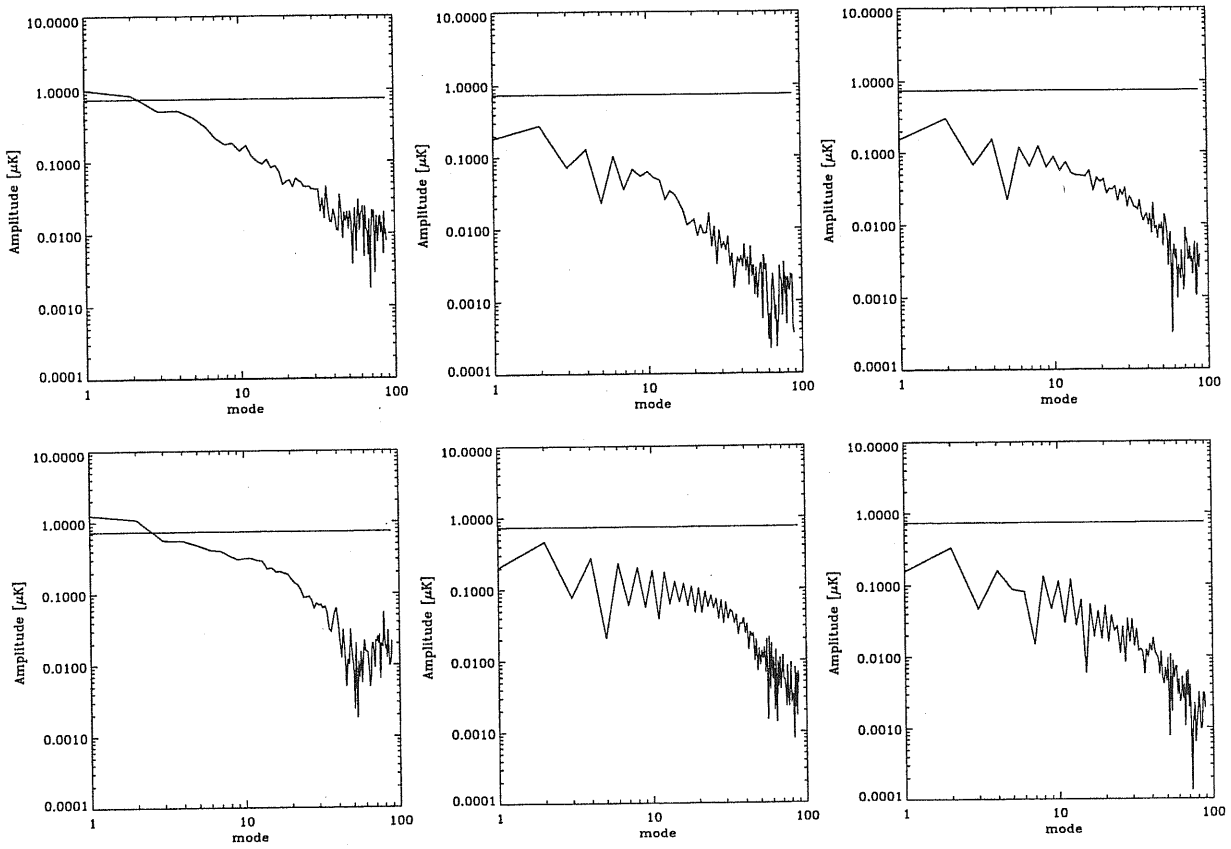

Figure 5-8: Fourier decomposition for the usual three scan circles as in Fig. 5-6 for the signal of intermediate plus far antenna pattern compared with the white noise level for 4 receivers at 30 GHz for the 80° (top) and 90° (bottom). Note the for all relevant modes $m \gtrsim 3$ the signal is smaller than white noise

where $g(\xi)$ is the signal in the ξ position along the scan circle. Given n_p data points along a scan circle, modes m up to $m = n_p/2$ could be exploited since two coefficients a_m and $\xi_{0,m}$ have to be calculated solving a linear system. The amplitude a_m for each mode m, which is analogous to the multipole ℓ for the usual spherical harmonics expansion, has to be compared with the amplitude of instrumental noise. Far and intermediate patterns are summed together and compared with the white noise for the 4 LFI 30 GHz receivers. Noise per mode is computed averaging a number of scan circles which span an arc equal to the $33'$ of FWHM at 30 GHz. Results are shown in Fig. 5-8 for the same three scan circles considered before, and for $\alpha = 80°$ and $90°$. For modes $m \gtrsim 3$ the stray=light contribution is well below the noise level and becomes 10 times smaller for modes $m \gtrsim 10$. This behavior is also due to the decreasing of the galactic fluctuations at smaller angular scales and seems to indicate a small contamination from stray-light.

5.4.2 Stray-light maps

The above approach is particularly useful for the data analysis during the mission since PLANCK will continuously scan circles in the sky. It is however interesting to reproject the stray-light signal into sky maps in order to compute their power spectrum and compare it with the white noise level.

Sky maps are obtained simply coadding pixels temperature in the data streams. For $\alpha = 80°$ a single map covering 1 year of mission is produced; for $\alpha = 90°$ two maps are instead considered coadding separately the first and the second sic months of mission. In this way it is possible to quantify in the stray-light angular power spectrum, the impact of different beam orientations with respect to sky signal.

Maps for main, intermediate and far antenna pattern for 1 year of mission are reported in Fig. 5-9. As expected and as already seen in the data streams, the map for the intermediate part is similar to that of the main beam a part for a smoothing and a rescaling in signal due to the different integrated response. The far pattern in completely different: structures at the μK level are present also at high galactic latitudes; signal along the galactic plane is still present due to the part of the far-side lobe closer to the intermediate pattern region.

We can compute the angular power spectrum for the stray-light signal from the intermediate and far antenna pattern and compare these spectra with that of the white noise for 4 receivers at 30 GHz. The spectra are computed using a cut in latitude: only those regions with $|b| \geq 30°$ have been considered. The first and second six months of mission are separately reported in Fig. 5-10 on the left and on the right panels respectively. It is interesting to note that in the second six months the power spectrum from the far part dominates over that from the intermediate part while they are comparable in the first six months of mission. However for multipole $\ell \gtrsim 10$ the level of stray-light signal is significantly smaller than the white noise level and decreases very rapidly as ℓ increases because of the decrease of galaxy fluctuations at smaller angular scales.

5.5 Conclusions

The impact of stray-light on PLANCK-LFI observations for one of the 30 GHz feed-horns with different and almost complementary approaches has been studied. Stray-light contamination has been properly quantified by means of: absolute and relative signals in the data streams, Fourier decomposition, stray-light maps and angular power spectrum. With this set of simulation results it is possible to draw some conclusions and state open issues.

The peak level of stray-light has to be found at a level of $\sim 13\mu$K which is comparable to the sensitivity per pixels. This signal is mainly due to those part of the beam displaced only by few degrees from the main beam direction. It occurs at low galactic latitudes where the galactic signal entering the main beam does not allow an accurate measurement of the CMB signal.

It is clear that the real problem comes with contamination from the far side-lobes for which the signal peaks at $\sim 6\mu$K with a mean value of $\sim 2\mu$K. This is smaller in absolute value than that from the intermediate part, but it occurs at high galactic latitudes where we expect to extract the most relevant CMB information. However these are not so "critical" numbers being less (but not so small) than the rms sensitivity.

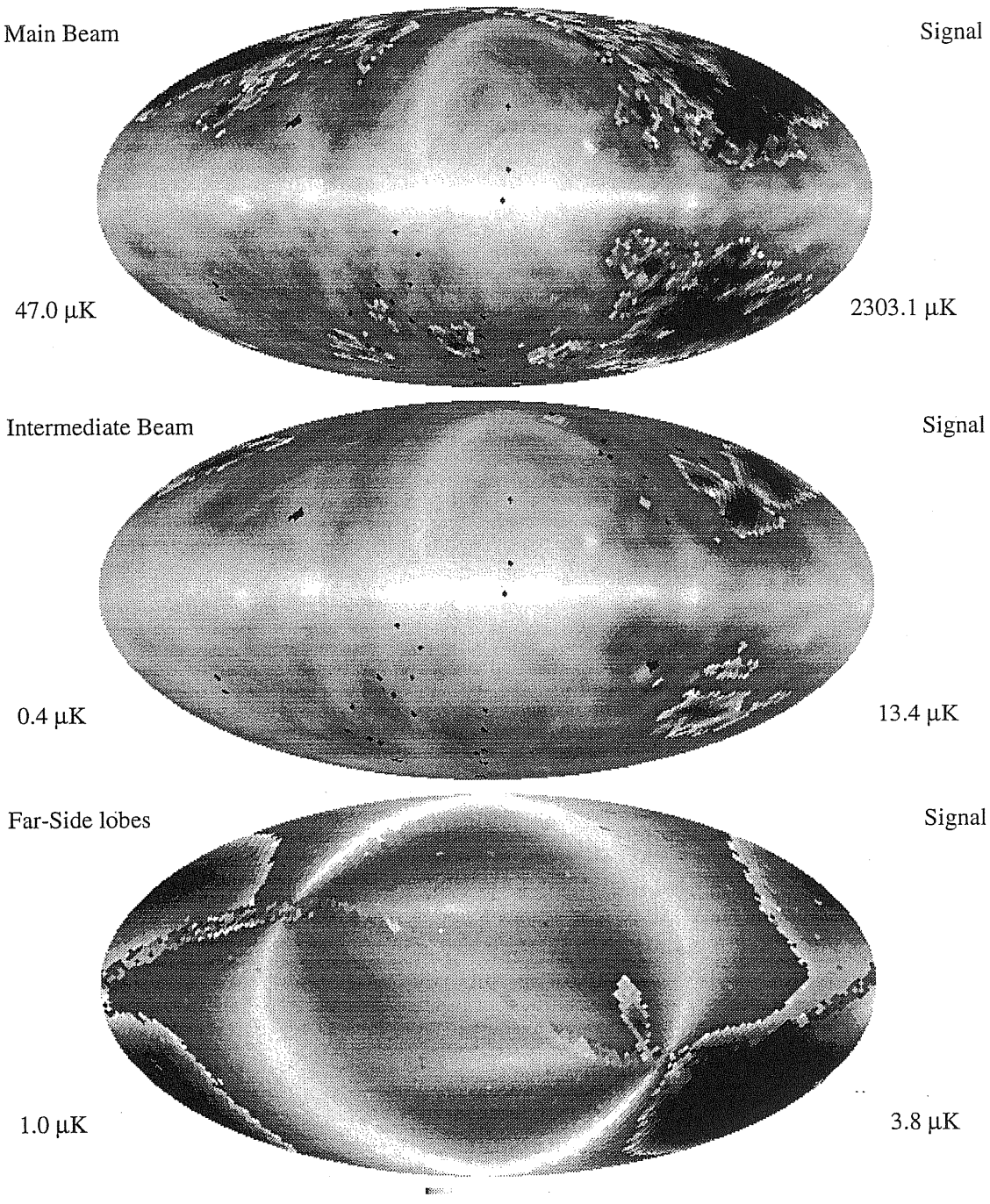

Figure 5-9: Main, intermediate and far antenna pattern response at 30 GHz for the $\alpha = 90°$ for one year of mission

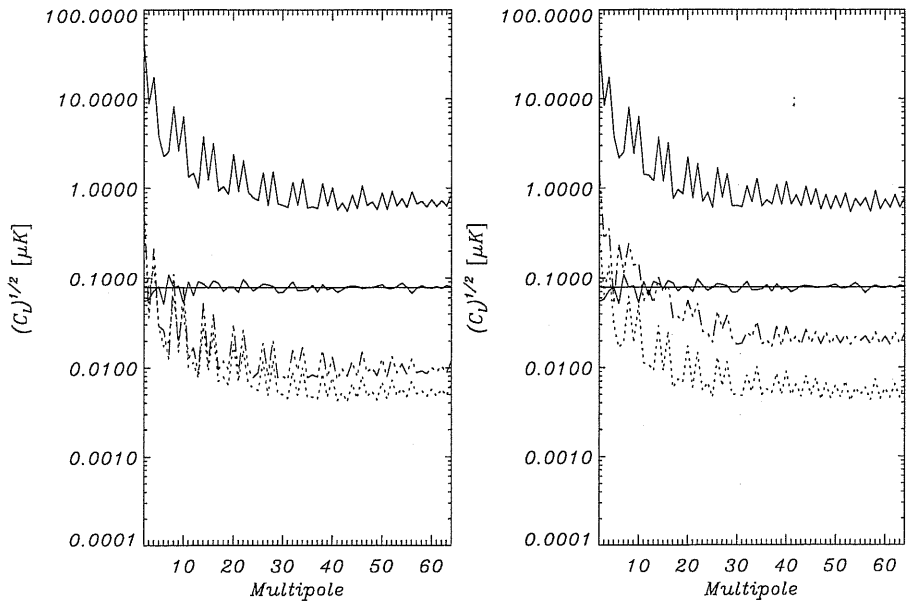

Figure 5-10: Angular Power Spectrum for main (red), intermediate (cyan) and far (blue) pattern at 30 GHz with a latitude cut of 30°, for the first (left) and second (right) 6 months of mission: note that far pattern power spectrum dominates that from the intermediate part for the first 6 months while they are comparable in the second ones. The black spectrum is the white noise spectrum superimposed on the theoretical expected value.

Furthermore around the Ecliptic polar caps the sensitivity is several times better than the average because of the PLANCK scanning strategy. For these regions our results indicate a possible issue. In particular this might be critical for polarization measurements which are possible in these regions for their higher sensitivity. A further reduction of stray-light contamination has to be achieved for a better estimation of polarization signal.

These results are relative to the 30 GHz which is not a cosmological channel. In this case we found no large contamination from stray-light at large multipoles and hence there is not a real degradation of CMB science at 30 GHz due to stray-light. We need an antenna pattern for one of the 70 and 100 GHz channels in order to evaluate the impact of stray-light contamination directly on the main scientific PLANCK goal. It is possible to estimate the order of magnitude for galactic stray-light at 100 GHz assuming the same beam shape as at 30 GHz and simply rescaling the galactic emission properly. Scaling the synchrotron emission with a spectral index $\beta_{\rm sync} = -2.9$, free-free emission with $\beta_{\rm ff} = -2.1$ and including dust emission modeled as a power law with $\beta_{\rm dust} = 2.5$ and $T_{\rm dust} = 20$ K, the ratio between overall microwave emission between 30 and 100 GHz is ~ 0.4. Rescaling results at 30 GHz by this factor we expect to have at 100 GHz a stray-light signal from intermediate beam of the order of 5.2μK and of $\sim 2.4\mu$K from the far side-lobes. These simple estimates yield results which are well below the nominal noise per resolution element at 100 GHz which is 12μK. Of course more accurate simulations have to be performed to verify such results.

These results hold for this very idealized case in which several assumptions have been made both in the computation of the beam pattern, both for what concerns the other systematic effects which are supposed to be excately known and properly corrected. It is worth to note that the FS code can take into account several systematic effects at the same time: it is quite simple, for example, to include the instrumental noise in the code (see Chapter 6); once a thermal model of the instrument and of the whole PLANCK payload will be available, it is straightforward to include this into the FS. No attempts have been made till now to consider all systematic effects together. This is an important point since out "not so critical" results will be certaintely degraded by more realistic simulations.

Chapter 6

The $1/f$ noise[1]

This Chapter aims to introduce and address the issue of receiver performances for the Low Frequency Instrument of the PLANCK mission. Instabilities in the receiver amplifiers are one of major sources of possible systematic effects. They may lead to stripes in the final maps because of the PLANCK scanning strategy. This is the so-called $1/f$, or low frequency, noise. It is possible to parameterize the $1/f$ noise with the "knee-frequency" f_k defined as the frequency at which the $1/f$ noise equals the ideal white noise sensitivity. The knee-frequency has to be kept as low as possible compared with the spinning frequency f_s of the PLANCK spacecraft. The LFI radiometers are designed to yield the lowest f_k and a key parameters is the reference load temperature which has to be very close to the observed sky temperature.

It is of great importance to clearly understand the source of this systematic effect in order to minimize its impact in final results also with one or more algorithms able to destripe the final maps. Accurate simulations have been performed and presented here and the effect of $1/f$ noise is quantified by the *rms* of additional noise with respect an ideal pure white noise case. A simple but general technique for removing this systematic effect is implemented and yields impressive results.

This chapter is organized as follows: §6.1 derives the expression of the f_k as a function of the LFI radiometer parameters; in §6.2 the main inputs to the FS code are reported and §6.3 describes the technique for noise data streams generation. §6.4 shows the map-making algorithm used for passing from data streams to sky maps and the modified model for galactic emission considered here is in §6.5; the concept of the de-striping code is in §6.6 and simulations results in §6.7. Conclusions are reported in §6.8.

6.1 The LFI radiometers

A detailed description of the LFI radiometers is reported in §3.4.1 where we have pointed out that the radiometers design is optimized to minimize the $1/f$ noise from amplifiers. Seiffert *et al.*[103] have in fact evaluated the contribution to $1/f$ noise from several possible sources in the specific case of LFI receivers. The main source resulted to be gain fluctuations in the HEMT amplifiers showing a typical $1/f$ spectrum. This behavior has been

[1]Partially based on D. Maino *et al.*, *A&ASS*, in press

accurately measured by Pospieszalski [90] and Wollack [129] but, up to now, a comprehensive theory explaining the origin and the spectrum of these fluctuations is not available. It is believed that the possible source of this behavior are impurities present in the layer where the HEMT amplifiers are built. Actually at TRW in Los Angeles, the world leader in design and production of ultra-low noise HEMT amplifiers, a project is on-going to clearly understand the physical origin of gain fluctuations in order to reduce them and obtaining better performances. It is interesting to mention the $1/f$ noise is a quite general phenomenon in physics occuring in a large variety of situations: from quasar light curves to current in vacuum tubes, from sun-spots number to current velocity in the deep Pacific ocean [91]. The common feature of this broad range of processes is that there is not a clear interpretation of them.

In a multi-stage amplifiers the final noise temperature T_n is given by $T_n = T_1 + T_2/G_1 + T_3/(G_1G_2) + ...$, where T_1, T_2,.. and $G_1, G_2, ...$ are the noise temperature and the gain from the different amplification stages. Therefore gain fluctuations translate into noise temperature fluctuations ΔT_n with the same spectral shape:

$$\frac{\Delta T_n}{T_n} = \frac{A}{\sqrt{f}}. \tag{6.1}$$

Typical value of A for PLANCK receivers at 30 and 44 GHz is $A \simeq 1.8 \times 10^{-5}$ Hz$^{1/2}$. At higher frequencies, the reduced gate widths in the amplifiers yields to fluctuations larger by a factor of $\sqrt{2}$ thus yielding to $A \simeq 2.5 \times 10^{-5}$ Hz$^{1/2}$ for 70 and 100 GHz [45, 127]. Noise fluctuations ΔT_n can mimic a real variation in sky signal. Since the two amplifiers (see Fig. 3.3) have uncorrelated noise, the observed change in radiometer output is:

$$\Delta T_{\rm equiv} = \sqrt{2}\Delta T_n \left[\frac{1-r}{2}\right] = \sqrt{2}\left[\frac{A \times T_n}{\sqrt{f}}\right]\left[\frac{1-r}{2}\right], \tag{6.2}$$

where the factor $\sqrt{2}$ accounts for the uncorrelated noise between the two amplifiers. The "knee-frequency" f_k is defined as the post-detection (*i.e.* after the diode and DC amplifier) frequency at with $\Delta T_{\rm equiv}$ equals the white noise ideal sensitivity $\Delta T_{\rm wn}$. Using an integration time $\tau = 1/(2\Delta f)$ and $\Delta f = 1$ Hz, the knee-frequency is

$$f_k = \frac{A^2 B}{8}(1-r)^2 \left(\frac{T_n}{T_n + T_x}\right)^2, \tag{6.3}$$

which shows the dependence of f_k upon different radiometer properties (*e.g.* the bandwidth B, the noise temperature T_n, intrinsic level of gain fluctuations A). In Fig. 6-1 two noise realizations are shown: one with white and $1/f$ noise (left panel) and one with pure white noise (right panel). The difference between the two is much more evident when comparing their power spectra: the pure white noise case is flat while a rise for $f < f_k$ occurs in the white plus $1/f$ noise case. In order to reduce the effect of the $1/f$ noise, f_k has to be kept as low as possible particularly compared with the spin frequency of the satellite $f_s = 0.0167$ Hz, corresponding to 1 r.p.m.. Theoretical knee-frequency values for the back-up solution at 20 K load are $\simeq 0.05$ Hz at 30 GHz and 0.11 Hz at 100 GHz; with a 4 K reference load these values drop to 1.24×10^{-3} Hz and 1.14×10^{-3} Hz at 30 and 100 GHz respectively. It has to be noted that these are theoretical values for f_k which have to be probed in real hardware.

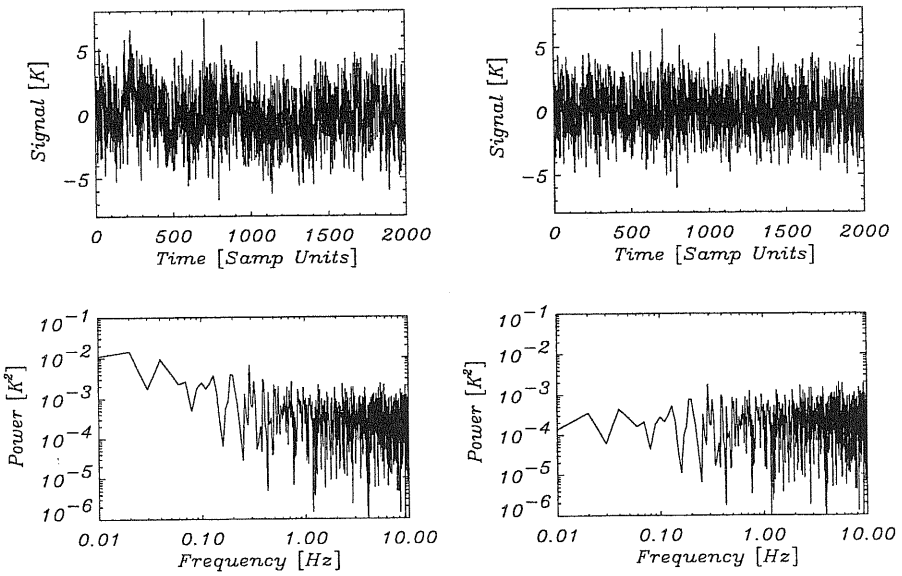

Figure 6-1: Comparison between two time series with only white noise (right panels) and white plus $1/f$ noise (left panels). The difference is much more clear in their power spectra.

6.2 A reduced flight simulator

In order to evaluate the effect of $1/f$ noise for LFI receivers, accurate simulations are performed using the FS code described in §3.6. Instead of the present baseline for the scanning strategy, a reduced version is considered. These are the modifications:

- spin-axis moves by $5'$ every two hours instead of $2.5'$ every hour;
- samplings scheme assumes 3 samplings per FWHM while the present LFI baseline consider 4 samplings at 100 GHz and $\simeq 12$ samplings at 30 GHz since the sampling rate is the same regardless the frequency.

A further simplification arises from the fact that instead of the single minute ring, the averaged over the 120 scan circles, for which the spin-axis points always in the same direction, is considered: this forms the 2-hours set used. The averaging of scan circles is like a low-pass filtering operation and, as long as $f_k \gtrsim f_s$, this means that only the very low frequency components of the $1/f$ noise survive to this filter operation. Wright [130] has shown that the possibility to pass-filter data from a single ring with filters other than the simple average may help in removing the $1/f$ noise. This turns out to be particularly useful for f_k values typical of Total Power receivers which in general are larger than those considered here for LFI receivers. Therefore these filters are not implemented here.

These modifications allow to explore a large region of a multi-parameter space (beam location, knee-frequency f_k, scanning strategy and bore-sight angle α) on a reasonable time-scale.

6.3 Noise generator and CPU time

In general the noise spectrum has the form [29]:

$$S_{\rm noise}(f) = a\left[1 + \left(\frac{f_k}{f}\right)^{\beta}\right], \tag{6.4}$$

where a is a normalization factor, related to the white noise sensitivity, and β has typical values from 1 to 2.5 according to the source of noise (gain instabilities or thermal drifts). The case $\beta = 1$ is the $1/f$ noise case. It is a good approximation to take $S_{\rm noise}(f)$ vanishing for $f < f_{\rm min}$ and $f > f_{\rm max}$: Delabrouille [29] suggested $f_{\rm min} \approx 1/T_{\rm mission}$ and $f_{\rm max} \approx 1/2T_{\rm sampling}$, where $T_{\rm mission}$ and $T_{\rm sampling}$ are the total mission time and sampling time respectively.

The noise data streams generation technique implemented involves the use of FFT (Fast Fourier Transform). Let be $n(t)$ the noise data stream: in general this can be expanded into its Fourier components:

$$n(t) = \sum_k c_k e^{-ikt} = \sum_k a_k \cos(kt) + i b_k \sin(kt)\,. \tag{6.5}$$

The simple condition that $n(t)$ has to be real yields to some useful properties for the a_k and b_k coefficients: $a_k = a_{-k}$ and $b_k = -b_{-k}$. Furthermore $\langle n(t)\rangle = 0$ and therefore the same must hold for a_k and b_k aspectation values. It is possible to work directly in Fourier space and generate the real (a_k) and the imaginary (b_k) part of the noise stream. These are normal distributed random numbers with variances given by $\langle |a_k|^2\rangle = \langle |b_k|^2\rangle = 1/(2N)$ where N is the total number of samplings for which the noise stream is computed. In this way the noise stream has unity variance. Multipling the a_k and b_k by the square root of the Eq.(6.4) generates different spectra depending on f_k and β values. Computing the FFT on these spectra yields to real (time) noise data stream with the desired spectrum.

In what follows a noise stream of about 2×10^6 data points is considered. This corresponds, in the reduced scanning strategy adopted here, to 8 spin-axis positions or 16 hours of observations. This time span seems to be reasonable considering the present knowledge of actual hardware performances and the required computational time. For example at 30 GHz, generating this noise data stream takes ~ 1 minute thus yielding $\sim 5 \div 6$ hours for one year of mission, on a Silicon Graphics machine with 2 Gb of RAM and 225 MHz clock speed.

Most of the CPU time is spent in FFT operations. The possibility to generate noise spectra as in Eq.(6.4) without the use of FFT directly in time domain is presently under study [124] and seems very promising: theoretical calculations yield several factors of CPU time reduction.

The large CPU time is not the only problem in these kind of simulations: another aspect is related to the available RAM. In the "reduced" FS considered here the required RAM is $\sim$ 150 Mb for double precision output which easily goes over 1 Gb for the real scanning strategy (2.5′ spin shift and 12 samplings per FWHM at 30 GHz). In principle also the implemented destriping code (see §6.6) requires a large amount of RAM being $\sim$ 250 Mb for this "reduced" FS case.

This asks of course for very powerful machine with large RAM and possibly with multiple CPUs. The FS code structure is naturally suitable for parallel computation:

each CPU can perform the scanning only for a small number of scan circles (it depends of the total number of CPUs and their RAM) since they do not need any exchange of information except the input map. This will reduce in a considerable way not only CPU time but also the requirements on RAM and therefore the parallelization of the FS code is currently under study.

6.4 From data streams to sky maps

The final output of the FS code, as in Chapter 5, are matrices with a number of rows equal to the spin-axis positions n_s (for one year of mission $n_s \sim 4320$ in the reduced version of the scanning strategy adopted here) and a number of columns equal to the number of integration along one scan circle n_p (here $n_p \sim 2160$ weakly dependent of the bore-sight angle α). More precisely these matrices are: the pixel number for each scan circle $\mathbf{N}$, the sky temperature plus white and $1/f$ noise $\mathbf{T}$, the sky temperature with only white noise $\mathbf{W}$ and the signal as observed without any noise source $\mathbf{G}$. The $\mathbf{W}$ and $\mathbf{G}$ matrices are computed in order to study the degradation of the $1/f$ noise with respect the pure white noise case and the validity of the geometrical part of the FS code which reproduces the scanning strategy.

The input and output maps are in HEALPix pixelization scheme [50] (see the HEALPix Web site at `http:\\www.tac.dk \~healpix`): an input map resolution of $3.5'$, which corresponds to 1.2×10^7 pixels, is used. Actually this is the pixelization selected for PLANCK: this has the advantages of equal-area pixels (useful for integration of sky signal when performing beam convolution), hierarchical structure and iso-latitude pixels distribution which allows fast map generation and extraction of power spectrum by FFT.

It is possible to specify in the FS code the temperature output data stream resolution from $3.5'$ to higher values (smaller resolution). Therefore several matrices $\mathbf{N}$ are stored at different resolutions allowing to test the effect of more or less stringent crossing condition in the destriping algorithm (see §6.6).

From the data streams it is quite simple to obtain "observed" simulated maps: using $\mathbf{N}$ and $\mathbf{T}$, the temperature of those pixels observed several times during the mission is coadded. The same is applied for the $\mathbf{W}$ and $\mathbf{G}$ matrices and a sensitivity map is computed knowing how many times a single pixel is observed. Fig. 6-2 shows a noise map (white and $1/f$ noise) after signal subtraction ($\mathbf{T}$-$\mathbf{G}$): stripes are clearly present.

6.5 Microwave sky

The CMB simulated sky is the same presented in §4.2. As for galactic emission a slightly different model is considered here. The galactic emission has in fact the spatial template of the dust emission [102] but the signal has been normalized to include contributions from synchrotron, free-free and dust according to *COBE*-DMR results [62]. It is worth to mention that, as reported by [31, 32, 33, 62], *COBE*-DMR, Saskatoon QMAP and Tenerife data seem to show a strong correlation of microwave emission from 10 to 90 GHz with dust templates rather than with synchrotron template. This is an indication that synchrotron emission is very small for $\nu \gtrsim 30$ GHz while the major contribution comes from free-free emission which has, at least, one component partially correlated with dust.

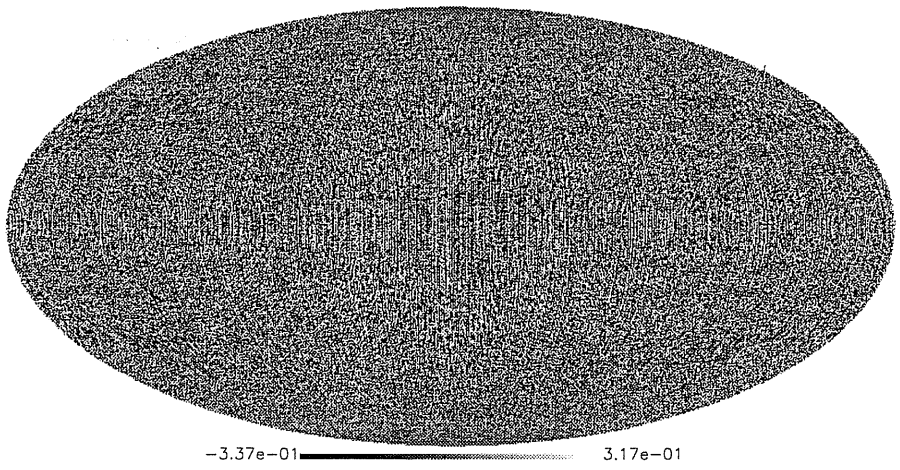

Figure 6-2: Pure noise (white plus $1/f$) map before destriping after signal subtraction: stripes are clearly present. The $f_k = 0.05$ Hz and the spin-axis is kept always on the Ecliptic plane during the mission.

On the basis of these results, the overall low-frequency emission has been over-estimated by a factor ≈ 10. Galactic model is therefore pessimistic with respect galactic signal and fluctuations. Of course the impact of the sky temperature is small being T_x a small fraction of the noise temperature T_n: this is in fact ~ 10 K while $T_x \approx 3$ K and the maximum galactic contamination is about 44 mK.

The input map is convolved by a gaussian beam with the nominal FWHM of the channel considered in the simulation. This is done since we want to estimate the effect of $1/f$ noise alone and therefore convolution with "real" beam shapes, which are far from gaussians (see §4.4), introduces other spurious systematic effects.

6.6 Destriping the $1/f$ noise

A simple technique to eliminate gain fluctuations due to $1/f$ noise is implemented. This is derived from the COBRAS/SAMBA Phase A study report [9] and from a re-analysis in [29]. As reported by Janssen *et al.*[57] and Delabrouille [29] the effect of $1/f$ noise can be seen as one or more additive levels different for each scan circle. The low-pass filter done by averaging over the scan circle relative to the same spin-axis position in a 2-hours period, leaves only the lowest $1/f$ noise frequencies. For the set of parameters considered it is a good approximation to model the "averaged" $1/f$ noise as constant baseline different for each scan circle.

We want to obtain these baselines for all the circles and re-adjust the signal correspondingly. Delabrouille [29] suggested the possibility that working with multiple baselines per circle (n_l = number of baseline levels) may result in a better destriping. This is implemented in the destriping code and it is equivalent to divide the number of columns of output matrices in n_l parts: the output matrices are with $n_s \times n_l$ rows and n_p/n_l columns.

The possible improvement adopting multiple baselines per circle depends on the value of f_k and also on the noise spectrum (namely the exponent β). The noise shape exploited by Delabrouille [29] has a typical value $\beta = 2$ for thermal drifts in bolometers. For the LFI radiometers there is no significant improvement in using multiple baselines per circle, meaning that the $1/f$ noise is quite stable with each averaged circle. Therefore a single baseline level A_i per circle is assumed.

In order to estimate the different A_i we have to find common pixels observed in different scan circles and the pixel size in the matrix $\mathbf{N}$ is a key parameter. Increasing the resolution in $\mathbf{N}$ reduces the number of crossing possibly yielding to lower destriping efficiency. On the contrary adopting resolution lower than the resolution of the input map and of the matrix $\mathbf{T}$, introduces extra noise. This is because of real sky temperature variations, within the scale corresponding to the adopted lower resolution in $\mathbf{N}$, which may introduce artifacts in the destriping code. The adopted pessimistic galactic emission model (§6.5) which has gradients larger than those inferred by current data, emphasizes this effect therefore yielding conservative results.

In the following N_{ij}, T_{ij} and E_{ij} will denote the pixel number, the temperature and the white noise level for the pixel in the i^{th} row and j^{th} column. A generic couple of different observations of the same pixel is denoted with π which ranges between 1 and n_c, the total number of common observations. In this notation π is related to two elements of $\mathbf{N}$: $\pi \rightarrow (il, jm)$ where i and j identify different scan circles and l and m are the respective positions in each of the two circles. Instead of using $\mathbf{N}$ for searching common pixels, equivalent matrices computed at higher resolution could be used: this requires two pixels to satisfy a more stringent crossing condition.

We want to minimize the quantity:

$$S = \sum_{\text{all pairs}} \left[\frac{[(A_i - A_j) - (T_{il} - T_{jm})]^2}{E_{il}^2 + E_{jm}^2} \right] = \sum_{\pi=1}^{n_c} \left[\frac{[(A_i - A_j) - (T_{il} - T_{jm})]^2}{E_{il}^2 + E_{jm}^2} \right]_\pi \tag{6.6}$$

with respect to the unknowns A_i. The sub-index π indicates that each set of (il, jm) is used in the summation. It is clear that S is quadratic in all the unknowns and that only differences between A_i enter into Eq.(6.6). The solution is indeterminate apart from an arbitrary additional constant (with no physical meaning in anisotropy measurements). We chose to remove this indetermination by requiring that $\sum_{h=1}^{n_s} A_h = 0$. With this modification Eq.(6.6) becomes $S' = S + (\sum_{h=1}^{n_s} A_h)^2$. After some algebra we finally get:

$$\frac{1}{2}\frac{\partial S'}{\partial A_k} = \sum_{\pi=1}^{n_c} \left[\frac{[(A_i - A_j) - (T_{il} - T_{jm})] \cdot [\delta_{ik} - \delta_{jk}]}{E_{il}^2 + E_{jm}^2} \right]_\pi + \sum_{h=1}^{n_s} A_h = 0\,, \tag{6.7}$$

for all $k = 1, ..., n_s$ (here δ is the usual Kronecker symbol). This translates into a set of n_s linear equation:

$$\sum_{h=1}^{n_s} C_{kh} A_h = B_k, \quad k = 1, ..., n_s \tag{6.8}$$

which can be easily solved. Furthermore the matrix $\mathbf{C}$ of the C_{kh} coefficients is, by construction, symmetric, positive defined and non singular. The first property allows to hold in memory only one half of the matrix $\mathbf{C}$ (e.g. the upper-right part) lowering the requirements on RAM; the second preserves the symmetry since no exchange of rows or

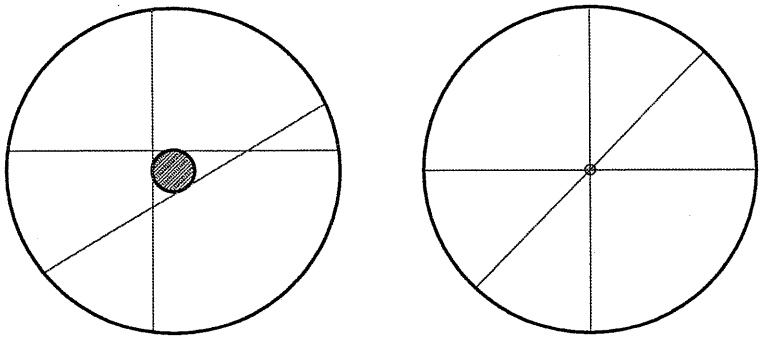

Figure 6-3: Polar view of scan circles crossings. Left panel - Beam with $\phi_B = 45°$ and $\theta_B = 2.8°$: scan circles crossings are in a large region around the Ecliptic polar cap. Right panel - Beam with $\phi_B = 0° = 180°$: scan circles crossings are only at the Ecliptic poles. The region within the small circle of radius $\sim \theta_B \sin(\phi_B)$ remains unobserved.

columns is required while solving the system [114]. The non-singularity of $\mathbf{C}$ is verified provided that there are enough intersections between different scan circles and hence is related to the resolution at which we look for common pixels, to the scanning strategy and beam location. A detailed study of possible numerical algorithms suitable to solve the system in Eq.(6.8) with a significant saving of RAM is reported in [18]. Furthermore it is worth to note that this destriping technique is independent on a-priori assumptions of the actual value of f_k or the shape of the noise spectrum [*i.e.* the value of β in Eq.(6.4)]. It is also clear that the efficiency of the destriping depends upon these quantities: their expected values may help in optimizing the technique *e.g.* the choice of baseline levels per circle and pixel-crossing condition.

6.7 Simulations and main results

We started with a 30 GHz beam with location on the focal plane $(\theta_B, \phi_B) = (2.8°, 45°)$. As usual θ_B is the beam displacement angle from the optical axis of the telescope: this value is typical for LFI 100 GHz feeds (for a 1.55m effective aperture telescope) while in general the 30 GHz feeds are placed at larger θ_B values. We are conservative with our assumptions with respect to the destriping efficiency since in this case the intersections between different scan circles are closer to the Ecliptic poles hence yielding a less efficient destriping. The angle ϕ_B is the displacement of the beam center from the axis given by the intersection of two planes: the sky field of view plane and the plane containing the telescope and spin axes (see [19]). The choice of $\phi_B = 45°$ is intermediate between 0° (or 180°) and 90° which are equivalent to an on-axis beam and a beam which spreads scan circles crossings over the widest possible region. This is shown in Fig. 6-3. Beam location is then non-degenerate [*i.e.* it allows to solve system in Eq.(6.8)] but non optimal.

The adopted knee-frequency is $f_k = 0.05$ Hz. The angle between pointing and spin-axis is $\alpha = 90°$ and the scanning strategy has the spin-axis always on the Ecliptic plane. The effect of $1/f$ noise is evaluated in terms of noise angular power spectrum and of *rms* of additional noise with respect a pure white noise case. The white noise power spectrum

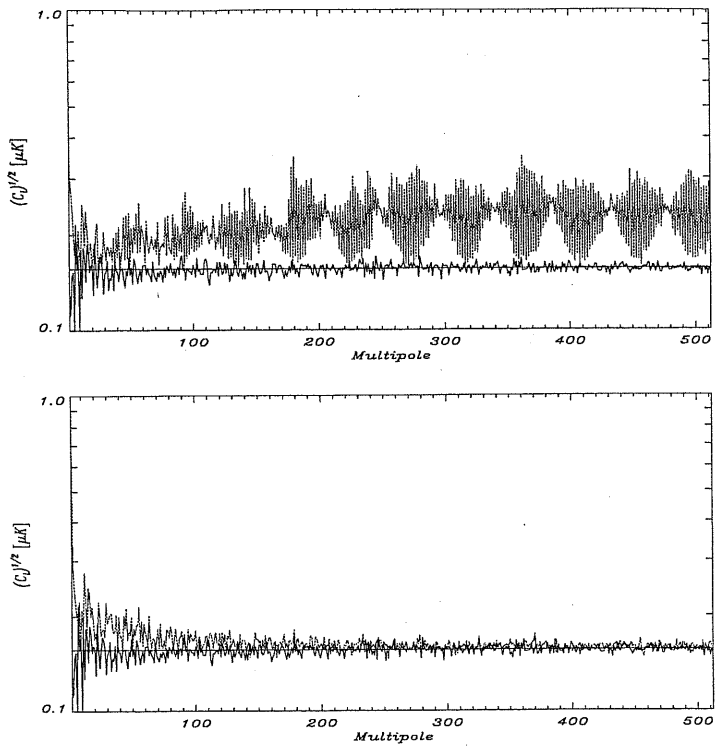

Figure 6-4: Noise power spectrum at 30 GHz before (top) and after (bottom) destriping. Simulation parameters are: $\alpha = 90°$, $(\theta_B, \phi_B) = (2.8°, 45°)$, $f_k = 0.05$ Hz and spin axis always on the Ecliptic plane. Theoretical white noise level is also reported for comparison. The overall excess of noise is about 40% over the white noise

can be derived analytically from the total number of pixels in the sky and pixel sensitivity:

$$C_{\ell,wn} = \frac{4\pi}{N_{\rm pix}^2} \sum_{i=1}^{N_{\rm pix}} \sigma_i^2 = \frac{4\pi}{N_{\rm pix}} \langle \sigma^2 \rangle \,, \tag{6.9}$$

where we have assumed an uniform sensitivity per pixel. In Fig. 6-4 (top panel) is reported the square root of power spectrum (which is roughly proportional to *rms* contribution per ℓ-bin) before applying destriping technique: the solid black line is the white noise level as derived from Eq.(6.9) and the superimposed spectrum is obtained from a simulation which considers only white noise. The agreement is very good and this probes the accuracy of FS code and map-making algorithm which do not insert any spurious artifacts. The gray line is the spectrum of white plus $1/f$ noise. The excess of noise in term of both *rms* and $\sqrt{C_\ell}$ is about 40% of the white noise level over the whole range of multipoles ℓ. The spectrum is clearly non-white: blobs are present with dimensions in ℓ space which depend on the geometrical properties of the simulation (beam position and the angle α).

We try to give an heuristic argument which explains the morphology of the blobs in the C_ℓ power spectrum. First of all there are two characteristic angular scales which determine the blobs shape:

1. the opening angle $\theta_1 \simeq [\alpha - \theta_B \sin\phi_B]$ for $\theta_B \ll \pi$ of the rings that the beam effectively traces in the sky;

2. the opening angle $\theta_2 = 90°$ of the ring which the spin-axis describes around the Sun in 1-year period.

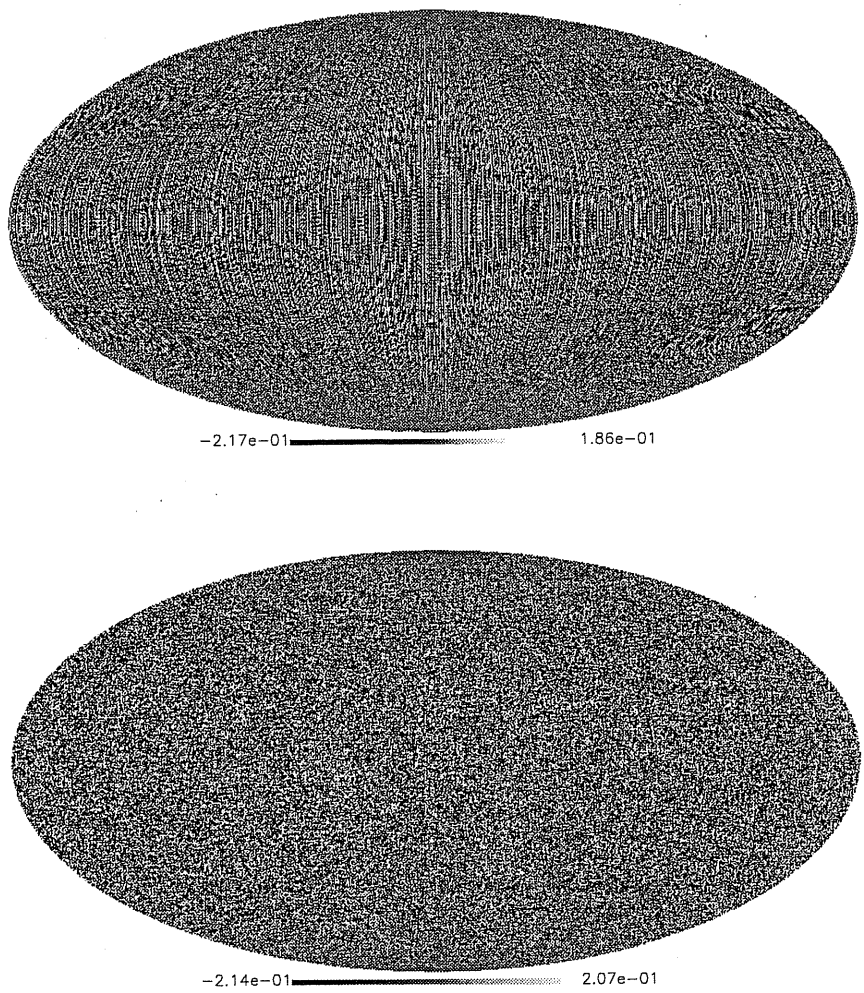

Figure 6-5: Baselines recovered from the destriping algorithm for the same case as in Fig. 6-2 (top panel) and pure noise (white plus $1/f$; bottom panel) map after subtraction of recovered baselines: stripes are no more visible. Units of mK.

The combination of these two scales produced the oscillations in the power spectrum: since these scales are really nearby, beats appears in the C_ℓ as in the top panel of Fig. 6-4. This is similar to a wave with θ_1 frequency and a sampling rate at frequency θ_2. The blob width in ℓ space is $\Delta\ell = 90/(\theta_2 - \theta_1)$. This simple argument agrees quite well with the observed blob dimension from power spectrum.

Fig. 6-5 shows the baselines, the constants A_i, as recovered from the destriping algorithm (top panel) and the noise map after subtraction of A_i from map in Fig. 6-2 (bottom panel): in comparison to Fig. 6-2 stripes are no more evident. The situation becomes more clear when we compute the noise power spectrum of the destripped map as in the bottom panel of Fig. 6-4. The spectrum is considerably flatter and no more blobs are present. The overall excess noise is now only 1-2% of the white noise level and the spectrum is noisier almost only at very low ℓ values while for $\ell \gtrsim 100$ the noise spectrum is almost indistinguishable from white. This is an interesting result: our technique removes very well the artifacts due to $1/f$ noise.

Possible periodic motion of the spin-axis away from the Ecliptic plane have the effect

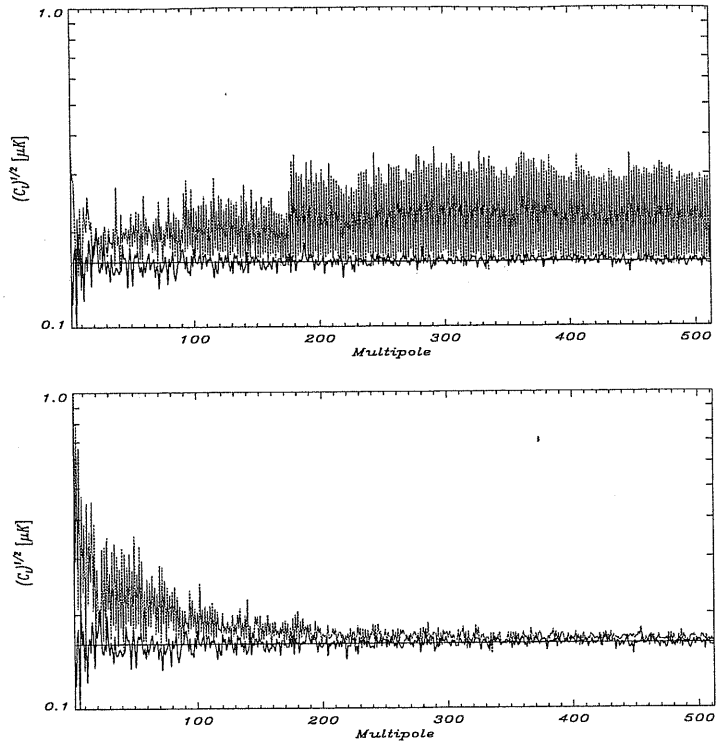

Figure 6-6: Noise power spectra at 30 GHz before (top) and after (bottom) destriping. Simulations parameters are the same of Fig. 6-4 but the beam location is now $(\theta_B, \phi_B) = (0°, 0°)$. The added noise is $\sim 45\%$ (before) and 5% (after) over the white noise level. White noise spectra are reported for comparison.

of broadening the region of crossing between different circles. This removes the degeneracy of the destriping system [Eq.(6.8)] when only two intersection points (namely the Ecliptic poles) are available. We implemented both sinusoidal oscillations and precession motions in the FS code: the first does not preserve the solar angle and this certaintely introduces thermal effects on the space-craft which are undesiderable. The second is preferable keeping the solar angle constant during the motion of the spin-axis. For both motions 10 complete oscillations per year of mission with 10° amplitude are considered. The results before and after destriping are nearly the same for the two cases and very similar to that for the simplest scanning strategy with no spin-axis motion: the overall noise level is always at $\sim 40\%$ and 1-2% over the white noise before and after destriping, respectively.

We consider also a case of an on-axis beam $(\theta_B, \phi_B) = (0°, 0°)$ with $\alpha = 90°$. This configuration represents the case for a couple of LFI feed-horns that, in the focal plane arrangement, are placed along the scanning direction: these horns are indeed equivalent to on-axis horns where intersections between different scan circles are very close to Ecliptic poles. A number of HFI feeds will also be in a similar situation. This represents a degenerate situation with respect destriping efficiency. Fig. 6-6 shows noise power spectra for this on-axis beam before (top) and after (bottom) destriping: the geometry of the simulation is changed and the same for blobs shape which our argument predicts to be $\Delta\ell \to \infty$ since $\theta_1 = \theta_2$. The level of the additional noise is $\sim 45\%$. After destriping we are left with an excess of noise of the order of 5% of the white noise at $\ell \lesssim 200$. This result is because of the nearly degeneracy of the destriping system which is no more efficient in recovering the A_i levels as before. A better configuration has to be found since the excess

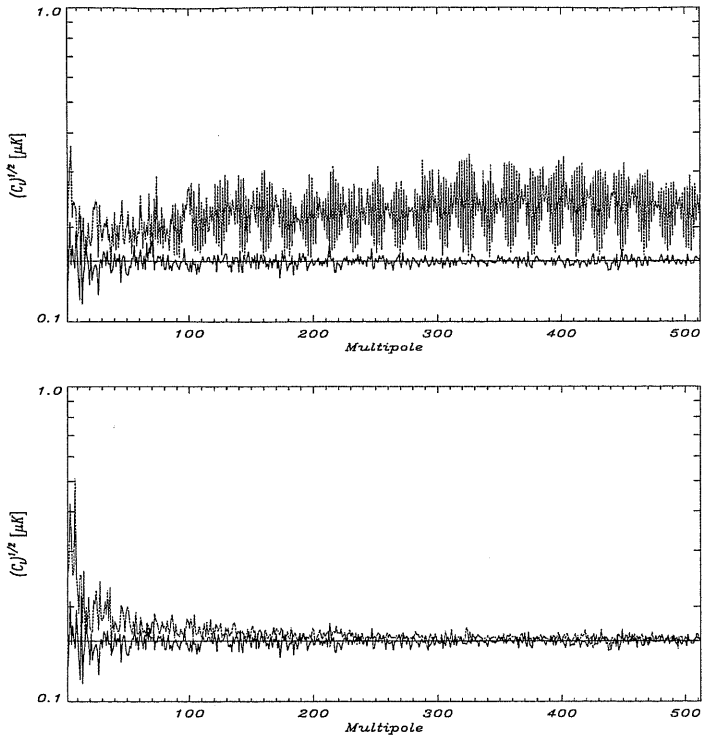

Figure 6-7: Noise power spectrum before (top) and after (bottom) destriping for the on-axis 85° case. The additional noise is $\sim$ 42% and 1-2% over the white noise level.

of noise *after* destriping is significant (from 30% at $\ell \sim 200$ to 60% for $\ell \simeq 50$). Keeping fixed the beam location on the focal plane, an angle $\alpha = 85°$ is considered: this of course leaves small regions around the Ecliptic poles which are not observed but has the benefit of enlarging the scan circles crossing region. Fig. 6-7 shows noise power spectra before and after destriping respectively for this on-axis and $\alpha = 85°$ case: now blobs are clearly visible with dimensions in ℓ-space different from Fig. 6-4 due to the different geometrical configuration and in agreement with our argument. Those blobs are completely removed after destriping leaving a level of additional noise of only $\sim$ 2% over the white noise. This is essentially what we obtain for the off-axis configuration.

All the simulations considered so far are with $f_k = 0.05$ Hz. The theoretical value for the knee-frequency with a reference load temperature of $T_y \simeq 4$ K is less than 1 mHz. Recent results however seem to show that, with the 4 K load, the knee-frequency would be probably larger than 0.01 Hz: this is mainly due to $1/f$ noise in the phase switches rather than in the amplifiers. Therefore the adopted value of 0.05 Hz is not far from reality. An interesting test with $f_k = 0.01$ Hz is performed to evaluate a possible better situation and which would be the benefits of a this low knee-frequency.

In this simulation the usual off-axis configuration $(2.8°, 45°)$ and $\alpha = 90°$ is restored. Results are reported in Fig. 6-8: it is interesting to note that now the level of additional noise is only 9% before destriping and reduces to only 0.5% after destriping.

6.8 Conclusions

This extensive work done on $1/f$ noise effect for PLANCK-LFI observations yields some final considerations. For most of the LFI feed-horns a choice of $\alpha = 90°$ is acceptable leaving only $\lesssim 2\%$ of extra-noise with respect white noise level and this is essentially at

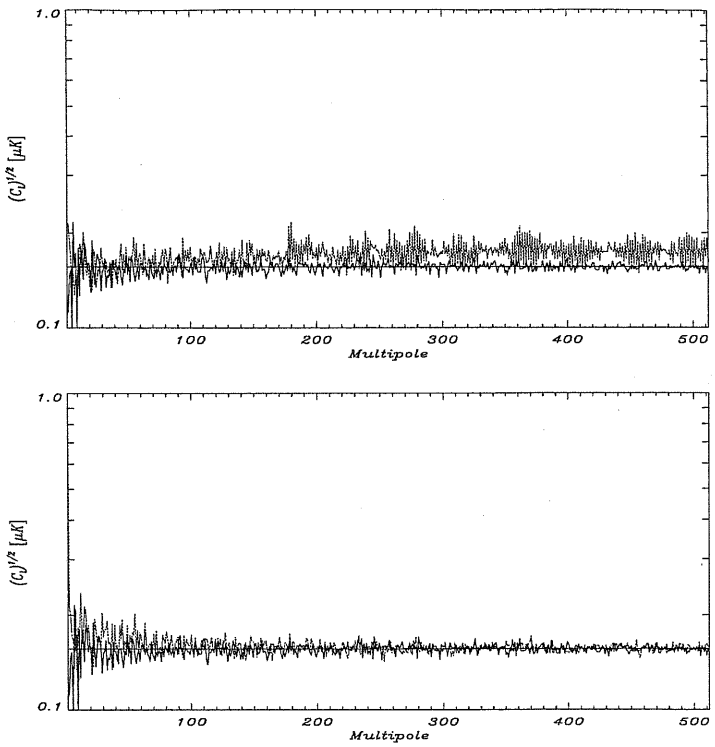

Figure 6-8: Noise power spectra before (top) and after (bottom) destriping for the 90°, off-axis $f_k = 0.01$ Hz case. Now the excess of noise is $\sim 9\%$ over the white noise level before destriping and less than 0.5% after destriping respectively. White noise spectra are reported for comparison.

small ℓ. Unfortunately some LFI feed-horns are equivalent to on-axis horns regarding destriping efficiency. An angle $\alpha \sim 85°$ (or at least $\alpha \sim 90° - \theta_{\rm FP}$ where $\theta_{\rm FP}$ is half of the PLANCK Focal Plane extension) breaks the observed degeneracy and restores the usual destriping efficiency. The full-sky coverage would be achieved with a small precession (only $\sim 5°$) which has the advantage of constant solar angle. This is indeed a critical point: no spin-axis motion means a more smoothed distribution of integration times, higher at the polar caps and degrading to the equator. Small precession of the spin-axis results in a very non uniform distribution of integration time which may be an issue in the data analysis processes. Furthermore the LFI capability in detecting CMB polarization signal (probably $\sim$ 5-10% of CMB temperature anisotropy) is possible with a very high sensitivity which is easily achieved at polar caps in the case of no spin-axis motion.

All the simulation are performed with $f_k = 0.05$ Hz which is larger than the theoretical value for the 4 K reference load. However several effects other than instabilities in the amplifiers may occur thus yielding a larger knee-frequency. In this much more realistic case it seems quite difficult to obtain $f_k = 0.01$ Hz with $T_y \simeq 4$ K (ten times larger than the theoretical value). Therefore simulations performed here are not far from "real" hardware performances and seem to indicate that with $f_k = 0.05$ Hz, the $1/f$ noise could be controlled in an efficient way.

In the ideality of these simulations, where the $1/f$ noise is the only effect considered as if all the other systematics were well under control, these results suggest that moving the spin-axis away from the Ecliptic plane does not help in a significant way to improve destriping efficiency. Therefore, in order to avoid possible thermal effects, which could generate other kind of systematics, is better for what concerns the $1/f$ noise alone to keep the spin-axis always on the Ecliptic plane.

There are of course many open issues both instrumental and astrophysical. Regarding the former a larger set of possible systematic effects has to be considered including thermal effects and stray-light contamination from our Galaxy [20]. These may degrade the destriping efficiency. On the astrophysical side, a more realistic model of microwave sky has to be computed including extra-galactic sources and in particular their time variability which may affect the destriping efficiency.

This is a strong requirement on the effective achievable knee-frequency and pushes the hardware efforts to obtain the lowest knee-frequency possible toward the theoretical value.

Chapter 7

Conclusions

The previous chapters have shown some accurate simulations that have been performed to address possible systematic effects in the observations of the LFI on board the PLANCK satellite. These results are extremely important in order to improve the design of the whole PLANCK mission. The main results can be summarized as follows:

- main beam distortions - the elliptical approximation of the main beam pattern yields useful order-of-magnitude estimation of the effect of main beam distortions and provide analytical relation with the most relevant beam parameters. "Real" beam shapes are far from gaussian and for the 100 GHz LFI feed-horns a large dispersion is found for the effective angular resolution values which depends on feed-horn position in the focal plane. The major effect of main beam distortions is a degradation in angular resolution which affects the LFI science in a considerable way: errors on cosmological parameters are $\sim 40\%$ larger for the Phase A 1.3m telescope than with a 1.75m telescope which provides the nominal $10'$ angular resolution at 100 GHz. These results have been the basis of design trade-off with ESA in the definition of the PLANCK telescope. Currently a new baseline telescope has been defined with a 1.55m aperture with possible improvements in Phase B.

- stray-light contamination - the analysis has shown the level as well as the spatial distribution of galactic stray-light due to intermediate and far side-lobes at 30 GHz. The far side-lobe contamination level is below the nominal sensitivity (peak at $\sim 6\mu$K, mean value $\simeq 2\mu$K), while the spatial distribution shows clearly features at high galactic latitudes where galactic emission is lower. A more precise evaluation should consider the 70 and 100 GHz channels since these are mostly CMB-dominated and therefore a direct stray-light impact on LFI science would be possible. Order-of-magnitude calculations yield a peak contamination of $\sim 2 \div 3\mu$K at 100 GHz for the far side-lobes with a mean value of $\simeq 1\mu$K, well below nominal sensitivity. However, Ecliptic polar caps have typical sensitivity ~ 5 times better than the average allowing possible measurements of CMB polarisation. In these regions stray-light contamination is comparable with nominal sensivitity. Furthermore these channels work well if lower frequency can monitor foreground emission in a good way. This asks for possible improvements of the telescope and baffle design to reduce side-lobes contribution.

- $1/f$ noise - the destriping code is extremely successful in removing from final maps artifacts due to amplifiers gain fluctuations: residual noise after destriping is usually $\lesssim 2\%$ of the white noise level for a knee frequency $f_k = 0.05$ Hz. However destriping efficiency is dependent on the scanning strategy, beam position in the focal plane, bore-sight angle and some degenerate positions have been found (on-axis, $\alpha = 90°$, mean residual noise $\simeq 5\%$ strongly affecting $\ell \lesssim 200$). Recent realistic simulations of hardware performances seem to indicate that even with a 4 K reference load, a knee frequency $f_k \simeq 0.01$ Hz (residual noise $\lesssim 0.5\%$ of the white noise) will be difficult to achieve because of $1/f$ noise due to sources other than the amplifiers. Simulations with higher values for f_k will be performed to assess the maximum acceptable f_k for a reasonable and removable level of contamination;

Of course this is a small set of all the possible relevant systematic effects, although possibly the most critical. Two are the most important sources of possible systematic effects which have not been considered so far and should be carefully addressd: internal stray-light and thermal effects.

By "internal stray-light" we mean the emission which originates within the PLANCK spacecraft, and therefore it is strictly related to the thermal effect issue. A model of the whole spacecraft thermal stability is needed as well as a full pay-load design to carefully evaluate the effect. When accurate simulations will be performed including internal stray-light, one should evaluate the additional noise and power spectrum of the effect and implement proper removal algorithms. Finally revised requirements on thermal stability are derived.

As for thermal effects one needs a thermal model and requirement for all the radiometric components (amplifiers, feed-horns, waveguide, front- and back-end units) of the LFI radiometers. This certainly includes: thermal stability and drift time-scales of the reference load (which has to be developed jointly with the HFI team), the telescope temperature, the thermal properties of a signle feed-horn and of the whole ensemble of LFI radiometers, environment temperature and soprtion cooler. Accurate simulations should provide the output of the instrument itself, *i.e.* , the output signal when looking a zero temperature load. This has to be re-projected into the sky according to the scanning strategy and its effects on observations have to be derived.

In general for a complete analysis of a single systematic effect one has to identify which are the inputs required, which are the expected outcomes of the analysis and to which other effects there is a link. Here is an example of this list:

- the inputs: simulated sky, model of the systematic effect, main parameters required;
- the outputs: degradation of nominal LFI characteristics because of the systematic effect (extra-noise, angular power spectrum of the effect) and impact on LFI science (multi-parameter fit of recovered CMB power spectrum, Fisher Matrix for errors estimation);
- related issues: those systematic effects which are obviously related to the effect under study (*e.g.* main beam distortions may affect the efficiency of the destriping code).

In this way it is possible to estimate the impact of a single systematic effects on LFI observation. In fact all the simulations considered so far are performed in an ideal condition: the only systematic effect present is the one under study (main beam distortion, $1/f$

noise and stray-light) as if all the others were exactly known and properly controlled. Of course a more realistic and accurate simulation should include several systematic effects at the same time. Therefore it is possible to verify the efficiency of removal techniques in a more complicated, by closer to reality, situation. In fact some level of degradation of the efficiency of, *e.g.* the destriping algorithm, is expected when including main beam distortions or stray-light contamination. This is an important point since all the results of those simulations considered here have to be regarded as lower limits for the impact of systematic effects. This will be the next step.

It is important to mention, for a clear view of the work presented in this thesis, that previous simulations are performed as a part of the activity of the LFI Modeling & Simulations Team as reported in the "Science Operation Implementation Plan". The aim of this Team is to produce PLANCK Time-Ordered-Data (TOD) exploiting realistic simulated input sky and simulated instrumental properties and performances. Within the Modeling & Simulations Team, data analysis software propotypes are, and will be, produced to "clean" data from systematic effects and to build sky maps at various observing frequencies. The software implemented for this thesis is the first step towards the PLANCK data analysis pipeline.

Bibliography

[1] C. Baccigalupi *et al.*, *private communication* (1998)

[2] A.J. Banday *et al.*, *ApJ*, **468**, L85 (1996)

[3] A.J. Banday & A.W. Wolfendale, *MNRAS*, **245**, 182 (1990)

[4] A.J. Banday & A.W. Wolfendale, *MNRAS*, **248**, 705 (1991)

[5] C.L. Bennet *et al.*, *ApJ*, **396**, L7 (1992)

[6] C. Bennet *et al.*, *Amer. Astro. Soc. Meet.*, **88.05** (1996)

[7] E.M. Berkhuijsen, *A&A*, **24**, 143 (1972)

[8] M. Bersanelli *et al.*, *A&ASS*, **121**, 393 (1997)

[9] M. Bersanelli *et al.*, *COBRAS/SAMBA - Report on the Phase A Study*, ESA Report D/SCI(96)3 (1996)

[10] M. Bersanelli *et al.*, *Experimental Astronomy*, in press (1998)

[11] E.J. Blum, *Annales d'Astrophysique*, **22-2**, 140 (1959)

[12] J.R. Bond, *Theory and Observations of the Cosmic Background Radiation*, in " Cosmology and Large-Scale Structure", proceedings of the Les Houches Summer School, Session LX, R. Schaeffer, ed. (elsevier Science Publishers, Netherlands) (1995)

[13] J.R. Bond & G. Efstathiou, *ApJ*, **285**, L5 (1984)

[14] J.R. Bond & G. Efstathiou, *MNRAS*, **226**, 655 (1987)

[15] J.R. Bond, G. Efstathiou & M. Tegmark, *MNRAS*, **291**, L33 (1997)

[16] F. Bouchet & R. Gispert, Elsevies preprint (1999)

[17] E.F. Bunn & M.White, *ApJ*, **480**, 6 (1997)

[18] C. Burigana *et al.*, *Int. Rep. TeSRE/CNR*, **198** (1997)

[19] C. Burigana *et al.*. *A&ASS*, **130**, 551 (1998)

[20] C. Burigana *et al.*, A&ASS, submitted (1999)

[21] B. Cappellini, *Degree Thesis*, Milano University (1999)

[22] R.S. Colvin, *Ph.D. Thesis - Standford University*, (1961)

[23] B.E. Corey & D.T. Wilkinson, *Bull. Am. Astron. Soc.*, **8**, 351 (1976)

[24] R.A. Daly, *ApJ*, **371**, 14 (1991)

[25] L. Danese, G. De Zotti, A. Franceschini & L. Toffolatti, *ApJ*, **318**, L15 (1987)

[26] L. Danese, L. Toffolatti, A. Franceschini, M. Bersanelli, N, Mandolesi, *AL&C*, **35**, 257, (1996)

[27] R.D. Davies, R.A. Watson & C.M. Gutierrez, *MNRAS*, **278**, 925 (1996)

[28] P. De Bernardis & S. Masi, *Proceedings of the XXXIIIrd Moriond Astrophysics Meeting*, p.209 (1998)

[29] J. Delabrouille, *A&ASS*, **127**, 555 (1998)

[30] P. De Maagt, A.M. Polegre & G. Crone, PLANCK-*Stray-light evaluation of the Carrier Configuration*, Technical report ESA, PT-TN-05697, 1/0

[31] A. De Oliveira-Costa *et al.ApJ*, **482**, L17 (1997)

[32] A. De Oliveira-Costa *et al.*, *ApJ in press*, astro-ph/9904296 (1999)

[33] A. De Oliveira-Costa *et al.*, *ApJ*, submitted (1998)

[34] R.H. Dicke, P.J.E. Peebles, P.G. Roll & D.T. Wilkinson, *ApJ*, **142**, 414 (1965)

[35] B.T. Draine & A. Lazarian, *ApJ*, **494**, L19 (1998)

[36] E. Dwek *et al.*, *ApJ*, **475**, 565 (1997)

[37] A.R. Duncan *et al.*, *MNRAS*, **291**, 279 (1997)

[38] D.J. Eisenstein, W. Hu & M. Tegmark, em ApJ submitted, astro-ph/9807130 (1998)

[39] A. Ferrara & R.J. Dettmar, *ApJ*, **427**, 155 (1994)

[40] D.P. Finkbeiner, M. Davis & D.J. Schlegel, *ApJ submitted*, astro-ph/9905128 (1999)

[41] D.J. Fixsen *et al.*, *ApJ*, **473**, 576 (1996)

[42] A. Franceschini, L. Toffolatti, L. Danese & G. De Zotti, *ApJ*, **344**, 35 (1989)

[43] A. Franceschini & P. Andreani, *ApJ*, **440**, L5 (1995)

[44] A. Franceschini *et al.*. *Proceedings of the ESA Symposium 'The Far Infrared and Submillimitre Universe'*, **ESA SP-401**, 159 (1997)

[45] T. Gaier, *private communication* (1997)

[46] G. Gamow, *Phys. Rev.*, **74**, 506 (1948)

[47] K. Ganga *et al.*, *ApJ*, **432**, L15 (1994).

[48] T.N. Gautier III, F. Boulanger, M. Perault & J.L. Puget, *AJ*, **103** 1313 (1992)

[49] K.M. Górski *et al.ApJ*, **464**, 11 (1996)

[50] K. M. Gorski, E. Hivon & B. D. Wandelt, *Proceedings of the MPA/ESO Conference on the Evolution of Large-Scal Structures: from Recombination to Garching*, Banday *et al.*(Eds.), astro-ph/9812350 (1998)

[51] C. Gruppioni, M. Mignoli & G. Zamorani, astro-ph/9811309

[52] Hancock *et al.*, *MNRAS*, **289**, 505 (1997).

[53] C.G.T. Haslam, C.J. Salter, H. Stoffel & W.E. Wilson, *A&ASS*, **47**, 1 (1982)

[54] M.P. Hobson, A.W. Jones, A.N. Lasenby & F.R. Bouchet, *MNRAS submitted*, astro-ph/9806387 (1998)

[55] W. Hu & M. White, *ApJ*, **479**, 568 (1997)

[56] E.P. Hubble, *Proc. Natl. Acad. Sci. U.S.*, **15**, 169 (1929)

[57] M. Janssen *et al.*, astro-ph/9602009

[58] J. Jonas, E.E. Baart & G.D. Nicolson, *MNRAS*, bf 297, 997 (1998)

[59] M. Kamionkowski, A. Kosowski, A. Stebbins, *Phys. Rev. D*, **55**, 7368 (1997)

[60] A. Kogut *et al.*, *ApJ*, **419**, 1 (1993)

[61] A. Kogut *et al.*, *ApJ*, **433**, 435 (1994)

[62] A. Kogut *et al.*, *ApJ*, **460**, 1 (1996)

[63] A. Kogut *et al.*, *ApJ*, **464**, L5 (1996)

[64] R.J. Kron *et al.*, *A&A*, **146**, 38 (1985)

[65] K.D. Lawson *et al.*, *MNRAS*, **225**, 307 (1987)

[66] A.N. Lasenby, *Proceedings of the XVI Moriond Astrophysics Meeting*, eds. F.R. Bouchet, R. Gispert, B. Guiderdoni, J. Tran Thanh Van, p. 445 (1996)

[67] A.N. Lasenby, A.W. Jones & Y. Dabrowski, *Proceedings of the XXXIII^d Moriond Astrophysics Meeting*, p. 221 (1998)

[68] E.M. Leitch *et al.*, *ApJ*, **486**, L23 (1997)

[69] A.D. Linde, *Particle Physics and Cosmology*, Harwood Academic, Chur, Switzerland (1990)

[70] M. Longain, *High Energy Astrophysics*, Cambridge (1994)

[71] D. Maino *et al.*, *ISAS Internal report*, in preparation (1999)

[72] D. Maino *et al.*, *Contribution to Stray-light Analysis*, ITeSRE (1999)

[73] N. Mandolesi *et al.*, *COBRAS, proposal submitted to ESA M3* (1993)

[74] N. Mandolesi *et al.*, Planck-LFI, A Proposal Submitted to the ESA (1998)

[75] N. Mandolesi *et al.*, A&ASS, in preparation (1999)

[76] N. Mandolesi *et al.*, astro-ph/9904135 (1999)

[77] S. Masi *et al.*, *ApJ*, **463**, L47 (1996).

[78] P.R. McCullough *et al.*, *ASPCS*, **181**, 253 (1999)

[79] J. Milogradov-Turin, *MNRAS*, **161**, 269 (1984)

[80] P.F. Muciaccia, P. Natoli & N. Vittorio, astro-ph/9703084 (1997)

[81] P.H. Nielsen & K. Pontoppidan, DESIGN & ANALYSIS OF THE COBRAS/SAMBA TELESCOPE - TICRA REP., **S-699-02** (1996)

[82] J. Nishimura *et al.*, *Proceedings 21st ICRC*, **Vol. 3**, 213 (1991)

[83] C. B. Netterfield *et al.*, *ApJ*, **474**, 47 (1997).

[84] R. Paladini, Degree Thesis, Milano University (1999)

[85] R.B. Partridge, *3K: The Cosmic Microwave Background Radiation*, Cambridge Univ. Press, (1995)

[86] I.I.K. Pauliny-Toth & J.R. Shakeshaft, *MNRAS*, **124**, 61 (1962)

[87] P.J.E. Peebles & J.T. Yu, *ApJ*, **162**, 815 (1970)

[88] A.A. Penzias & R.W. Wilson, *ApJ*, **142**, 419 (1965)

[89] P. Platania *et al.*, *ApJ*, **505**, 473 (1998)

[90] Pospieszalsky, *MTT*, Sep., 1340 (1989)

[91] W.H. Press, *Comments Astrophys*, **7**, 103 (1978)

[92] W.H. Press *et al.*, *Numerical Recipes in Fortran*, Cambridge University Press (1992)

[93] J.L. Puget *et al.*, *SAMBA, proposal submitted to ESA M3* (1993)

[94] J.L. Puget *et al.*, HFI for the Planck mission, A proposal Submitted to the ESA (1998)

[95] J.L. Puget & J. Delabrouille, *private communication* (1999)

[96] R.J. Reynholds, S.L. Tufte, L.M. Haffner, K. Jaehnig & J.W. Percival, *Publ. Astron. Soc. Ausr.*, **15**, 14 (1998)

[97] M.J. Rees & D.W. Sciama, *Nature*, **310**, 391 (1968)

[98] P. Reich & W. Reich, *A&ASS*, **63**, 106 (1986)

[99] P. Reich & W. Reich, *A&ASS*, **74**, 7 (1988)

[100] G.B. Rybicki & A.P Lightman, *Radiative Processes in Astrophysics*, Wiley (1979)

[101] R.K. Sachs & A.M. Wolfe, *ApJ*, **147**, 73 (1967)

[102] D.J. Schlegen *et al.*, *ApJ*, **500**, 525 (1998)

[103] M. Seiffert *et al.*, *Rev. Sci. Instrum.*, submitted (1997)

[104] U. Seljak, *ApJ*, **482**, 6 (1996)

[105] U. Seljak & M. Zaldarriaga, *Phys. Rev. Lett.*, **78**, 2054 (1997)

[106] J. Silk, *Nature*, **215**, 1155 (1967)

[107] J. Silk, *ApJ*, **151**, 459 (1968)

[108] J.H. Simonetti, B. Dennison & G.A. Topsana, *ApJ*, **458**, L1 (1996)

[109] C.J. Sletten, REFLECTOR AND LENS ANTENNAS, Artech House (1998)

[110] M.S. Smith, L.H. Kawano & R.A. Malaney, *ApJ Supp.*, **85**, 219 (1993)

[111] G.F. Smoot, M.V. Gorestein & R.A. Muller, *Phys. Rev. Lett.*, **39**, 898 (1977)

[112] G.F. Smoot *et al.*, *ApJ*, **396**, L1 (1992)

[113] G.F. Smoot, astro-ph/9801121 (1998)

[114] G. Strang, *Linear Algebra and Its Applications*, Academic Press Inc. (1976)

[115] M. Tegmark & G. Efstathiou, *MNRAS*, **281**, 1297 (1996)

[116] M. Tegmark, A. Taylor, A.F. Heavens, *ApJ*, **480**, 22 (1997)

[117] L. Toffolatti *et al.*, *MNRAS in press*, astro-ph/9711085

[118] G. S. Tucker *et al.*,*ApJ*, **475**, 73 (1997).

[119] A.J. Turtle & J.E. Baldwin, *MNRAS*, **240**, 225 (1962)

[120] F. Villa, M. Bersanelli & N. Mandolesi, *Int. Rep. TeSRE/CNR*, **188** (1997)

[121] F. Villa *et al.*, PROCEEDINGS OF THE XVIIIth MORIOND ASTROPHYSICS MEETING, LES ARC, SAVOIE, FRENCH, 17-24 JANUARY 1998, (1998)

[122] L.A. Wade & A.R. Levy, *Cryocoolers*, **9**, 587 (1997)

[123] P.N. Walker *et al.*, *ApJ*, **376**, 51 (1991)

[124] B.D. Wandelt & K.M. Górski, *in preparation* (1999)

[125] Y. Wang, D.N. Spergel & M.A. Strauss, *ApJ accepted*, astro-ph/9802231 (1998)

[126] W. Webber, *Composition and origin of cosmis rays*, Shapiro Eds. (1983)

[127] S. Weinreb, *private communication* (1997)

[128] M. White, *A&A*, **290**, L1 (1994)

[129] E. Wollack, *Rev. of Sci. Instruments*, **66**, 8, 4305 (1995)

[130] E.L. Wright, *IAS CMB Data Analysis Workshop*, Princeton 22 Nov. 1996, astro-ph/9612006

[131] E.L. Wright, *ApJ in press*, astro-ph/9711261 (1997)

[132] M. Zaldarriaga & U. Seljak, *Phys. Rev. D.*, **55**, 7368 (1997)

[133] M. Zaldarriaga, D. Spergel & U. Seljak, astro-ph/9702157 (1997)

Appendix A

The Fisher Information Matrix and cosmological parameters[1]

In this appendix we describe the formalism of the Fisher Information Matrix applied for estimating the errors on cosmological parameters for the PLANCK-LFI instrument for different telescope designs (see Chapter 4).

The usual way to infer errors on cosmological parameters from CMB data from a given experiment is via the Fisher Information Matrix (*e.g.* [15, 116, 38]). Suppose that after data reduction and analysis we found the underlying cosmological model to our data in terms of a set of C_ℓ coefficients and suppose we have a consistent model containing cosmological parameters to fit these coefficients. Then the Fisher Matrix simply tells us how the data depend upon the set of cosmological parameters we want to measure. Given this set the Fisher Matrix yields a lower limit to the error bars on such parameters. Under the hypothesis that the signal and noise are Gaussian distributed (which may not be true either due to the signal itself, either due to the adopted scanning strategy and to the $1/f$ noise) it is possible to build the Fisher matrix for the selected cosmological model with the specifications of a generic CMB experiment.

Let $\mathbf{x}$ be the vector of the observed data, $\mathbf{p}$ the model parameters vector and $L(\mathbf{x};\mathbf{p})$ the probability of observing the $\mathbf{x}$ data set from the model parameters set $\mathbf{p}$. The vector $\mathbf{x}$ has components given by the C_ℓ coefficients while the vector $\mathbf{p}$ has components equal to the number of cosmological parameters under consideration. The Fisher matrix is defined as:

$$(\mathbf{F})_{ij} = -\left\langle \frac{\partial^2 \ln L}{\partial p_i \partial p_j} \right\rangle_{\mathbf{x}} . \tag{A.1}$$

If we want to estimate the error on a single parameter when the others are already determined, the 1-sigma error is simply $1/\sqrt{F_{ij}}$. If instead we want to constrain the whole set of model parameters at the same time, the resulting error on the i^{th} parameter is the square root of $(\mathbf{F^{-1}})_{ii}$.

It is important to point out that these errors may not be comparable with those derived from a χ^2 fit or likelihood analysis of the data. In fact only if the likelihood function is nearly gaussian around its maximum, those errors would be comparable. This is the case when the estimated errors are small compared with the range over which a

[1] Based on D. Maino *et al.*, ISAS Internal Report, in preparation

cosmological parameter alters model prediction [133]. Furthermore in order to obtain meaningful results it is important to use high accuracy calculation in computing the CMB angular power spectra instead of approximated methods. These approximations will lead to an artificial breaking of the degeneracy between parameters yielding to un-real small errors.

Following Seljak [104] (see also [132, 59]) the Fisher matrix for the CMB anisotropies with the assumption of gaussian distributed noise can be written:

$$\mathbf{F}_{ij} = \sum_{\ell} \sum_{X,Y} \frac{\partial C_{X\ell}}{\partial p_i} (\mathrm{Cov}_\ell)^{-1}_{XY} \frac{\partial C_{Y\ell}}{\partial p_j}, \tag{A.2}$$

where $C_{X\ell}$ is the angular power spectrum for $X = T, E, B$ and C (T is temperature, E and B are the two polarization channels and C is the temperature-polarization correlation) in the multipole ℓ. In computing the Fisher matrix we evaluate the derivative with respect to one independent parameter, holding all the others fixed: note that in the Fisher matrix we are varying all the parameters simultaneously because each parameter is varied and correlations between them are in the matrix thought their derivatives products. The derivatives are computed, when possible, using two-sided finite differences:

$$\frac{\partial C_\ell}{\partial p_i} = \frac{C_\ell(p_i + \Delta p_i) - C_\ell(p_i - \Delta p_i)}{2\Delta p_i}, \tag{A.3}$$

where the step amplitude Δp_i is usually 5% of the model value of the parameter p_i.

The Cov_ℓ is the covariance matrix between various power spectra. Its non zero components are listed below:

$$(\mathrm{Cov}_\ell)_{TT} = \frac{2}{(2\ell+1) f_{sky}} (C_{T\ell} + w_T^{-1} B_\ell^{-2})^2, \tag{A.4}$$

$$(\mathrm{Cov}_\ell)_{EE} = \frac{2}{(2\ell+1) f_{sky}} (C_{E\ell} + w_P^{-1} B_\ell^{-2})^2, \tag{A.5}$$

$$(\mathrm{Cov}_\ell)_{BB} = \frac{2}{(2\ell+1) f_{sky}} (C_{B\ell} + w_P^{-1} B_\ell^{-2})^2, \tag{A.6}$$

$$(\mathrm{Cov}_\ell)_{CC} = \frac{2}{(2\ell+1) f_{sky}} \left[C_{C\ell}^2 + (C_{T\ell} + w_T^{-1} B_\ell^{-2}) \times (C_{E\ell} + w_P^{-1} B_\ell^{-2}) \right], \tag{A.7}$$

$$(\mathrm{Cov}_\ell)_{TE} = \frac{2}{(2\ell+1) f_{sky}} C_{C\ell}^2, \tag{A.8}$$

$$(\mathrm{Cov}_\ell)_{TC} = \frac{2}{(2\ell+1) f_{sky}} C_{C\ell} (C_{T\ell} + w_T^{-1} B_\ell^{-2}), \tag{A.9}$$

$$(\mathrm{Cov}_\ell)_{EC} = \frac{2}{(2\ell+1) f_{sky}} C_{C\ell} (C_{E\ell} + w_P^{-1} B_\ell^{-2}), \tag{A.10}$$

where B_ℓ^2 is the beam window function (denoted with W_ℓ in Chapter 4), that for a gaussian beam is given by $B_\ell^2 = \exp[-\ell(\ell+1)\,\theta^2/8\ln 2]$ with θ the FWHM (Full Width Half Maximum) of the beam in radians, and $w_{T,P}^{-1} = \sigma_{T,P}^2 \theta^2$ where $\sigma_{T,P}$ is the noise level per pixel for temperature and polarization respectively. For PLANCK-LFI detectors, which are

Experiment	Frequency [GHz]	θ [']	σ_T [μK]	σ_P [μK]
MAP:	40	28.2	27.	38.2
	60	21.0	35.	49.5
	90	12.6	35.	49.5
PLANCK-LFI:	70	14	10	20
	100	10	12	24

Table A.1: PLANCK-LFI and MAP specifications: for MAP $w_T = w_P/2$ is assumed [125]

naturally sensitive to polarization, we assumed $\sigma_P = 2\sigma_T$. This in general depends upon the chosen assembly of the different feed horns in the focal-plane.

For PLANCK-LFI we consider only the two cosmological channels at 70 and 100 GHz with their nominal specifications [74]. We suppose that the 30 and 44 GHz are used to control foreground contamination (mainly galactic free-free) while the HFI channels provide the useful informations for cleaning dust contamination. The main properties of the two considered channels are reported in Table A.1 together with MAP specification as in Wang *et al.*[125]. We compared our results with this work to establish the accuracy and validate our machinery. Since we use multiple channel experiments, we perform a weighted average over the number of channels. We obtain:

$$w_T = \sum_c w_T^c, \tag{A.11}$$

$$B_\ell^2 = \frac{\sum_c w_T^c B_{\ell,c}^2}{\sum_c w_T^2}, \tag{A.12}$$

plus the usual relation between w_T and w_P.

Our cosmological models are determined by the matter density Ω_m, the cosmological constant Ω_Λ, the baryons content Ω_b, the Hubble constant h, the re-ionization optical depth τ_{ri}, the primordial spectral index n_S and the CMB power spectrum normalization C_2, where the Hubble constant is written in units of 100 Km/s/Mpc. We express the densities in units of the critical density and we have $\Omega_m = 1 - \Omega_\Lambda - \Omega_K$ where Ω_K is the curvature contribution. Once we have the Fisher matrix for the chosen sets of cosmological parameters, we are free to derive marginalized errors for any kind of cosmological variable $g(\mathbf{p})$ using:

$$\sigma_g^2 = \sum_{i,j} \left(\frac{\partial g}{\partial p_i}\right) (\mathbf{F}^{-1})_{ij} \left(\frac{\partial g}{\partial p_j}\right). \tag{A.13}$$

We consider two models: a standard CDM (SCDM) and a CDM model with a cosmological constant (ΛCDM). We normalize power spectra to *COBE* four-year data as in Bunn & White [17]. The model considered are flat by definition and we require that $\Omega_m + \Omega_\Lambda = 1$. Table A.2 lists model values for cosmological parameters. Some models for inflation predict a contribution to CMB fluctuations by gravitational waves at small ℓ. But even in these models, gravity waves do not contribute in a significant way to anisotropy

	h	Ω_B	Ω_Λ	Ω_m	τ_{ri}	n_S	C_2
SCDM	0.50	0.05	0	1	0.05	1	$113.9\mu\mathrm{K}^2$
ΛCDM	0.65	0.06	0.7	0.3	0.1	1	$145.5\mu\mathrm{K}^2$

Table A.2: Cosmological parameters in our models

	Wang *et al.*[125]		this work	
1-σ error	MAP^T	MAP$^{(T+P)}$	MAP^T	MAP$^{(T+P)}$
$\Delta\ln C_2$	0.17	0.065	0.16	0.063
$\Delta\ln h$	0.052	0.033	0.051	0.032
$\Delta\Omega_\Lambda$	0.15	0.091	0.15	0.093
$\Delta\ln(\Omega_b h^2)$	0.028	0.020	0.028	0.020
$\Delta\ln\tau_{ri}$	2.4	0.39	2.5	0.39
$\Delta\ln n_S$	0.017	0.0085	0.017	0.0081

Table A.3: Fisher Matrix 1-σ errors for SCDM model for MAP experiment as in Wang *et al.*[125]

for $\ell \gtrsim 100$. We therefore do not consider tensor perturbations and hence the B mode of CMB polarization.

We consider the MAP case with the same specification as in Wang *et al.*[125]. Results are reported in Table A.3 and Table A.4 for both the considered models and for temperature and temperature plus polarization measurements. The agreement is quite good being less than 6% on C_2 (SCDM) and $\lesssim 4\%$ for all the other parameters for both SCDM and ΛCDM models. This is quite good and validate our machinery. Results for LFI are reported in Table 3.3 and Table 3.4: errors are typically $2\div3$ times smaller than for MAP.

	Wang *et al.*[125]		this work	
1-σ error	MAP^T	MAP$^{(T+P)}$	MAP^T	MAP$^{(T+P)}$
$\Delta\ln C_2$	0.21	0.043	0.22	0.043
$\Delta\ln h$	0.066	0.032	0.066	0.032
$\Delta\ln\Omega_\Lambda$	0.076	0.037	0.076	0.037
$\Delta\ln(\Omega_b h^2)$	0.044	0.021	0.044	0.021
$\Delta\ln\tau_{ri}$	1.33	0.18	1.32	0.18
$\Delta\ln n_S$	0.034	0.014	0.034	0.013

Table A.4: Fisher Matrix 1-σ errors for ΛCDM model for MAP experiment as in Wang *et al.*[125]